Order Number: 42482

Université de Lille

Doctoral School **SMRE**

University Department **Laboratoire de Physique de Lasers, Atomes et Molécules**

Habilitation to conduct research defended by **Matteo Conforti**

Defended on **18th December, 2017**

Academic Field **Physics**

Instabilities, shock waves and solitons in optical fiber systems

Guarantor Alexandre Kudlinski

Committee members

Referees	Alain Barthélémy	Institut XLIM, Limoges
	Antonio Picozzi	Laboratoire ICB, Dijon
	Thibaut Sylvestre	Institut FEMTO ST, Besançon
Examiners	Stephan De Bièvre	Université de Lille
	Arnaud Mussot	Université de Lille
	Giovanna Tissoni	Institut InPhyNi, Nice
	Stefano Trillo	Università di Ferrara
Guarantor	Alexandre Kudlinski	Université de Lille

Université de Lille

École doctorale **SMRE**

Unité de recherche **Laboratoire de Physique de Lasers, Atomes et Molécules**

Habilitation à diriger les recherches présentée par **Matteo Conforti**

Soutenue le **18 décembre 2017**

Discipline **Physique**

Instabilités, ondes de choc et solitons dans les systèmes à fibre optique

Garant Alexandre Kudlinski

Composition du jury

Rapporteurs	Alain Barthélémy	Institut XLIM, Limoges
	Antonio Picozzi	Laboratoire ICB, Dijon
	Thibaut Sylvestre	Institut FEMTO ST, Besançon
Examinateurs	Stephan De Bièvre	Université de Lille
	Arnaud Mussot	Université de Lille
	Giovanna Tissoni	Institut InPhyNi, Nice
	Stefano Trillo	Università di Ferrara
Garant	Alexandre Kudlinski	Université de Lille

This habilitation to conduct research has been prepared at the following research units.

Laboratoire de Physique de Lasers, Atomes et Molécules
Bât. P5 - USTL
F-59655 Villeneuve d'ascq cedex

IRCICA
CAMPUS Haute-Borne CNRS IRCICA-IRI-RMN
Parc Scientifique de la Haute Borne
50 Avenue Halley
BP 70478
59658 Villeneuve d'Ascq Cédex

Instabilities, shock waves and solitons in optical fiber systems

Abstract

This Manuscript resumes the principal research activities that I have conducted since my arrival at the *Laboratoire de Physique des Lasers, Atomes et Molécules* (PhLAM). The first Chapter describes the development of modulation and parametric instabilities in passive ring cavities with inhomogeneous dispersion. The second Chapter is devoted to the analysis of the nonlinear stage of modulation instability in optical fibers with periodic dispersion. The third Chapter deals with dispersive shock waves in fibers and resonators. The fourth Chapter reports on the interactions between solitons and linear waves in optical fibers with varying dispersion. The last part of the Thesis, composed of four Appendices, reports a complete list of my publications, my Curriculum Vitae, a summary of teaching and supervision activities, of responsibilities and of scientific collaborations.

Keywords: shock waves, instabilities, solitons, nonlinear optics, fibers

Instabilités, ondes de choc et solitons dans les systèmes à fibre optique

Résumé

Ce Manuscrit résume les principales activités des recherche que j'ai menées depuis mon arrivée au *Laboratoire de Physique des Lasers, Atomes et Molécules* (PhLAM). Le premier Chapitre décrit les études de l'instabilité de modulation et paramétrique dans les cavités fibrées avec une modulation longitudinale de la dispersion. Le deuxième Chapitre est dédié à l'analyse du régime non-linéaire de l'instabilité de modulation dans des fibres optiques avec dispersion périodique. Le troisième Chapitre traite des ondes de choc dispersives dans les fibres optiques et les résonateurs. Le quatrième Chapitre porte sur les interactions entre solitons et ondes linéaires dans les fibres optiques avec dispersion variable. La dernière partie de la Thèse, composée de quatre Appendices, contient une liste complète de mes publications, mon Curriculum Vitæ, un résumé de mes activités d'enseignement et encadrement, de mes responsabilités scientifiques et de mes collaborations.

Mots clés : ondes de choc, instabilités, solitons, optique non-linéaire , fibres

Laboratoire de Physique de Lasers, Atomes et Molécules
Bât. P5 - USTL – F-59655 Villeneuve d'ascq cedex

Remerciements

Je remercie toutes les personnes qui ont contribué de près ou de loin à ce travail.

Contents

Introduction

This Thesis reports an overview of the principal research activities which I developed throughout my career. I will focus on the research that I conduct at the Laboratoire de Physique de Laser, Atomes et Molécules since 2014. Nonetheless, in this Introduction I will describe very briefly my early scientific path in Brescia during my PhD and post-docs from 2003 to 2013.
My involvement in research started in 2003 with my Master's degree Thesis (called *Laurea* in Italy) on the development of finite-element codes for the numerical solution of Maxwell equations, with application to Photonic Crystals. The Thesis was developed as a joint collaboration between the Department of Mathematics and the Department of Electronics for Automation of the University of Brescia. From then on, the interdisciplinarity, at the borderline between Physics, Mathematics and Engineering, has been a signature of my research activity. This experience has been developed during my PhD (2004-2007) on *Theoretical and Numerical Modelling of Nanostructred Photonic Devices*, and during my post-docs in Brescia, at Department of Electronics for Automation (2007-2009) and at Department of Information Engineering (2009-2013). I studied such diverse fields as computational electromagnetics, nonlinear dynamical systems, solitons, frequency conversion, quadratic crystals, and plasmonics. Below I report a brief description of my principal research achievements during the period 2003-2013.

Freak waves in vector system. Extreme wave events, also referred to as freak or rogue waves are mostly as known oceanic phenomena responsible for a large number of maritime disasters. These waves, which have height and steepness much greater than expected from the sea average state, not only appear in oceans but also in the atmosphere, in optics, in plasmas, in superfluids, in Bose-Einstein condensates. In a variety of complex systems such as Bose-Einstein condensates, optical fibers, and financial systems, several amplitudes rather than a single one need to be considered. Models describing rogue wave phenomena involving more than one wave amplitude are, for instance, the three wave interaction, the Gross-Pitaevskii and the Manakov system. I contributed to the field of rogue waves by constructing new multi-parametric vector soliton solution of the Manakov [J58] and the three-wave systems [J50]. I found the expression of multi-parametric, rational or semi-rational deterministic freak waves [J23] and contributed to their experimental observation in nonlinear optics [J13]. Remarkably, I showed the existence of rogue waves in the defocusing regime [J34,J27].

Dispersive shock waves. Dispersive shock waves (DSWs) are expanding regions filled with fast oscillations that stem from the dispersive regularization of classical shock waves. Originally introduced in collisionless plasmas and water waves, they have been the focus of intense multidisciplinary efforts that have established their universal role in atom condensates, light propagation, oceanography, quantum liquids, electron beams, and magma flow. In this context, I studied the emergence of DSW in different optical systems, encompassing fibers, cavities and quadratic crystals. I showed that dispersive shock formation can occur during second harmonic generation in quadratic crystals [J59], showing also a competition with modulational instability [J48]. I showed that DSW can be perturbed by high order dispersion [J40] and can emit resonant radiation, both in the context of fibers [J51,J41] and fiber resonators [J37]. I pursued this line of research after my arrival in Lille, and I will describe the recent achievements in more details in Chapter 3.

Modelling of ultrabroadband phenomena in quadratic crystals. The modeling of extreme nonlinear spectral broadening (or supercontinuum generation) of optical pulses propagating in nonlinear medium, as well as the compression of optical pulses down to single-cycle duration, is an active area of research. The overwhelming majority of studies on these topics deals with third order nonlinear media, characterized by Kerr and Raman processes. There are a few experimental works that report the observation of extremely broad spectrum generation by exploiting second order nonlinear materials such as Lithium Niobate (LN), Lithium Tantalate (LT) and Potassium Dihydrogen Phosphate (KDP) or Potassium Titanium Oxide Phosphate (KTP). Theoretical research efforts on the modelling of this kind of broadband phenomena are more limited. When second order nonlinearities are considered, the usual approach was to write coupled equations for the separated frequency bands relevant for the process. However, when ultra-broadband $\chi^{(2)}$ phenomena take place, the fundamental frequency and harmonics bands merge, generating a single broad spectrum, as observed in some experiments. Obviously, in these cases the coupled envelope description of the propagation fails due the frequency overlapping of the distinct bands. An important result of my work are models for the description of single-cycle and ultrabroadband electric field phenomena in dispersive quadratic, isotropic or birefringent media [J73,J72,J68,J65,J54,J52,J36]. These models can be easily solved with a modest computational effort, which has permitted to understand experiments of supercontinuum generation in quadratic crystals.

Theory and experiments on three wave solitons. Solitary waves in quadratic materials have been the subject of an intense renewal of interest from both theoretical and experimental viewpoints. Two types of solitary waves that were both predicted in the early seventies are being studied. On one hand, one finds solitary waves that result from a balance between nonlinearity and diffraction (or dispersion). On the other hand, quadratic media were shown to support solitary waves that result from energy exchanges between diffractionless (or dispersionless) waves of different velocities. This type of solitary wave, known as three wave interaction (TWI) soliton, is ubiquitous in nonlinear wave systems and has been reported in such diverse fields as plasma physics, hydrodynamics, acoustics, and nonlinear optics. In this field I gave several theoretical and experimental contributions. Form the theoretical side, I found novel analytical solutions of the three wave interaction model in form of simultons and accelerating solitons [J93,J91,J85], and developed spectral and numerical methods for the solution of TWI equations [J64]. On the application side, I proposed soliton based schemes for frequency conversion [J84] and pulse train generation [J82]. From the experimental side, I contributed to the first observation of bright and bright-dark solitons of TWI equations [J77,J71,J62], and to develop a scheme to realize a mode-locked laser exploiting TWI solitons [J63].

Plasmonic waveguides. The miniaturization of photonic devices for confining and guiding electromagnetic energy down to a nanometer scale is one of the biggest challenges for the information technology industries. When the size of a conventional optical circuit is reduced to the nanoscale, the propagation of light is limited by diffraction. One way to overcome this limit is through surface plasmon polaritons, which are evanescent waves trapped at the interface between a medium with a positive real part of the dielectric constant and one with a negative real part of the dielectric constant, such as metals in the visible range. Even though this phenomenon has been known for a long time, in the past few years there is renewed interest in this field, mainly motivated by the will to merge integrated electronic circuits to photonic devices. In this field I studied guiding structures, such as waveguide arrays, where I found peculiar diffractive phenomena, and showed the possibility of diffraction management on a subwavelength scale [J81]. Then I derived the dispersion relation for nanoparticle chains by exploiting the Mie scattering method and calculated the complex band diagram solving the dispersion relation for lossy particles [J75,J70].

Nonlinear plasmonics. The linear optical response of noble metal nanostructures, such as thin films, gratings, multilayers, and nanoparticles has been exploited to achieve extreme light concentration and manipulation. Also, the huge nonlinear optical response of metallic nanostructures after intense excitation with fs-laser pulses has attracted increasing attention in view of the potential to achieve ultrafast all-optical control of light beams. Usually, the nonlinear response of the metal is modeled as a pure Kerr effect. This model, though perfectly describing nonresonant nonlinearities of electronic type that respond extremely fast to a driving electric field, turned out to be unsuitable for fs and ps optical pulses. Actually, the values of the $\chi^{(3)}$ coefficient, measured by the z-scan technique, which can be found in the literature, differ by up to two orders of magnitude, clearly demonstrating that an instantaneous Kerr model is inadequate to describe the nonlinear response of metallic nanostructures. In this context I derived a delayed third-order nonlinear response suitable for the description of optically thin metallic structures [J60,J44]. The outcome of this model has been quantitatively compared with experimental results from pump-probe spectroscopy on thin gold films [J56], multilayers [J31], and semiconductor nanoparticles [J61,J43].

After ten years spent in Brescia, in 2014 I was recruited as Research Officer at PhLAM in Lille, in the Photonics group. Here I started the studies of the nonlinear phenomena which take place in fibers with longitudinal modulation of dispersion, in strict collaboration with Alexandre Kudlinski and Arnaud Mussot. The good synergy with this research team has been corroborated by the acceptance of an ANR research project in the same year, devoted to the study of extreme waves. As the principal investigator of this project I was able to build my own research team, composed by two PhD students (Carlos Mas Arabi and Tomy Marest) and one post-doc (Gang Xu). In 2015 I got my present position of CNRS researcher (CR1).

In this Manuscript I will resume the principal research activities that I am leading from 2014 at PhLAM, which can be grouped into four themes. The first research area consist in the study of instabilities in passive ring cavities. I opened this line at my arrival at PhLAM, with the first theoretical study of modulation instability in dispersion oscillating fiber cavities. Following this work, we have obtained several other theoretical and experimental results, which are summarized in Chapter 1. The great part of these results have been obtained by François Copie during his PhD thesis, of which I am co-supervisor with Anraud Mussot.

The second subject is the nonlinear stage of modulational instability in optical fibers. These studies are carried on in the framework of the CEMPI LABEX project, which links PhLAM and the mathematics department "Paul Painlevé". The principal results, issued by a fruitful collaboration between mathematicians, theoretical and experimental physicists, are summarized

in Chapter 2.
The third subject are shock waves. I started the theoretical studies on shock waves in collaboration with Stefano Trillo during my post-doc in Brescia. At PhLAM I exploited my theoretical knowledge to design and supervise experiments in optical fibers. The experimental results have been obtainen mainly by Gang Xu during his post-doc, and by Tomy Marest during his first year of PhD, both under my supervision in the framework of the ANR project *Nonlinear dynamics of Abnormal Wave Events* (NoAWE). These results are reported in Chapter 3.
The fourth theme is the interaction between nonlinear and dispersive waves in optical fibers with varying dispersion. A good part of the job has been performed by Flavie Braud during his PhD thesis (informal supervision) and by Tomy Marest. These results are reported in Chapter 4.
The last part of the Thesis, composed of four Appendices, reports a complete list of my publications, my Curriculum Vitae, a summary of teaching and supervision activities, of responsibilities and of scientific collaborations.

CHAPTER 1

Instabilities in passive fiber ring cavities

This Chapter reports the outcomes of our theoretical and experimental studies of instabilities in passive ring cavities composed of pieces of fiber with different dispersion. We describe the derivation of an extended version of the Lugiato-Lefever equation, which permits to model dispersion oscillating cavity and it has proved to hold valid well beyond the mean field approximation. We review the theory of Turing (modulational) and Faraday (parametric) instability in inhomogeneous fiber cavities. We report the experimental demonstration of the generation of stable Turing and Faraday patterns in the same device, which can be controlled by changing the detuning and/or the input power. Moreover, we show experimental records of the round-trip-to-round-trip dynamics of the spectrum, which point out that Turing and Faraday instabilities not only differ by their characteristic frequency but also by their dynamical behavior.

1.1 Introduction

Modulation instability (MI) is probably the most basic, interdisciplinary and studied nonlinear phenomenon, which appears in disparate physical settings described by dispersive and nonlinear partial differential equations [1]. It essentially consists in the exponential growth of a weak periodic perturbation of an intense continuous wave (CW) as a result of the interplay between dispersion and nonlinearity. The underlying mechanism is a nonlinear phase matching of the four-wave mixing between the CW pump and sidebands. MI is a central process in nonlinear optics at the origin of complex nonlinear phenomena such as Fermi-Pasta-Ulam recurence [2], [3], Peregrine and Kuznetsov-Ma soliton excitation [4], [5], supercontinum generation [6], [7], development of rogue waves [8] or frequency combs [9], [10]. It has been observed in free running fiber systems in the early 80's [11] and later on exploited to develop large band fiber optical parametric amplifiers for telecommunication applications [12], [13], short pulse amplifications [14] or signal processing [15]. In passive cavities, MI is usually referred to as Turing instability, by analogy with the pattern formation in chemical reactions [16], [17], and besides its fundamental interest, it has a wealth of applications ranging from optical memory [18], self referencing [19], [20] to ultra-stable optical clock [19]. Quite recently, the idea of periodically modulating one parameter along fiber length has been investigated in the context of

MI in free running configurations [21]. It has been shown that it adds a new degree of freedom to these fiber systems leading to the formation of new quasi-phase matched waves [21]–[24]. In passive cavities, it can be achieved by periodically modulating group velocity dispersion [25], nonlinearity [26] or losses [27]. It significantly modifies the dynamics of these cavities where, in addition to Turing instabilities observable in uniform cavities, the periodic modulation acts as a forcing term leading to the birth of parametric resonances [28], also known as Faraday instabilities in direct analogy with the seminal discovery of Faraday in a vertically vibrating bowl [29]. We first theoretically predicted [25] and then demonstrated experimentally [30] the birth of parametric sidebands in dispersion oscillating cavities. We showed for the first time that while Turing and Faraday instabilities have different physical origins, they can exist within the same physical system. Following this first observation in the steady state regime, we have investigated the round-trip-to-round-trip behaviour, revealing a complex dynamics during the switching from one instability regime to the other [31].

The Lugiato-Lefever Equation (LLE) [32], [33] is the fundamental tool exploited to study theoretically and numerically nonlinear dynamics in passive cavities. We have extended LLE to the description of inhomogeneous cavities, and showed its validity well beyond the assumption (mean-field) under which it has been originally derived [25]. We then proposed a rigorous justification of why LLE can describe situations that goes beyond the mean field approximation [34].

This Chapter reports the main results of our investigations on dispersion oscillating fiber ring cavities. First, we describe an original and rigorous derivation of LLE model under minimal assumptions, which applies both to uniform and dispersion oscillating cavities. Secondly, we review the theory of modulational and parametric instabilities in homogeneous and passive resonators. Lastly, we report our main experimental results obtained in these cavities showing the observation of Turing and Faraday instabilities within the same physical system.

1.2 Rigorous derivation of LLE

Let us consider the passive fiber ring resonator sketched in Fig. 1.1(a). The input is a train of equally spaced pulses, perfectly synchronized, i.e. the cavity length is such that after each cavity transit, the recirculating pulse perfectly overlaps in time with the next pulse of the train. The pulses duration is assumed to be much longer than the typical MI period, so that we can consider a continuous wave pumping. The electric field at the coupler is modelled by the Ikeda map [35], describing the cavity boundary conditions:

$$E^{(n+1)}(Z=0,T) = \theta E_{in}(T) + \rho e^{i\phi_0} E^{(n)}(Z=L,T), \tag{1.1}$$

where Z measures the distance along the fiber, T is the retarded time, E and E_{in} are the intracavity and input electric field envelopes, $\rho^2+\theta^2=1$ are the reflection and transmission coefficients, $\phi_0=\beta_0 L$ is the linear phase detuning, $\beta_0=\omega_0 n(\omega_0)/c$ is the wavenumber at the laser frequency ω_0 and L is the cavity length, n being an integer counting the round-trip number. The electric field envelope evolves inside the cavity (i.e. for values of the spatial variables $0 \le Z \le L$) according to the nonlinear Schrödinger equation (NLSE):

$$i\frac{\partial E^{(n)}}{\partial Z} - \frac{\beta_2(Z)}{2}\frac{\partial^2 E^{(n)}}{\partial T^2} + \gamma |E^{(n)}|^2 E^{(n)} = 0, \tag{1.2}$$

where $\beta_2(Z)$ is the group velocity dispersion (GVD) and γ is the nonlinear coefficient of the fiber. The function $\beta_2(Z)$ is periodic and its period is in general a fraction of the cavity length L [36].

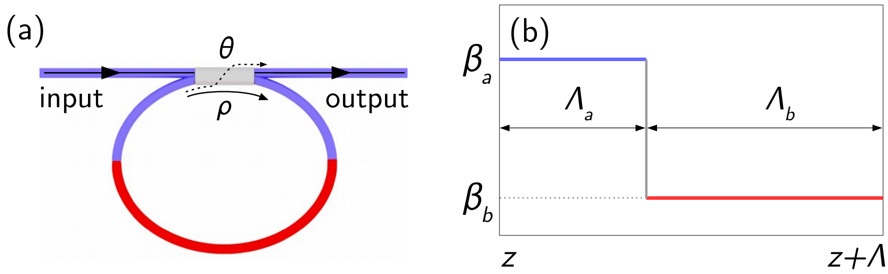

Figure 1.1 – (a) Schematic illustration of a non-uniform passive fiber ring cavity. (b) Piecewise constant dispersion map over one period of the GVD.

The rest of the Chapter is focused on the simplest case where the periodicity of the dispersion is equal to the cavity length. In general both the dispersion and the nonlinearity change, however in our experimental range we can assume that only the GVD changes and γ is constant.

The LLE has been originally derived from Eqs. (1.1-2.1) in the so called mean-field approximation [32], [37], i.e. assuming that the intracavity field does not evolve significantly over a round-trip. This entails several strong constraints: the cavity is short with respect to nonlinear and dispersion length, the intensity loss at the coupler and the cavity detuning are small. However, LLE holds valid even when several of these assumptions are violated. A typical example is the parametric instability in a dispersion oscillating cavity, where the dispersion and the field change rapidly over a single round-trip [25]. *In the following, it is showed that the only assumption needed in order to derive LLE is that only one longitudinal mode of the cavity is excited.*

Let's start by performing a phase rotation:

$$A^{(n)}(Z,T) = E^{(n)}(Z,T)\exp[i\beta_0 Z],$$

in order to incorporate the rapid phase variation into NLSE and remove it from the boundary conditions. The equations for the fast variable A are:

$$A^{(n+1)}(Z=0,T) = \theta E_{in}(T) + \rho A^{(n)}(Z=L,T), \tag{1.3}$$

$$i\frac{\partial A^{(n)}}{\partial Z} + \beta_0 A^{(n)} - \frac{\beta_2(Z)}{2}\frac{\partial^2 A^{(n)}}{\partial T^2} + \gamma|A^{(n)}|^2 A^{(n)} = 0. \tag{1.4}$$

Now the spatial variable is allowed to assume all values from 0 to infinity, i.e. the cavity is unfolded. Even if Z is a continuous variable, the field is physically accessible only at the coupler, i.e. at distances $Z = nL$. The boundary conditions are incorporated in the propagation equation with the aid of the delta function, so that Eqs. (1.3-1.4) can be written in the following equivalent compact way:

$$i\frac{\partial A}{\partial Z} + \beta_0 A - \frac{\beta_2(Z)}{2}\frac{\partial^2 A}{\partial T^2} + \gamma|A|^2 A = i\sum_n \delta(Z-nL)\left[\theta E_{in}(T) + (\rho-1)A\right]. \tag{1.5}$$

The Dirac delta comb can be written in Fourier series thanks to the Poisson summation formula as follows ($k = 2\pi/L$):

$$\sum_n \delta(Z-nL) = \frac{1}{L}\sum_n e^{in\frac{2\pi}{L}Z} = \frac{1}{L}\sum_n e^{inkZ}, \tag{1.6}$$

which inserted into Eq. (1.5), gives:

$$i\frac{\partial A}{\partial Z}+\beta_0 A-\frac{\beta_2(Z)}{2}\frac{\partial^2 A}{\partial T^2}+\gamma|A|^2A=\frac{i}{L}\sum_n e^{inkZ}\left[\theta E_{in}(T)+(\rho-1)A\right]. \tag{1.7}$$

In order to recognize exponential terms oscillating at the same rate, it is convenient to come back to the slow variable through the substitution $E = A\exp[-i\beta_0 Z]$:

$$i\frac{\partial E}{\partial Z}-\frac{\beta_2(Z)}{2}\frac{\partial^2 E}{\partial T^2}+\gamma|E|^2E=\frac{i\theta}{L}E_{in}\sum_n e^{i(nk-\beta_0)Z}+i\frac{\rho-1}{L}E\sum_n e^{inkZ}. \tag{1.8}$$

Equation (1.8) is a NLSE forced by two combs with equal wavenumber spacing $k = 2\pi/L$ and a relative shift β_0. The solution of (1.8) can be written as a sum of slowly-varying envelopes, which modulates the longitudinal modes of the cavity, as:

$$E(Z,T)=\sum_n E_n(Z,T)e^{iknZ}. \tag{1.9}$$

It is of fundamental importance to choose the correct forcing terms for each mode, in order to neglect the fast-rotating exponential in favor of the slowly evolving ones. When the intracavity power is reasonably small, we can assume that we have only one mode present in the cavity, i.e.

$$E(Z,T)=E_0(Z,T). \tag{1.10}$$

This assumption permits to describe all the phenomena we observe in our experiments and in most of the situations. Only when several longitudinal mode are present in the cavity, as observed recently in a tristable resonator [38], the single LLE ceases to be valid and a more complex model has to be used [39]. *It is worth noting that the single longitudinal mode operation is the only hypothesis that has been made so far*.
By retaining only the quasi-phase-matched forcing terms in (1.8), i.e. the terms that are multiplied by the exponentials with the smallest argument, gives:

$$i\frac{\partial E_0}{\partial Z}-\frac{\beta_2(Z)}{2}\frac{\partial^2 E_0}{\partial T^2}+\gamma|E_0|^2E_0=\frac{i\theta}{L}E_{in}e^{i\delta Z/L}+i\frac{\rho-1}{L}E_0, \tag{1.11}$$

where the cavity detuning δ is defined as follows:

$$\delta = mk-\beta_0,\ m=\arg\min_n|nk-\beta_0|, \tag{1.12}$$

that implies $\delta\in[-\pi,\pi]$. This fixes the detuning validity range of LLE. Any choice $|\delta|>\pi$ means the slowest oscillating term has been neglected in favor of a rapid one, which means that we have chosen the wrong n in the first summation in (1.8). *Note that it is not necessary to assume that the detuning is small.*
The exponential can be removed from the pump by the phase rotation $E_0(Z,T)=U_0(Z,T)\exp[i\delta Z/L]$, to find the LLE in the usual (dimensional) form:

$$i\frac{\partial U_0}{\partial Z}-\frac{\beta_2(Z)}{2}\frac{\partial^2 U_0}{\partial T^2}+\gamma|U_0|^2U_0=\frac{i\theta}{L}E_{in}+\left(\frac{\delta_0}{L}-i\frac{\alpha}{L}\right)U_0, \tag{1.13}$$

where $\alpha = 1-\rho$. The intrinsic fiber losses, that have been neglected up to now, can be accounted for by taking α as the total round-trip losses.

Equation (1.13) can be written in a convenient non-dimensional form as follows:

$$i\frac{\partial u}{\partial z} - \frac{\beta(z)}{2}\frac{\partial^2 u}{\partial t^2} + |u|^2 u = (\delta - i\alpha)u + iS, \tag{1.14}$$

where $z = Z/L$, $t = T/T_0$, $u = U\sqrt{\gamma L}$, $T_0 = \sqrt{|\beta_2^{av}|L}$; $S = \theta u_{in}(t)$, and $\beta(z) = \beta_2(z)/|\beta_2^{av}|$, β_2^{av} being the average group velocity dispersion. The normalized periodic dispersion profile (normalized period $\Lambda = 1$) is of the form $\beta(z) = \beta_{av} + \beta_m f(z)$, where β_m is the amplitude and $f(z)$ the shape of the dispersion modulation.

In the following Section, we report the linear stability analysis of Eq. (1.14), which permits to characterize the different kind of instabilities that can rise in a dispersion oscillating fiber cavity pumped by a CW source.

1.3 Linear stability analysis

The stationary solution of Eq. (1.14), $u_0(z,t) = \sqrt{P_u}$, which can be assumed real without loss of generality, follows from the steady state response $P = P(P_u)$, explicitly $P = P_u[(P_u - \delta)^2 + \alpha^2]$, where $P = |S|^2$ is the input power and $P_u = |u_0|^2$ is the intracavity power. The steady state response is bistable whenever $\delta^2 > 3\alpha^2$. In this case the function $P_u(P)$ is multivalued in the range $P(P_u^+) \leq P \leq P(P_u^-)$ where $P_u^{\pm} = (2\delta \pm \sqrt{\delta^2 - 3\alpha^2})/2$ stands for the knees of the bistable response. In the multivalued region, out of the three possible solutions, only the lower and the higher ones are stable. The intermediate one, associated to a negative slope, is dynamically unstable so it is not reachable in the experiments.

The cavity steady states can destabilize through the exponential growth of modulations which can be due to a Turing (modulation instability) or Faraday (parametric instability) mechanism, respectively. The Turing instability is characteristic of a uniform cavity (in a periodic case it is affected only by the average quantities), whereas the Faraday instability is a consequence of the parametric resonance due to the forcing, and hence the characteristics of the instability are affected by the period and the strength of the perturbation. However both follow from a linear stability analysis of the steady solution u_0, which at some point needs to be specialized to describe the two mechanisms. To this end, let us consider the evolution of a perturbed solution $u(z,t) = \sqrt{P_u} + [p(z,t) + iq(z,t)]$, where it is assumed that the real functions p, q are much smaller than u_0.

By linearization of Eq. (1.14), a linear system ruling the evolution of the perturbation is obtained:

$$\frac{\partial p}{\partial z} - \frac{\beta(z)}{2}\frac{\partial^2 q}{\partial t^2} + (P_u - \delta)q + \alpha p = 0, \tag{1.15}$$

$$\frac{\partial q}{\partial z} + \frac{\beta(z)}{2}\frac{\partial^2 p}{\partial t^2} - (3P_u - \delta)p + \alpha q = 0. \tag{1.16}$$

Taking the Fourier transform in time $[\hat{p}(z,\omega) = \int u(z,t)e^{i\omega t}dt]$ of this system leads, for each frequency, to :

$$\frac{d}{dz}\begin{bmatrix} \hat{p} \\ \hat{q} \end{bmatrix} = \begin{bmatrix} -\alpha & -g(z) \\ h(z) & -\alpha \end{bmatrix}\begin{bmatrix} \hat{p} \\ \hat{q} \end{bmatrix}, \tag{1.17}$$

where $g(z) = \frac{\beta(z)}{2}\omega^2 + P_u - \delta$ and $h(z) = \frac{\beta(z)}{2}\omega^2 + 3P_u - \delta$.

1.3.1 Uniform cavity: Turing instability

Let us start by considering a uniform cavity, where $\beta_m = 0$, $\beta(z) = \beta_{av}$. System (1.17) is similar to a damped harmonic oscillator, whose oscillation spatial frequency (wavenumber) is:

$$k_{av} = \sqrt{h_{av} g_{av}} = \sqrt{\left(\frac{\beta_{av}}{2}\omega^2 + 2P_u - \delta\right)^2 - (P_u)^2}. \tag{1.18}$$

Its eigenvalues, which rule the z evolution, read $-\alpha \pm i k_{av}$. When the detuning δ is sufficiently high, k_{av} can become imaginary in a certain range of ω, and the solution of Eqs. (1.17) involves two exponentials with real argument. In this range, if $|k_{av}| > \alpha$ the perturbations $\hat{p}, \hat{q}$ grows exponentially $\propto \exp[G(\omega)z]$ with growth rate $G(\omega) = -\alpha + \sqrt{-h_{av} g_{av}}$, entailing modulation instability of the stationary solution [37]. The most unstable Turing frequency $\omega = \omega_T$ and its corresponding gain, can be easily calculated from the eigenvalues to be:

$$\omega_T = \sqrt{\frac{2}{\beta_{av}}(\delta - 2P_u)}, \;\; G(\omega_T) = P_u - \alpha. \tag{1.19}$$

It is worth recalling that, unlike the cavityless fiber configuration where MI occurs only in the anomalous GVD regime and without threshold, in the cavity, MI occurs also with normal GVD and has a threshold $P_u = \alpha$, obtained by imposing $G = 0$ in Eq. (1.19).
The linear stability analysis presented here allows to determine the conditions of instability with respect to small perturbations but does not provide any information on the dynamics of large amplitude modulated states. In other words, MI is the generating mechanism of the Turing pattern but only in a subset of the unstable region, the growth of the sideband can generate a stable pattern. This has been analyzed in details in [40].

1.3.2 Periodically modulated cavity: Faraday instability

Before proceeding with the analysis, it is useful to factorize the effect of the losses through the transformation $[\hat{p}, \hat{q}] = [\tilde{p}, \tilde{q}]\exp(-\alpha z)$, which transforms Eqs. (1.17) into a one degree of freedom Hamiltonian system with canonical coordinates $[\tilde{p}, \tilde{q}]$:

$$\frac{d}{dz}\begin{bmatrix} \tilde{p} \\ \tilde{q} \end{bmatrix} = \begin{bmatrix} 0 & -g(z) \\ h(z) & 0 \end{bmatrix}\begin{bmatrix} \tilde{p} \\ \tilde{q} \end{bmatrix}. \tag{1.20}$$

Since the coefficients in the equation are z-periodic with period Λ, Floquet theory applies. This amounts to study the evolution over one period Λ ($\Lambda = 1$ in this Chapter), to obtain the Floquet map Φ, which is the two by two real matrix defined by $[\tilde{p}(\Lambda), \tilde{q}(\Lambda)]^T = \Phi[\tilde{p}(0), \tilde{q}(0)]^T$. As a result $[\tilde{p}(n\Lambda), \tilde{q}(n\Lambda)]^T = \Phi^n[\tilde{p}(0), \tilde{q}(0)]^T$. Note that Φ necessarily has determinant one, since it is obtained by integrating a Hamiltonian dynamics, which preserves phase space volume. As a consequence, the two eigenvalues $\lambda^{\pm}$ of Φ are constrained to lie either both on the unit circle, or both on the real axis. Only in the latter case the system can be unstable, the instability being associated with $|\lambda| > 1$ according to Floquet theory.
Since the system (1.20) is not autonomous, it cannot be solved analytically in general. Nevertheless, the above observations pertmit to obtain some information about its stability for relatively small β_m, which, importantly, holds valid regardless of the specific shape of the forcing $f(z)$ [41]. To see this, let us start from the unperturbed limit $\beta_m = 0$, $\beta(z) = \beta_{av}$. It is then straightforward

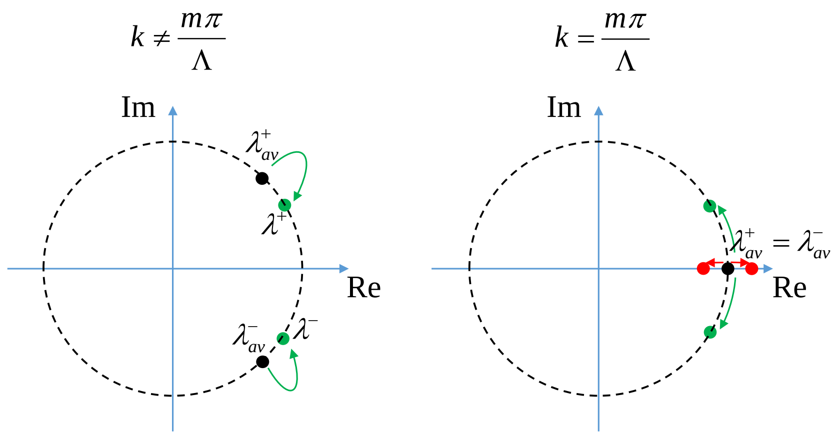

Figure 1.2 – Sketch illustrating, in the complex plane, the effect of the forcing term $f(z)$ on the eigenvalues of the Floquet map (1.21). Black dots correspond to the unperturbed eigenvalues lying on the unit circle (dashed line). Colored dots show the new position of the eigenvalues after switching on the perturbations, leading to a stable regime when $k \neq \frac{m\pi}{\Lambda}$ (left sketch) and an unstable one when $k = \frac{m\pi}{\lambda}$ (right sketch).

to integrate the system (1.20). The Floquet map is then given by:

$$\Phi_{av} = \begin{bmatrix} \cos(k_{av}\Lambda) & -\frac{g_{av}}{k_{av}}\sin(k_{av}\Lambda) \\ \frac{k_{av}}{g_{av}}\sin(k_{av}\Lambda) & \cos(k_{av}\Lambda) \end{bmatrix}. \tag{1.21}$$

The eigenvalues of Φ_{av} can be easily computed as:

$$\lambda^{\pm}_{av} = \exp(\pm i k_{av}\Lambda). \tag{1.22}$$

The wavenumber $k_{av}(\omega)$ is assumed to be real, i.e. the uniform cavity is stable with respect to perturbations at frequency ω. What happens by switching on the periodic dispersion described by $f(z)$? The system (1.20) becomes non-autonomous and hence it is no longer possible, in general, to give a simple closed form expression of the eigenvalues. Nevertheless, for sufficiently small β_m, the eigenvalues of Φ must be close to the eigenvalues $\lambda^{\pm}_{av}$. Two cases can then be distinguished:

1. Off-resonant case $k_{av} \neq \frac{m\pi}{\Lambda}$. Since $k_{av}\Lambda \neq m\pi$, it follows from Eq. (1.22) that $\lambda^-_{av} = (\lambda^+_{av})^*$, *are distinct and they both lie on the unit circle, away from the real axis*. They then must remain on the unit circle under perturbation since, for the reasons explained above, they cannot move into the complex plane away from the unit circle. A pictorial description of this situation is shown in the left panel of Fig. 1.2. In this case, the stationary solution is linearly stable under a sufficiently small perturbation $\beta_m f(z)$ and this statement does not depend on the precise form of $f(z)$.

2. On-resonant case $k_{av} = \frac{m\pi}{\Lambda}$. It follows from Eq. (1.22) that $\lambda^+_{av} = \lambda^-_{av} = \pm 1$ (upper or lower sign holds for m even or odd, respectively) is a doubly degenerate eigenvalue of Φ_{av}. Under a small perturbation, the degeneracy can be lifted and two real eigenvalues can be created, one greater than one, one less than one in absolute value. The system has then become unstable. A pictorial description of this situation is shown in the right panel of Fig. 1.2. In principle, under

very peculiar perturbations, the eigenvalues might also move along the circle implying that the system remains stable. However, for the most common perturbations (sinusoidal, square wave, sawtooth, comb, ...), the system, for some m, destabilizes under an arbitrarily small perturbation, following the split of the eigenvalues on the real axis at the degenerate points ± 1.
To resume, when the forcing is switched on, the instability sets in under the resonant condition $k_{av} = \frac{m\pi}{\Lambda}$. Recalling the expression of $k_{av} = k_{av}(\omega)$ in Eq. (1.18), it is straightforward to show that the m−th order resonance is fulfilled at frequency $\omega = \omega_m$, where:

$$\omega_m = \sqrt{\left\{\frac{2}{\beta_{av}}(\delta - 2P_u)\right\} \pm \left[\frac{2}{\beta_{av}}\sqrt{\left(\frac{m\pi}{\Lambda}\right)^2 + P_u^2}\right]}. \tag{1.23}$$

The resonance condition:

$$k_{av}(\omega_m) = m\frac{\pi}{\Lambda} = m\frac{k_g}{2} \tag{1.24}$$

is the condition of *parametric resonance, i.e. the natural spatial frequency of the unperturbed harmonic oscillator (k_{av}) is equal to a multiple of half the forcing spatial frequency ($k_g = \pi/\Lambda$)* [28].
Let us return now to the original (damped) system for the perturbations $[\hat{p}, \hat{q}]$. The Floquet map is simply given by $\Psi_{av} = \exp(-\alpha\Lambda)\Phi_{av}$, whose eigenvalues read as:

$$\sigma_{av}^{\pm} = \exp(-\alpha\Lambda)\lambda_{av}^{\pm} = \exp[(-\alpha \pm ik_{av})\Lambda]. \tag{1.25}$$

This means that the eigenvalues $\sigma_{av}^{\pm}$ lie in the complex plane either on a circle of radius $\exp(-\alpha\Lambda)$ (case 1), or on the real axis (case 2). Now the perturbation can grow only if the forcing β_m is sufficient to push one of the eigenvalues outside the unit circle. In this case, the perturbations $\hat{p}, \hat{q}$ will experience an exponential growth with rate $G(\omega) = \ln(\max|\sigma^{\pm}|)/\Lambda$. This means that there is a threshold on β_m for the onset of the parametric instability. On the same footing, for a fixed β_m, there exist a power threshold for the parametric instability to appear.
To summarize, the Faraday instability appears in general at multiple frequencies ω_m given by Eq. (1.23) which depend on the period of the forcing and represent the tips of the unstable regions known as Arnold tongues, whereas a threshold in the strength of the forcing (or intracavity power) exists which depends on the losses (the higher the losses, the higher the threshold) and on the specific shape of the perturbation (though no general analytical formulas can be given for the threshold).
The stability analysis presented here allows to determine the conditions of parametric instability with respect to small perturbations but does not provide any information on the dynamics of large amplitude modulated states. In other words, parametric instability is the generating mechanism of the Faraday pattern but only in a subset of the unstable region the growth of the sideband can generate a stable pattern. Above this region, the Faraday pattern becomes unstable and the behavior of the cavity chaotic.

1.3.3 Piecewise constant dispersion

An example of practical interest where the Floquet analysis can be performed *analytically* is a cavity with a piecewise constant dispersion [25]. This case corresponds to the experimental set-up we used, where the intracavity loop is made of two pieces of different fibers spliced together. The fiber-ring thus exhibit a step-like longitudinal dispersion profile (see Fig. 1.1(b)). The Floquet map is given by

$$\Psi = \exp(-\alpha\Lambda)\Phi_a\Phi_b, \tag{1.26}$$

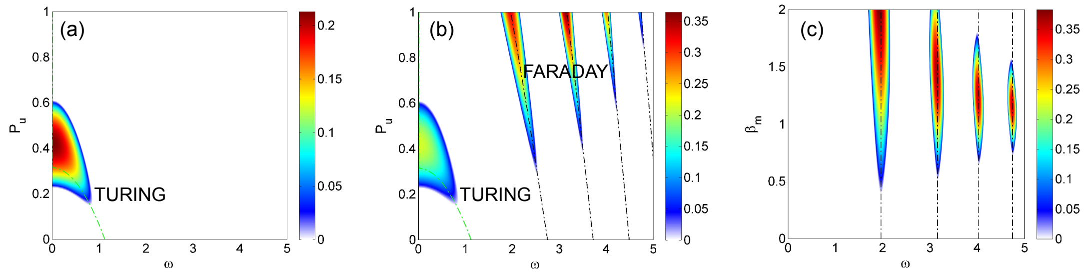

Figure 1.3 – Color level plot of growth rate $G(\omega)$. (a) Uniform cavity $\beta_{av} = 1$, $\beta_m = 0$, $\Lambda = 1$. The dashed green curve indicates the peak gain calculated from Eq. (1.19). (b) Modulated cavity $\beta_{av} = 1$, $\beta_{a,b} = 1 \pm 1.5$, $\Lambda_a = \Lambda_b = 0.5$. The dashed black curves indicates the peak gain calculated from Eq. (1.23) for $m = 1, 2, 3, 4$. (c) Modulated cavity $\beta_{av} = 1$, $P_u = 1$, $\Lambda_a = \Lambda_b = 0.5$. In all three plots, $\delta = \pi/5$, $\alpha = 0.15$.

where $\Phi_{a,b}$ has the expression (1.21) calculated for a dispersion $\beta(z) = \beta_{a,b}$, where the two pieces of fiber has length $\Lambda_{a,b}$, such that $\Lambda_a + \Lambda_b = \Lambda$ and the average dispersion is $\beta_{av} = (\beta_a\Lambda_a + \beta_b\Lambda_b)/\Lambda$. The eigenvalues of Ψ are given by

$$\sigma^{\pm} = \frac{D}{2} \pm \sqrt{\frac{D^2}{4} - W}, \tag{1.27}$$

where

$$D = e^{-\alpha\Lambda}\left[2\cos(k_a\Lambda_a)\cos(k_b\Lambda_b) - \frac{g_a h_b + g_b h_a}{k_a k_b}\sin(k_a\Lambda_a)\sin(k_b\Lambda_b)\right], \tag{1.28}$$

and $W = e^{-2\alpha\Lambda}$. We have parametric instability if $|D| > (1 + W)$, with gain $G(\omega) = \ln(\max|\sigma^{\pm}|)/\Lambda$. In Fig. 1.3 we report some examples of analytically calculated instability gain. Figure 1.3(a) shows the gain as a function of perturbation frequency and intracavity power for a homogeneous cavity. In this case, we observe a branch located around zero frequency, which can generate a stable Turing pattern. Figure 1.3(b) shows the gain for a modulated cavity in the same operating conditions. The Turing branch survives, and we see the generation of several branches due to the periodic forcing. These parametric instability branches (Arnold tongues) are the generating mechanism for the Faraday patterns. The existence of both Turing and Faraday branches in the same device allows us to observe the competition between the two phenomena. Figure 1.3(c) shows the Arnold tongues as a function of the forcing amplitude β_m for a fixed power. Due to nonzero losses α, there exist a threshold for the onset of the instability (as discussed above), which is generally different for each tongue.

1.3.4 Chart of instabilities

The behavior of the system is controlled by two main parameters, namely power and normalized detuning $\Delta = \delta/\alpha$, which are easily accessible experimentally. The scenario is summarized in Fig. 1.4 which shows the domains of the different instabilities in the parameter plane (Δ, P_u) for a uniform cavity (Fig. 1.4 (b)), and for a dispersion modulated cavity (Fig. 1.4(d)) when the average dispersion is normal ($\beta_2^{av} > 0$). For better clarity, the corresponding steady state responses are also reported in Figs. 1.4(a) and (c), respectively. We fixed a large value of detuning of $\Delta = 6.25$ because it allows to capture all the richness of the setup with the excitation of both regimes of

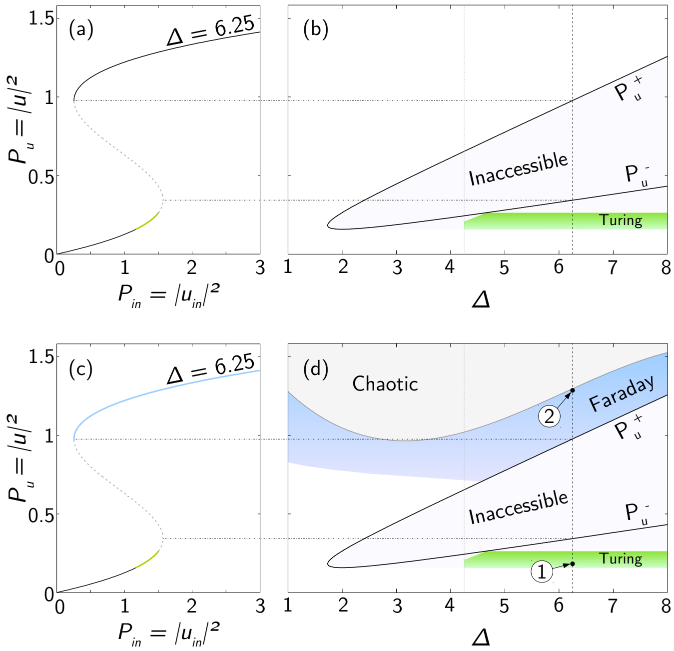

Figure 1.4 – (a) Normalized steady-state curve for a detuning value $\Delta = 6.25$. (b) Instability domains of a uniform cavity in the plane (Δ,P_u) in the average normal dispersion regime ($\beta_2^{av} > 0$). The "Inaccesible" region corresponds to the negative-slope branch of the steady-state of (a). The green domain represents the region where Turing modulated structures can be excited. (c-d) Same as (a-b) except that the periodic dispersion is switched on. The Faraday domain of instability appears on the upper branch (for higher powers the Faraday structures destabilize giving rise to chaotic spatio-temporal evolutions). Parameters: $\Lambda_a = 0.97$, $\Lambda_b = 0.03$, $\beta_a = 1.5$, $\beta_b = -14$, $\alpha = 0.157$, $\theta^2 = 0.1$, $\Lambda = 1$: the period of the GVD equals the length of the resonator.

instability. Note that it corresponds to the detuning value used in the experiments described below. For $\Delta \geq \sqrt{3}$, the cavity is bistable [32], [37], and exhibits an unstable negative slope branch for $P_u^- < P_u < P_u^+$, where $P_u^\pm(\Delta)$ stands for the bistability knees, delimiting the domain labeled "inaccessible" in Fig. 1.4(b) and (d). Below such domain, the green area corresponds to the region where temporally modulated Turing structures can be excited in uniform and modulated cavities (Fig. 1.4(b) and (d), respectively). This region has been computed numerically and corresponds to the tiny domain where Turing structures, which bifurcate subcritically, can be spontaneously formed [40]. We emphasize that this regime requires to drive the cavity with a detuning $\Delta > 4.25$, and with powers belonging to a small portion of the lower branch of the bistable response (highlighted in green over the bistable curve for $\Delta = 6.25$ in Fig. 1.4(a) and (c)). It is important to emphasize that this regime only depends on the average GVD and not on its periodic modulation. On the contrary, Faraday structures only develop when the cavity is driven over the upper branch and the periodic longitudinal variations are effective.

As a result, the stable excitation of Faraday structures requires to operate in the blue domain of Fig. 1.4(d). Note that no blue area exists in Fig. 1.4(b) which summarize the behavior of uniform cavities. In that configuration, the upper branch is modulationally stable and thus there is no pattern formation. At higher powers, such Faraday structures destabilize leading

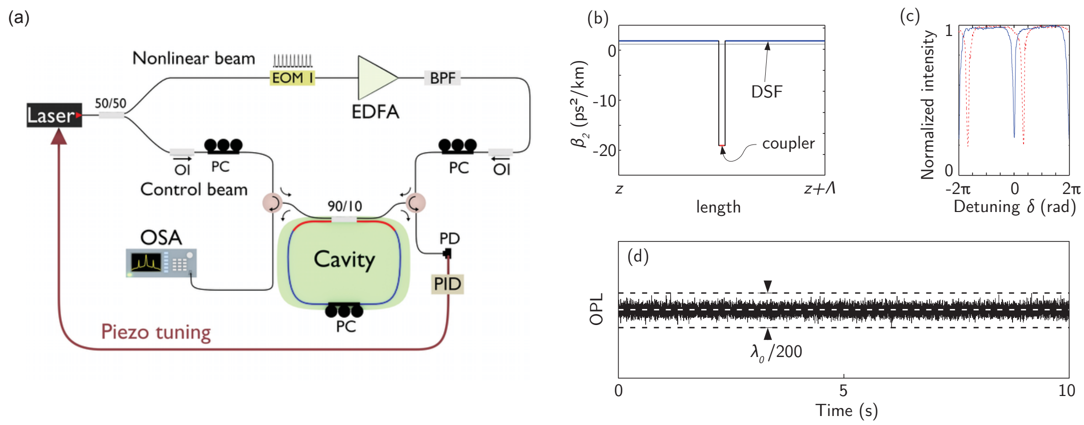

Figure 1.5 – (a) Experimental setup. (b) GVD map of the cavity over one round-trip, centered on the 90/10 SMF coupler. The gray horizontal line gives the average GVD β_2^{av} at the pump wavelength of 1550 nm. (c) Normalized transfer functions of the cavity for the Control beam (dashed red) and the Nonlinear beam in the linear regime (blue). (d) Optical path length (OPL) variation over 10 seconds when the feedback loop is operating.

to chaotic states (see upper portion of Fig. 1.4(d)). Note that the Faraday branch (unlike the Turing one) extends also to the monostable regime $\Delta < \sqrt{3}$. However, we choose to focus on the bistable regime where the two instabilities can compete thereby drastically changing the bistable switching dynamics. Indeed, at high detunings ($\Delta > 4.25$), both instability regimes can be excited in the same cavity and switching between Turing and Faraday structures can be controlled by the power (vertical axis in Fig.1.4(d)).

1.4 Experimental results

1.4.1 Steady state regime

We built a fiber ring cavity presenting the piecewise constant dispersion profile shown in Fig. 1.5(b). The ring has a total length of 51.6 m, and is composed of a 50 m long, specially designed dispersion shifted fiber (DSF, with GVD $\beta_2 = 2$ ps^2/km at 1550 nm) directly spliced to the two pigtails (total length 1.6 m) of the input/output coupler made of a standard single-mode fiber (SMF-28 with GVD $\beta_2 = -19$ ps^2/km). The average nonlinear coefficient is $\gamma = 5.5$ /W/km and we numerically checked that the slight difference (inferior to 10%) between the nonlinear coefficients does not affect the behaviour of the system. Thus, we can consider that the nonlinear coefficient is almost constant over all the cavity length. The cavity is pumped at 1550 nm (well below the average zero dispersion wavelength of 1562 nm), where the values of GVD reported above gives a normal average dispersion $\beta_2^{av} \approx 1.35$ ps^2/km. We estimated the finesse to be $\mathcal{F} = \pi/\alpha \approx 20$. The experimental setup is sketched in Fig. 1.5(a). In order to operate at constant detuning δ we use a fraction of the power of the pump called the "Control beam", launched inside the cavity in the direction opposed that of the "Nonlinear beam". We control the linear phase accumulation of light during a round-trip by finely tuning the wavelength of the laser. The output of the "Control beam" is launched into a servo controlled system (PID) to be compared to a reference level related to the desired detuning. It then generates an error signal that finely

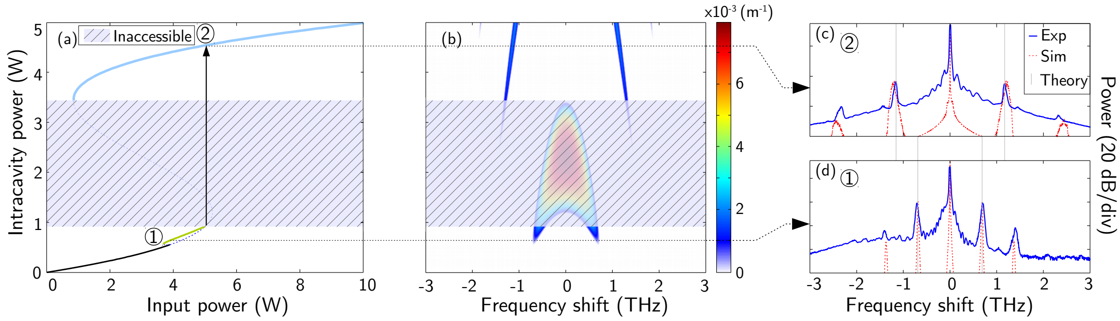

Figure 1.6 – (a) Bistable response of the cavity calculated for $\Delta = 6.25$ ($\delta = \pi/3.2$ rad, $\alpha = 0.157$); the hatched region is inaccessible. (b) Pseudo-color level plot of the gain spectrum as a function of the intracavity power calculated from Floquet analysis [25]. (c-d) Comparison of experimental spectra (solid blue), corresponding numerical integrations of the periodic LLE (1.14) (dashed red) and analytical estimates (vertical line, Theory) for two different input powers labelled 1 and 2 on the lower and upper branch respectively (see also Fig. 1.4(d)): (c) $P_{in} = 5.02$ W (4.27 W in experiment); (d) $P_{in} = 3.9$ W (3.55 W in experiment). Estimated frequencies (Theory) are from Eq. (1.23) with $m = 1$ in (c) and from Eq. (1.19) in (d).

tunes the pump wavelength to compensate for the environmental fluctuations, and thus locks the value of the detuning. The maximum duration of the locking is strongly linked to the environment fluctuations for they eventually lead to a failure of the PID system. As an example, the evolution of the optical path length of the cavity over 10 s is shown in Fig. 1.5 (d). As can be seen, the length of the cavity is stabilized with an accuracy of at least $\lambda/200$ rms.

In order to validate the general behaviour depicted in Fig. 1.4(d), we performed experiments with $\Delta = 6.25$ where both instabilities can be excited by simply tuning the pump power as predicted in Fig. 1.4 (d).

Figure 1.6 shows the results obtained for this detuning. For input powers below 3.9 W we do not observe any spectral signature of periodic structures in the output spectrum. Indeed the system is stable and simply follows the lower branch of the steady-state response shown in Fig. 1.6(a). However, when the power exceeds a first MI threshold the system enters the Turing region and exhibits the stable formation of sidebands over the lower branch. An example is shown in Fig. 1.6(d), where the primary sidebands are located at 0.70 THz. This is consistent with the fact that, while the periodic solutions corresponding to Turing structures continue to bifurcate sub-critically, a stable branch exists for a finite range of input powers, as shown by the green curve in Fig. 1.6(a). Then, when the power exceeds the value where the Turing branch merge on the stationary response, the Turing instability induces up-switching towards the upper branch. As described above, however, this branch presents narrowband Faraday instability [see Fig. 1.6(b)] and hence two sidebands are still observed in the spectra [see Fig. 1.6(b)], though at larger frequency (1.16 THz). As can be seen, experimental spectra (blue curves) in Fig. 1.6(c) and 1.6(d) are in excellent agreement with numerical simulations (dashed red curves) and with the analytical predictions of the positions for the sidebands (vertical grey lines, 0.69 THz and 1.15 THz respectively). The large difference of frequency shifts between Fig. 1.6(c) and 1.6(d) allows us to claim that we have unambiguously observed the crossover between the two instabilities. Thus, we can conclude that the dynamics of this bistable system is dramatically affected by the excitation of modulated structures due to competing Turing and Faraday branches. We showed that by tuning the pump power launched inside the cavity, one

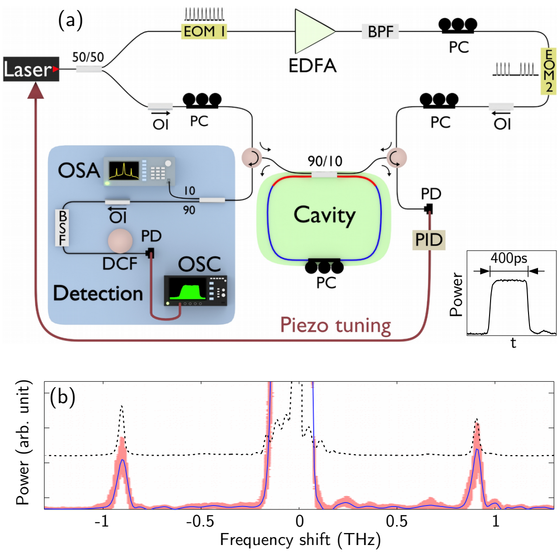

Figure 1.7 – (a) Experimental setup for the recording of both averaged (OSA) and round-trip-to-round-trip (OSC) spectra. Inset: profile of the pump pulses. (b) Spectrum recorded at the output of the cavity. A trace from a standard optical spectrum analyzer is in dashed black line, 1500 consecutive traces from the DFT technique are in red with the corresponding average spectrum superimposed in blue. The spectrum from the OSA is upshifted for the sake of clarity. EOM: electro-optic modulator; EDFA: erbium doped fiber amplifier; BPF: band-pass filter; OI: optical isolator; PC: polarization controller; PD: photo-detector; PID: proportional-integral-derivative controller; BSF: band-stop filter; DCF: dispersion compensating fiber; OSA: optical spectrum analyser; OSC: oscilloscope.

can control the dynamics of this bistable system by switching from one regime of instability to the other.

1.4.2 Transient regime

In the previous section, spectra corresponding to steady state regimes were recorded by means of an optical spectrum analyser. They are averaged over thousand of round-trips, since the typical integration time of an OSA is of the order of the second, to be compared with a round-trip time that is of the order of the microsecond. The recording of instantaneous spectra has attracted a lot of attention in recent years through the development of real time spectroscopy techniques such as the time-stretch dispersive Fourier transformation (DFT). Its ultra-short recording time enables the recording of shot-to-shot spectral fluctuations associated to ultrafast nonlinear phenomena such as MI [42], [43] or supercontinuum generation [44] or round-trip-to-round-trip dynamics of both passive and active fiber cavities [45]–[47]. We took benefit of this technique to observe the transient evolution of Turing and Faraday instabilities, in order to capture the growth and saturation of the power of the different unstable bands as well as the switching dynamics between these instabilities driven by abruptly changing the input pump power. The experimental setup shown in Fig. 1.7 is very similar to the one described in the previous section, exploited to investigate the steady state behavior of these cavities (Fig. 1.5(a)), except three details. (i) We add a second EOM (EOM 2) to create either periodic bursts of pump pulses to

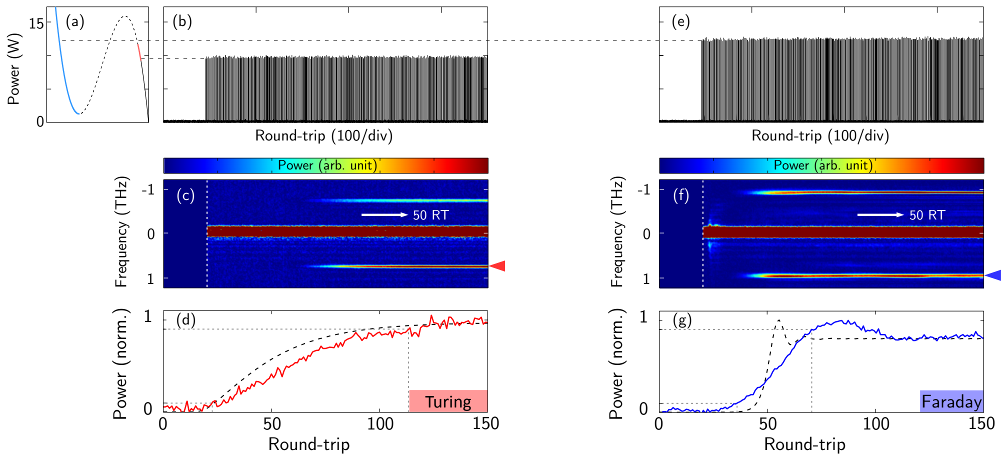

Figure 1.8 – (a) Bistable cycle. (b) Input pulse burst resulting in the excitation of Turing instabilities. (c) Experimental round-trip-to-round-trip evolution of the spectrum. The dashed line indicates the first input pulse. The Turing sideband position is marked by a red arrow on the right. (d) Evolution of the power contained in the unstable sideband indicated by the colored triangle. Numerical simulation of this transition is superimposed in dashed black line. Dashed gray lines indicate 10 and 90% of the steady power of the sidebands. (e-g) Same as (b-d) but for an input peak power of 13 W. This results in the excitation of Faraday instabilities on the upper branch of the bistable cycle.

observe the growth of Turing or Faraday instabilities or a two-level pump pattern to observe the switch from one to the other. (ii) The output spectra of the cavity are recorded by using an OSA (steady state regime) and/or a fast oscilloscope (OSC) coupled to a dispersion compensating fiber (DCF) using the real-time spectroscopy technique [48]. Note that the duration of the pulses is slightly shorter in this case (400 ps) in order to achieve an accurate frequency to time conversion via the DFT technique. (iii) The length of the cavity is slightly different (49.3 m in the present case vs. 51.6 m before).

We remind that the DFT technique basically consists in stretching the temporal pulses by a highly and purely dispersive element. Note that sufficient stretching is all the easier achieved when the pump pulses are short and this is why we used shorter pump pulses. In our setup the frequency-to-time conversion is realized by a DCF with a coefficient $\beta_2^{DCF} \times L$ of 888 ps^2. The time-to-frequency mapping is then easily obtained at first order by the relation $T(\omega) = \beta_2^{DCF} \times L \times (\omega - \omega_0)$, where ω_0 is the angular frequency of the pump. We use a fast photodiode and a 6 GHz oscilloscope for detection and we estimate the spectral resolution to be ≈ 250 pm [48]. In order to avoid saturation of the photodetector and to be able to reveal weak MI sidelobes, the pump is filtered out using a notch filter (BSF) centered at the pump wavelength. The fiber cavity (highlighted in green in Fig. 1.7(a)) still exhibits normal average dispersion. The accuracy of the frequency-to-time-to-frequency conversion has been checked by comparing the results of the DFT technique to an OSA trace. Driving the resonator with a continuous pulse train of peak power 13 W and normalized detuning $\Delta = 9$, is large enough to allow for the two regimes of instability to be independently excited as can be seen in Fig. 1.4 (d). Figure 1.7(b) shows an OSA trace along with the superposition of 1500 consecutive spectra acquired using the DFT setup and the corresponding averaged spectrum. A good agreement between the two detection methods is obtained for the range of frequency of interest which validates our setup.

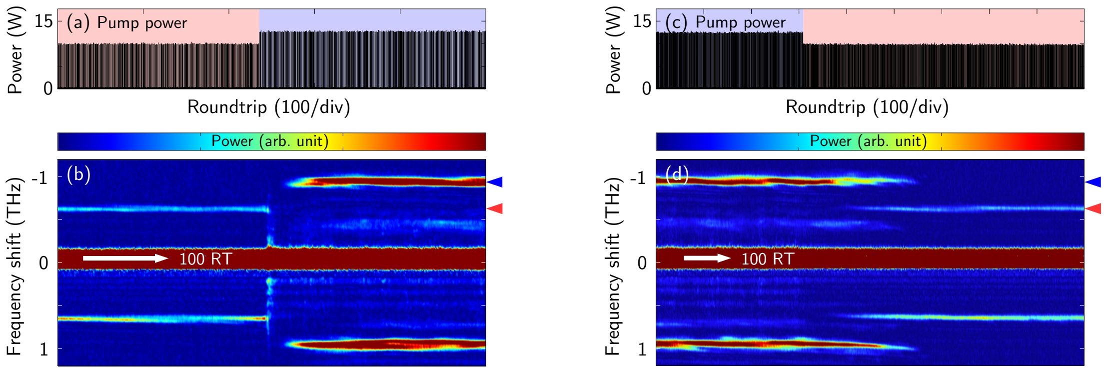

Figure 1.9 – (a) Input pulse pattern exhibiting an abrupt increase of the pump power. The two levels correspond to peak pump powers of 10 and 13 W. (b) Corresponding experimental evolution of the cavity output spectrum showing the Turing-to-Faraday transition. Turing (Faraday) sideband's position is marked by a red (blue) arrow on the right. (c-d) Same as (a-b) but for a sudden decrease of the input power, thus triggering the Faraday-to-Turing transition.

We then proceeded to investigate the onset of the Turing and Faraday sideband growth by launching a burst of pump pulses with constant power. Working at fixed detuning, the nature of the instability observed only depends on the peak power of the pump pulses: in our setting, 10 W for the Turing branch (Fig. 1.8(b)) and 13 W for the Faraday branch (Fig. 1.8(e)). Figure 1.8(c) and (f) show that in both cases a pair of spectral sidebands appear symetrically to the pump after a few round-trips, at a frequency shift slightly higher for Faraday sidebands, which is in agreement with theory and previous experiments [25], [30]. Furthermore this allows us to unambiguously identify the observed regime of instability, as shown in the previous section. The growth of the power of the unstable modes eventually saturates as the system reaches a stable attractor of the dynamics [37]. This is clearly illustrated by Fig. 1.8(d) and (g), which showcase the temporal evolution of the power content of the high-frequency sideband in the two regimes. By comparing Fig. 1.8(d) and (g), one clearly notices that the transition to the stable Turing regime appears to be slower than the transition to the Faraday regime. A simple and intuitive explanation lies on the difference of parametric gain between the two regimes of instability. Indeed, we verified that the parametric gain is more than two times higher in the Faraday case compared to the Turing case. On the other hand, the rise time of the Faraday mode is nearly two times shorter than the one of the Turing mode. This supports the argument that the difference in the dynamics between these two regimes is essentially driven by the strength of the parametric gain. In order to compare with the experimental recordings, we also conducted numerical simulations based on the LLE (1.13) seeded at the unstable frequency. The outcome is displayed as dashed black lines in Fig. 1.8(d) and (g). A good qualitative agreement is obtained, clearly highlighting the faster transition in the case of the Faraday instability.

Besides the emergence of the Faraday unstable branch in addition to the Turing one, the inhomogeneous dispersion profile allows the transition between these instability regimes by simply tuning the input power while keeping the detuning fixed. This power dependence has been observed in the stationary regime through the abrupt change of unstable frequency associated to the two instabilities [30]. Here we analyze the transition between those instabilities by recording the real-time evolution of the cavity output spectrum when abruptly tuning the input pump power from a level corresponding to the Turing regime to a higher one which corresponds to the Faraday regime and vice versa.

Figure 1.9(b) shows the evolution of the output spectrum corresponding to the pump power evolution of Fig. 1.9(a). The abrupt power step is preceded by a large number of pump pulses of 10 W peak power (not shown here) to ensure that a stable Turing state is reached. Once again, the different regimes of instability can be identified owing to their different characteristic frequencies. The sudden increase of pump power appears to trigger the Turing-to-Faraday transition i. e. the switching of the system from the lower branch to the upper branch of the bistable cycle. The opposite transition can occur when we switch back the input power to its lower value. This is illustrated in Figs. 1.9(c-d) which show that, after such modification of the driving field, the system goes back to a stationary state on the lower branch of the bistable cycle in the region of Turing instability. To summarize, we showed that the dynamics of dispersion oscillating cavities can be experimentally investigated in details by means of a standard DFT technique, which allows the round-to-round-trip recording of output spectra. It revealed that by simply tuning the pump power one can trigger Turing and Faraday instabilities.

1.5 Conclusions

We investigated theoretically and experimentally the development of different kinds of instabilities in passive ring cavities composed of pieces of fiber with different dispersion. We presented an original derivation of the well known Lugiato-Lefever equation adapted for the description of dispersion oscillating cavity. Quite remarkably, we demonstrated that this equation is valid well beyond the mean field approximation, under which it has been traditionally derived. We reviewed the theory of Turing (modulational) and Faraday (parametric) instability in inhomogeneous fiber cavities by means of Floquet theory. We reported the experimental demonstration of the generation of stable Turing and Faraday patterns in the same device, which can be controlled by changing the detuning and/or input power. Moreover, we experimentally recorded the round-trip-to-round-trip dynamics of the spectrum by implementing a real-time spectroscopy technique. We found that Turing and Faraday instabilities not only differ by their characteristic frequency but also by their dynamical behavior. In more general terms, we showed that compared to other experimental setups, fiber ring cavities made of dispersion oscillating fibers are a fantastic test bed for fundamental investigations since the dynamics can easily be recorded by means of simple DFT techniques and the dispersion step easily tuned with different optical fibers. It paves the way to more complete experimental and fundamental investigations of parametric instabilities in passive resonators, namely of their nonlinear regimes. These fundamental investigations can also find direct applications in the context of soliton or frequency comb generation in microresonators.

1.5.1 Personal contribution and scientific production

I opened this new line of research soon after my arrival at PhLAM. In fact, it seemed natural to me to extend the investigations on dispersion oscillating fibers which were carried on at PhLAM to the case of a fiber ring resonator. I predicted theoretically MI in DOF cavities, which has been the central result for all the subsequent investigations. I then furnished a theoretical support to the experiments, I performed or supervised the simulations, and contributed to the design and analysis of the experimental results. The overall outcomes of these activities are:

- 6 peer-reviewed papers (1 *Physical Review Letters*) [J7,J8,J9,J15,J17,J39]
- 4 international conferences [C3,C8,C4]

CHAPTER 2

Nonlinear stage of modulation instability in dispersion oscillating fibers

In this Chapter we study modulation instability in fibers with a periodic variation of the group velocity dispersion, or dispersion oscillating fibers (DOF). We show that the nonlinear stage of modulational instability induced by the periodic dispersion in the average *normal* dispersion regime, can be accurately described by combining mode truncation and averaging methods. The resulting integrable oscillator reveals a complex hidden heteroclinic structure of the instability. A remarkable consequence, validated by the numerical integration of the nonlinear Schrödinger equation, is the existence of breather solutions separating different Fermi-Pasta-Ulam recurrent regimes. Our theory also shows that optimal parametric amplification unexpectedly occurs outside the bandwidth of the resonance (or Arnold tongues) arising from the linearised Floquet analysis.

2.1 Introduction

Following the pioneering studies by Faraday and Lord Rayleigh [29], [49], the universal nature of parametric resonances (PRs) induced by periodic variations of a system parameter [28] was established in several contexts, involving micro- [50] and nano-oscillators [51], optical trapping [52], wrinkling [53], quantum tunnelling [54], and Faraday waves [55], [56]. The concept of PR originates in the linear world: the undamped harmonic oscillator with natural frequency ω_0 exhibits PRs at driving frequencies $\omega_p = 2\omega_0/p$ (p integer) according to the Mathieu equation. However, PRs deeply impact also the behavior of *nonlinear* conservative systems. The full nonlinear dynamics of PRs is relatively well understood only for low-dimensional Hamiltonian systems [28]. Conversely, the analysis of *extended* systems described by partial differential equations with periodicity *in the evolution variable* is essentially limited to determine the region of parametric instability (Arnold tongues) via Floquet analysis [57]–[59], while the nonlinear stage of PR past the linearized growth of the unstable modes remains mostly unexplored.
In this Chapter, taking the periodic defocusing nonlinear Schrödinger equation as a widespread example ranging from e.g. atom condensates to optics [21], [24], [60], we show that the PR gives rise to quasi-periodic evolutions which exhibit on average Fermi-Pasta-Ulam (FPU) recurrence

[2], [3] with a remarkably complex (but ordered) underlying phase-plane structure. Such structure describes the continuation into the nonlinear regime of the modulation instability of a background solution, uniquely due to the parametric forcing. A byproduct of this structure is the existence of breather-like solutions [61], that suggests the intriguing possibility of observing rogue waves in the defocusing scalar NLSE. On the other hand, the richness of such structure allows us to predict that optimal parametric amplification occurs at a critical frequency where the system lies off-resonance (outside the PR bandwidth). These features are discovered by proper averaging over the fast-scale oscillations. Our approach retains its validity in the regime of strong parametric driving, where the system is found to exhibit a remarkably ordered structure despite its broken translational symmetry and integrability.

2.2 Parametric resonances in the NLSE with peridic dispersion

We consider the following periodic NLSE:

$$i\frac{\partial\psi}{\partial z} - \frac{\beta(z)}{2}\frac{\partial^2\psi}{\partial t^2} + |\psi|^2\psi = 0, \tag{2.1}$$

referring to the notation used in optical fibers in suitable scaled units. The dispersion is $\beta(z) = \beta_{av} + \beta_m f_\Lambda(z)$, with positive average $\beta_{av} > 0$; $f_\Lambda(z)$ has period $\Lambda = 2\pi/k_g$, zero mean and minimum -1. The method can be easily extended to deal also with periodic nonlinearities. We are interested in the nonlinear evolution of perturbations of the stationary solution $\psi_0 = \sqrt{P}\exp(iPz)$ with power $P = |\psi_0|^2$. The field ψ can be rescaled to give $P = 1$. Although we set $P = 1$ in the figures, we leave P as a parameter in the equations in order to highlight the role of nonlinear terms. First, we briefly recall the origin of PRs in this system [24], [57], [58]. Modulational instability of the stationary solution ψ_0 can be analyzed by inserting in Eq. (2.1) the ansatz:

$$\psi = \psi_0 + a(z,t), \tag{2.2}$$

a being a perturbation at frequency ω of the form:

$$a = [\epsilon_1(z)\exp(i\omega t) + \epsilon_2^*(z)\exp(-i\omega t)]\exp(iPz). \tag{2.3}$$

Linearizing around $\mathbf{x}(z) = [\epsilon_1(z),\ \epsilon_2(z)]^T$ gives a Λ-periodic problem of the form $d\mathbf{x}/dz = A\mathbf{x}$, with $A(z) = A(z+\Lambda)$, which can be treated by means of Floquet theory. In the absence of perturbation ($\beta_m = 0$), $\mathbf{x}(z)$ exhibits only phase changes ruled by imaginary eigenvalues $\pm ik$, where $k^2 = \beta_{av}\omega^2/2\left(\beta_{av}\omega^2/2 + 2P\right)$ represents the squared spatial frequency of the evolution. As a result ψ_0 is stable. Any arbitrarily small perturbation $\beta_m \neq 0$ induces, regardless of its shape $f_\Lambda(z)$, instability at multiple frequencies ($p = 1, 2, \ldots$):

$$\omega_p = \sqrt{\frac{2}{\beta_{av}}\left(\sqrt{P^2 + \left(\frac{p\pi}{\Lambda}\right)^2} - P\right)}, \tag{2.4}$$

which fulfil the PR condition $k_g = 2k(\omega_p)/p$, analogous to Mathieu equation [28]. The Floquet analysis gives rise to instability islands, or Arnold tongues, in the plane (ω, β_m), with ω_p representing the tip of the tongues, as shown in Fig. 2.1(a), taking as an example $f_\Lambda(z) = \cos(k_g z)$ and $p = 1, 2$. Figure 2.1(b) shows the instability gain spectrum $g_F(\omega)$ at $\beta_m = 0.5$, which accurately predicts the spontaneous growth of MI bands from white noise, obtained from NLSE integration, shown in the inset of Fig. 2.1(b).

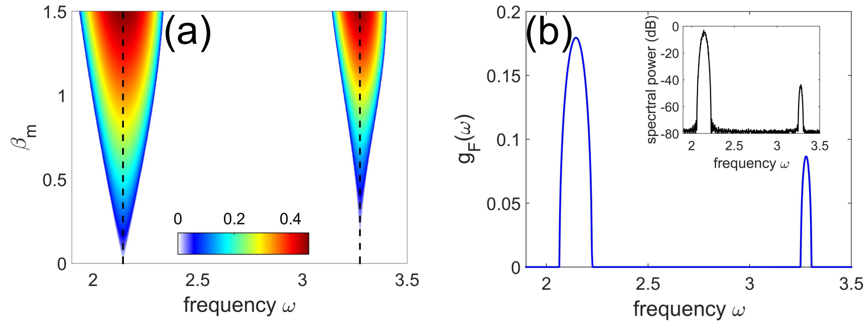

Figure 2.1 – Results of the linear Floquet analysis for $f_\Lambda(z) = \cos(k_g z)$, $\Lambda = 1$, $P = 1$: (a) false color plot showing first two MI tongues in the plane (ω, β_m) [dashed vertical lines stand for ω_p, $p = 1, 2$, from Eq. (2.4)]; (b) section at $\beta_m = 0.5$ showing gain curves $g_F(\omega)$; Inset: spectral output ($z = 50$) from numerical integration of NLSE (2.1), where PRs grow out of white noise superimposed onto ψ_0.

Two aspects of the PR instability are of crucial importance: (i) it exhibits narrowband features around the tongue tip frequencies ω_p; (ii) different ω_p are generally incommensurate, which greatly reduces the possibility that the harmonics of a probed frequency experience exponential amplification due to higher-order bands. These properties allow us to simplify the analysis of the nonlinear development of parametric instability, by considering the evolution of a few discrete modes, as described in the next section.

2.3 Three-wave truncation and averaging

Under the circumstances (i) and (ii) introduced before, three-mode truncation constitutes a suitable approach to describe the underlying structure of the dynamics [62]. However, unlike uniform media where the truncation is integrable, in the PR such structure can remain hidden owing to the fast phase variations induced by the oscillating dispersion, which breaks the integrability of the truncated model too. In order to unveil the dynamics, we need to combine the mode truncation approach with suitable phase transformations and averaging [63]. We start by substituting in Eq. (2.1) the following field:

$$\psi = A_0(z) + a_1(z)\exp(-i\omega t) + a_{-1}(z)\exp(i\omega t), \tag{2.5}$$

and group all nonlinear terms vibrating at frequencies $0, \pm\omega$, neglecting higher-order harmonic generation. For sake of simplicity we consider henceforth the case of symmetric sidebands $a_1 = a_{-1} \equiv A_1/\sqrt{2}$, though our analysis and conclusions straightforwardly extend to the case $a_1 \neq a_{-1}$. We obtain the following non-autonomous Hamiltonian system of ordinary differential equations (dot stands for d/dz):

$$-i\dot{A}_0 = (|A_0|^2 + 2|A_1|^2)A_0 + A_1^2 A_0^*, \tag{2.6}$$

$$-i\dot{A}_1 = \left[\frac{\beta(z)\omega^2}{2} + \left(\frac{3|A_1|^2}{2} + 2|A_0|^2\right)\right]A_1 + A_0^2 A_1^*, \tag{2.7}$$

where the only conserved quantity $P = |A_0|^2 + |A_1|^2$ is not sufficient to guarantee integrability. In order to describe the mode mixing in the p-th unstable PR band beyond the linearized stage, we transform to new phase-shifted variables $u(z), w(z)$, defined as:

$$A_0(z) = u(z), \;\; A_1(z) = w(z) e^{i\left(p\frac{k_g}{2}z + \frac{\delta k(z)}{2}\right)}, \tag{2.8}$$

where $\delta k(z) = \beta_m \omega^2 \int_0^z f_\Lambda(z')dz'$ physically accounts for the oscillating wavenumber mismatch of the three-wave interaction. Then, we exploit the general Fourier expansion:

$$\exp[i\delta k(z)] = \sum_n c_n \exp(-ink_g z), \tag{2.9}$$

which allows us to cast Eqs. (2.6-2.7) in the form:

$$-i\dot{u} = (P + |w|^2)u + \left[c_p + F_\Lambda(z)\right] w^2 u^*, \tag{2.10}$$

$$-i\dot{w} = \left(\frac{\kappa}{2} + \frac{|w|^2}{2} + |u|^2\right) w + \left[c_p^* + F_\Lambda^*(z)\right] u^2 w^*, \tag{2.11}$$

where $F_\Lambda(z) \equiv \sum_{n\neq p} c_n \exp[-i(n-p)k_g z]$, and $\kappa \equiv \beta_{av}\omega^2 - pk_g + 2P$ measures the mismatch from optimal linearized amplification. Indeed $\kappa = 0$ is equivalent to the quasi-phase-matching condition $\beta_{av}\omega^2 + 2P = pk_g$, where the quasi-momentum pk_g associated to the forcing compensates for the average nonlinear wavenumber mismatch of the three-wave interaction.

In the quasi-matched regime ($|\kappa| \ll 1$), the dominant mixing terms $c_p w^2 u^*$ and $c_p^* u^2 w^*$ in Eqs. (2.10-2.11) are responsible for the growth of sidebands associated with the PR instability in the p-th band. However, additional contributions to the mixing arise from the mismatched terms contained in the Λ-periodic function $F_\Lambda(z)$. In order to evaluate their impact we generalize the approach of Ref. [63]. We assume $1/k_g$ to be small and expand u, w in Fourier series:

$$u(z) = \sum_n u_n(z) e^{inpk_g z}, \;\; w(z) = \sum_n w_n(z) e^{inpk_g z}. \tag{2.12}$$

Assuming that w_n, u_n vary slowly with respect to $\exp(ik_g z)$, and the harmonics to be of order $1/k_g$ (or smaller, compared to leading order or spatial average u_0, w_0), we are able to express w_n, u_n through the relations:

$$u_n = \frac{1}{pk_g}\frac{c_{p(1-n)}}{n} w_0^2 u_0^*, \;\; w_n = \frac{1}{pk_g}\frac{c^*_{p(1+n)}}{n} u_0^2 w_0^*. \tag{2.13}$$

Equations (2.13) allow us to obtain the average self-consistent equations for the leading functions $u_0(z), w_0(z)$:

$$-i\dot{u}_0 = (P + |w_0|^2)u_0 + c_p w_0^2 u_0^* + \alpha\left(|w_0|^4 - 2|w_0 u_0|^2\right) u_0, \tag{2.14}$$

$$-i\dot{w}_0 = \left(\frac{\kappa}{2} + \frac{|w_0|^2}{2} + |u_0|^2\right) w_0 + c_p^* u_0^2 w_0^* - \alpha\left(|u_0|^4 - 2|w_0 u_0|^2\right) w_0, \tag{2.15}$$

which shows that the mismatched terms result into an effective quintic correction weighted by the (small) coefficient $\alpha = \frac{1}{pk_g}\sum_{n\neq 0}\frac{|c_{p(1-n)}|^2}{n}$.

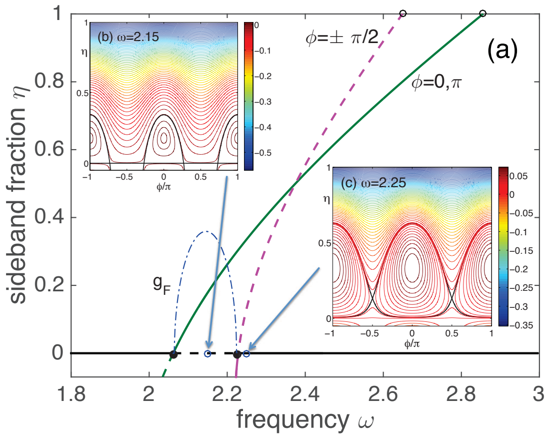

Figure 2.2 – (a) Bifurcation diagram from Eqs. (2.16): sideband fraction η of unstable (dashed red) and stable (solid green) branches vs. ω. The instability range of the pump mode $\eta = 0$ coincides with the bandwidth calculated from Floquet analysis (gain g_F, dot-dashed line). Insets (b,c): phase-plane pictures for (b) $\omega = 2.15$ inside PR gain bandwidth; (c) $\omega = 2.25$, outside PR gain bandwidth, where the topology is affected by saddle eigenmodulations with $\eta \neq 0$. Here $p = 1$ (primary PR), $\beta_m = 0.5$, $\Lambda = 1$, $P = 1$.

Equations (2.14-2.15) can be cast in the following Hamiltonian form:

$$\begin{aligned} \dot{\eta} &= -\frac{\partial H_p}{\partial \phi}; \ \dot{\phi} = \frac{\partial H_p}{\partial \eta}, \\ H_p &= |c_p|\eta(1-\eta)\cos 2\phi + \frac{\kappa}{2}\eta - \frac{3}{4}\eta^2 - \alpha\eta\left(1 - 3\eta + 2\eta^2\right), \end{aligned} \tag{2.16}$$

in terms of fractional sideband power $\eta = |w_0|^2 \approx |A_1|^2$ and overall phase $\phi = Arg[w_0(z)] - Arg[u_0(z)] + \phi_p/2$, $\phi_p = Arg[c_p]$.

We have thus obtained an integrable Hamiltonian system, which describes the development of the parametric unstable sidebands beyond the initial linear stage. In the next section we show that this Hamiltonian structure has deep impact on the dynamical behavior of the system.

2.4 Heteroclinic structure: Breathers and FPU recurrence

Equations (2.16) constitute an averaged integrable description of the fully nonlinear stage of the instability, which holds valid regardless of the choice of order p and the specific function $f_\Lambda(z)$. Among the different tests that we have performed, in the following we present the results obtained for the harmonic case $f_\Lambda(z) = \cos(k_g z)$ already considered in Fig. 2.1. In this case, the Fourier expansion can be calculated explicitly:

$$\exp[i\delta k(z)] = \sum_{n=-\infty}^{\infty} (-1)^n J_n\left(\frac{\beta_m \omega^2}{k_g}\right)\exp(-ink_g z), \tag{2.17}$$

which gives for the primary parametric resonance ($p = 1$):

$$c_0(\omega) = J_0\left(\frac{\beta_m \omega^2}{k_g}\right), \tag{2.18}$$

$$c_1(\omega) = -J_1\left(\frac{\beta_m \omega^2}{k_g}\right), \tag{2.19}$$

$$\alpha(\omega) \approx \frac{1}{k_g}\left(|c_0|^2 + |c_1|^2/2\right), \tag{2.20}$$

where we have considered $c_0 \gg c_n, n > 1$ in order to simplify the expression of α.
Explicit solutions of Eqs. (2.16) can be written in terms of hyperelliptic functions. However, their phase-plane representation (level set of H_p) along with the bifurcation analysis are sufficient to gain a full physical insight. Figure 2.2 shows the bifurcation diagram, i.e. the value η of the stationary points (solutions of $\dot\eta = \dot\phi = 0$) versus frequency ω. The instability of the pump mode $\eta = 0$ reflects the PR instability of order p. Indeed the points:

$$\eta = 0, \;\; \phi^{\pm} = \pm\frac{1}{2}\cos^{-1}[(\alpha - \kappa/2)/|c_p|],$$

turn out to be saddle points of the Hamiltonian H_p in the range of frequencies implicitly determined by the condition:

$$-|c_p(\omega)| \le \alpha(\omega) - \kappa(\omega)/2 \le |c_p(\omega)|,$$

which agree with the PR bandwidth from linear Floquet analysis [see the comparison in Fig. 2.2 for $p = 1$]. Within such range of frequencies, the accessible portion of the phase plane ($\eta \ge 0$) is characterized by a heteroclinic separatrix which connects such saddles, dividing the phase plane into regions of inner and outer orbits which are similar to those describing librations and rotations of a standard pendulum, respectively [see Fig. 2.2(b)]. At the edges of such frequency span, the pump mode bifurcates and new phase-locked eigenmodulation branches appear with modulation depth $\eta = \eta_s \neq 0$ variable with frequency, and phase locked either to $\phi = 0, \pi$ (stable, centers) or $\phi = \pm\pi/2$ (unstable, saddles). New heteroclinic connections emanate from the latter, dividing the accessible phase plane into three different domains [see Fig. 2.2(c)].

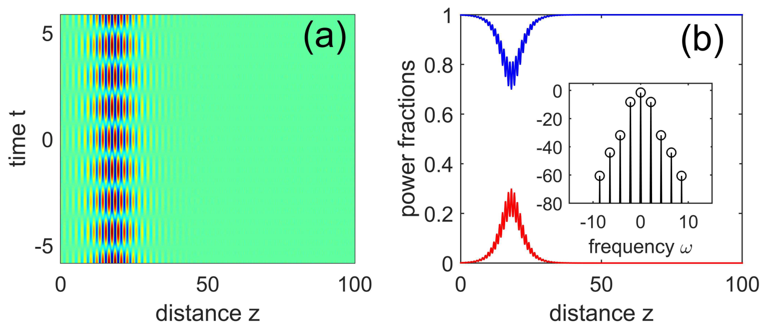

Figure 2.3 – PR breather excitation from numerical integration of NLSE (2.1): (a) color level plot of $|\psi|^2$; (b) fractions $|A_0|^2$, $|A_1|^2$ of Fourier modes vs. z. Inset: log scale spectrum at the point of maximum depletion, $z = 18$. Here $\beta_m = 0.5$, $\omega = 2.15$, $\Lambda = 1$, $P = 1$, and initial condition $\eta_0 = 0.001$, $\phi_0 = 0.24162\pi$ corresponds to the separatrix in Fig. 2(b).

The structure illustrated in Fig. 2.2 has deep implications for the long-term evolution of the PR in the full NLSE (2.1). In order to show this we numerically integrate Eq. (2.1) with initial value representing a weakly modulated background: $\psi_0(t) = \sqrt{1-\eta_0} + \sqrt{2\eta_0}\exp(i\theta_0)\cos(\omega t)$, $\eta_0 \ll 1$, where θ_0 is linked to the overall initial phase $\phi_0 = \phi(0)$ as $\phi_0 = \theta_0 + \phi_p/2$.

Considering first frequencies within a PR band, we show in Fig. 2.3 the excitation of the infinite-dimensional analog of the heteroclinic separatrix shown in the left inset in Fig. 2.2, obtained from a very weak modulation ($\eta_0 = 0.001$) with suitable phase. This entails a single cycle of amplification connecting the background to itself with opposite phases, i.e. the analog of the well known Akhmediev breather of the integrable *focusing* NLSE [61]. This type of solutions of the periodic NLSE (2.1), which we term as parametric resonance breathers (PR breathers), are characterized by a main breathing occurring on top of the short Λ-scale breathing. PR breathers can be excited for all frequencies inside the PR bandwith. We remark that although they entail the generation of harmonics of the input modulation, the spectrum decays rapidly as shown in the inset of Fig. 2.3(b) and the dynamics is dictated by the first sideband pair with the harmonics that remain locked to them.

A PR breather divides the phase-plane into two types of dynamical behaviors which exhibit different FPU-like recurrence, i.e. cyclic amplification and de-amplification of the modulation over scales much longer than the Λ−scale of small oscillations. One of such recurrent regimes is displayed in Fig. 2.4(a,b), obtained for $\eta_0 = 0.02$, $\phi_0 = 0$. When we flip the initial phase to $\phi_0 = \pi/2$ we observe a very similar behavior. However the projection of the NLSE evolutions onto the phase-space (η, ϕ) reveals very different behaviors for the two initial phases. While

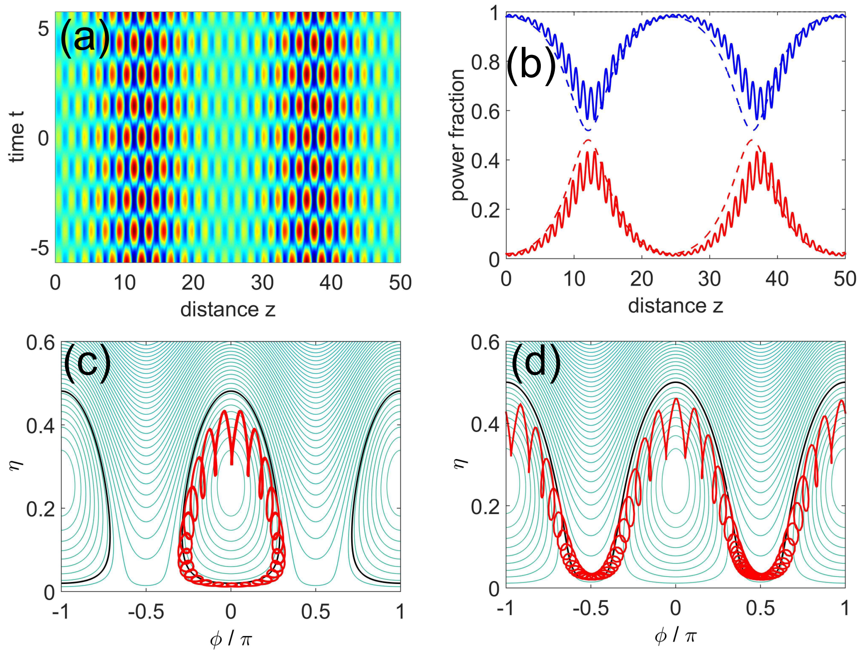

Figure 2.4 – Quasi-periodic recurrent evolution from full NLSE numerical integration with $\eta_0 = 0.02$: (a) colormap of $|\psi|^2$; (b) evolution of extracted pump and sideband power fractions for $\phi_0 = 0$ (solid lines), compared with those from the average model (dashed lines), Eq. (2.16). (c-d) projections of the NLSE numerical evolutions over the phase plane of the averaged system for $\phi_0 = 0$ (c) and $\phi_0 = \pi/2$ (d). Here $\beta_m = 0.5$, $\omega = 2.2$, $\Lambda = 1$, $P = 1$.

in both cases we observe quasi-periodic evolutions, in one case ($\phi_0 = 0$) the recurrence occurs around the libration-type of orbit of the averaged system [Fig. 2.4(c)], whereas the recurrent dynamics for $\phi_0 = \pi/2$ follows rotation-type of dynamics with the phase spanning continuously the full range $(-\pi, \pi)$ [Fig. 2.4(d)]. This is the clear signature of the hidden heteroclinic structure of the PR in the periodic NLSE. At variance with the well-known structure of the integrable focusing NLSE, it cannot be revealed directly from the space-time evolutions [Fig. 2.4(a)], due to the fast scale oscillations associated with the driving.

2.5 Amplification outside the linear gain band

The geometric structure of the nonlinear PR has even more striking consequence in terms of optimal parametric amplification of small sideband pairs. Clearly, the Floquet analysis entails that the sidebands growth rate is maximum at frequencies where the gain g_F peaks. However, the nonlinear analysis shows that stronger conversion occurs towards higher frequencies of the gain curve, despite a slower initial growth. Indeed the long range conversion is associated with quasi-periodic evolutions in the neighbourhood of the averaged separatrix, and the latter extends to larger portion of the phase space and hence larger values of η as the frequency increases. The remarkable and unexpected fact, however, is that strong nonlinear conversion occurs also at frequencies higher than the high-frequency edge of the PR bandwidth. While at such frequency the background is stable, strong nonlinear conversion is permitted nearby the heteroclinic orbit that emanates from the unstable eigenmodulations. As a result, the converted sideband fraction as a function of ω exhibits a maximum slightly below a critical frequency ω_c which lies off-resonance, i.e. outside the Floquet gain bandwidth of PR, as shown in Fig. 2.5(a). Across ω_c the conversion abruptly drops, as entailed by qualitatively different conversion regimes [Fig. 2.5(b,c)] and remain low for $\omega > \omega_c$. The critical frequency corresponds to the evolution along the heteroclinic orbit in Fig. 2.2(c) and can be calculated as the implicit solution

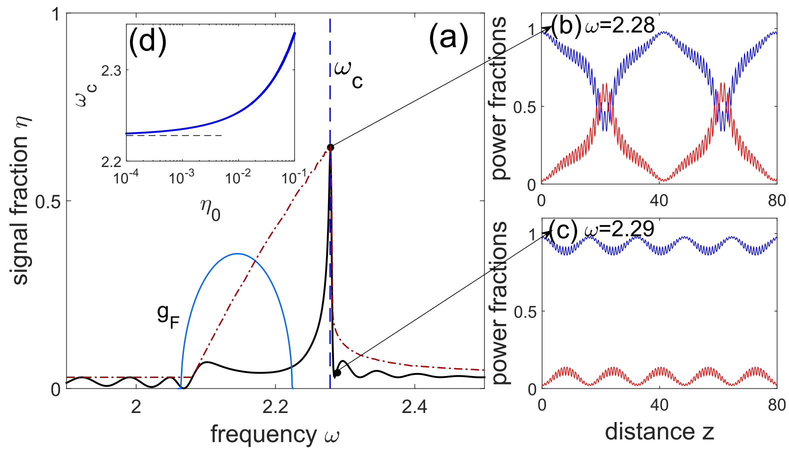

Figure 2.5 – (a) Output sideband fraction $\eta(z = 20)$ vs. ω from NLSE numerical integration for $\eta_0 = 0.03$ and $\phi_0 = 0$ (solid black curve; dash-dotted brown curve gives the maximum achievable conversion along z), with superimposed small-signal PR gain $g_F(\omega)$ (solid cyan curve). (b-c) Pump and sideband mode evolutions extracted from NLSE numerical integration across ω_c [vertical dashed line in (a), obtained from Eqs. (2.16)]. Inset (d): ω_c vs. input modulation fraction η_0 (the horizontal dashed line stands for the edge frequency of $g_F(\omega)$).

of the equation $H_p(\eta_s(\omega), \phi = \pm\pi/2) = H_p(\eta_0, \phi_0)$. ω_c tends to the high-frequency edge of the Floquet bandwidth in the limit of vanishing input signal $\eta_0 \to 0$, and substantially deviates from it when increasing η_0, even moderately, e.g. up to 10%, as shown in Fig. 2.5(d).

2.6 Experiments in dispersion oscillating fibers

The physics described above could be observed in realizable dispersion oscillating optical fibers. In fact, the generation of new spectral components corresponding to the parametric unstable frequencies, has already been reported [21]. This shows the potentiality of this physical set-up, making it a good candidate to be a tool for the exploration of the nonlinear regime of parametric instability that we have studied so far. In this case the dimensional form of the NLSE is:

$$i\frac{\partial A}{\partial Z} - \frac{\beta_2(Z)}{2}\frac{\partial^2 A}{\partial T^2} + \gamma|A|^2 A = 0, \tag{2.21}$$

where A is the electric field envelope, normalized in such a way $|A|^2$ is measured in Watts, $\beta_2(Z) = \overline{\beta}_2 + \beta_2^A \cos(KgZ)$ is the group velocity dispersion, a sinusoidal function of period $Z_0 = 2\pi/K_g$, γ is the nonlinear coefficient and Z, T are the real-world distance and time. The fibers described in [21] have lengths of a few hundreds of meters and a typical period of a few meters. Typical values of the group velocity dispersion and nonlinearity are $\overline{\beta}_2 = 1.5 \times 10^{-27}$ s^2/m, $\beta_2^A = 1.5 \times 10^{-27}$ s^2/m, $\gamma = 7W^{-1}Km^{-1}$. A continuous wave laser source at 1 micron with a peak power of a few Watts has been exploited to generate the stationary background field. The parametric resonance frequencies has a frequency detuning from the pump of a few THz.
It will be possible to observe the off-resonance gain (see Fig.2.5), by exploiting two tunable cw lasers, one for the pump and a second one (weak seed) for the sideband. We performed some numerical simulations by using realistic parameters. An example is reported in Fig. 2.6, which compares qualitatively well with Fig. 2.5. An optimization of the fiber design will be necessary to access the nonlinear stage of parametric instability in the DOF, which was never been explored so far.

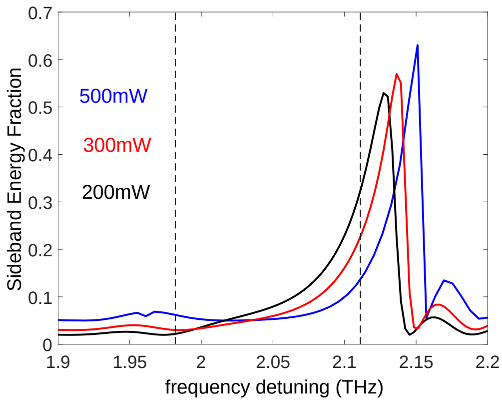

Figure 2.6 – Output sideband fraction from numerical integration of dimensional NLSE (2.21) as a function of sideband frequency detuning for three different input sideband powers. Fiber length 150m, period $Z_0 = 7.5$ m, $\overline{\beta}_2 = 4 \times 10^{-27}$ s^2/m, $\beta_2^A = 2.2 \times 10^{-27}$ s^2/m nonlinearity, $\gamma = 7.5W^{-1}Km^{-1}$, pump power 10W.

2.7 Conclusions

We have studied the nonlinear development of modulational instability arising in fiber with a periodic modulation of group velocity dispesion in the average normal dispersion regime. The physics is described by a parametrically dirven defocusing NLSE. By means of a three-wave reduction and a proper averaging over fast oscillations, we have unveiled the underlying phase-space structure. This allowed us to reveal the existence of a parametric resonance breather solution dividing different regimes of Fermi-Pasta-Ulam recurrence. From a more application oriented point of view, we have show that optimal parametric amplification is not *a priori* predicted by the linear stability analysis, and cases exist where the maximum gain is obtained outside the resonance band. Preliminary numerical simulations with realistic fibers suggest that the phenomena can be readily observed in experiments.

2.7.1 Personal contribution and scientific production

My main role in this area has been to establish and to manage the collaboration between the mathematicians of the Laboratoire Painlevé and the experimenters of PhLAM in the framework of the LABEX CEMPI. Thanks to my interdisciplinary formation, I helped the two communities to establish a common "language", which permitted fruitful exchanges. The cooperation eventually lead to unveil complex nonlinear processes in dispersion oscillating fibers and to perform the corresponding experiments. The overall outcomes of these activities are:

- 2 peer-reviewed papers (1 *Physical Review Letters*) [J10,J21]
- 2 invited international conferences [I5,I7]
- 3 international conferences [C4,C7,C13]

CHAPTER 3

Dispersive shocks in optical fibers

Dispersive shock waves are strongly oscillating wave trains that spontaneously form and expand thanks to the action of weak dispersion, which contrasts the tendency, driven by the nonlinearity, to develop a gradient catastrophe. In this Chapter we review the basic concepts and our recent progresses made in the description of such nonlinear waves, both in terms of experimental results and modelling. After a brief introduction on the generating mechanisms of dispersive shocks in optical fibers, we report the experimental observation of the rupture of a photonic dam, as well as the theory and some experiments on the generation of resonant radiation from shocks in fibers and resonators.

3.1 Introduction

Dispersive shock waves (DSWs) are non-stationary wave trains that develop spontaneously in weakly dispersive nonlinear media [64]. The nonlinearity induces front steepening and hence the tendency to develop a gradient catastrophe. A weak dispersion plays a secondary role until steep gradients are eventually formed. At this stage dispersion becomes effective, inducing the onset of strong oscillations which expand in a characteristic fan in the space-time plane. The borders of this fan represent the leading and the trailing edge of the DSW, where the amplitude of the oscillations are largest and vanishingly small, respectively. DSWs constitute the dispersive counterpart of viscous regularization of classical shock waves [65], which occurs when the dissipation dominates over the dispersive effects.
The investigation of DSWs has a long history that starts with pioneering contributions in the 60's and the 70's, when DSWs were mainly known as *collisionless shocks*. Indeed Sagdeev and coworkers first predicted the oscillatory nature of the shock occurring in the extremely rarefied (collisionless) plasma [66]. The observation of such dispersive breaking in the lab was reported as early as 1970 [67]. From the theory point of view, the weakly dispersive Korteweg-de Vries (KdV) equation played a pivotal role in the early developments. In 1965 Zabuski and Kruskal [68] investigated soliton-like excitations emerging from the dispersive breaking of a sinusoidal wave. This can be thought of as the periodic analog of smooth waveforms containing a large number of solitons, which start to emerge after a wavebreaking defined in the dispersionless

limit. However, more generally DSWs do not require soliton content to develop. A milestone towards a more general description was the solution of the Riemann problem (the evolution of a step initial datum) for the KdV, reported by Gurevich and Pitaeviskii [69], who proposed the first explicit construction of a DSW by exploiting Whitham modulation theory [70]. The modulation approach was soon extended to the defocusing nonlinear Schrödinger equation [71], [72] and then deepened during several decades, remaining a powerful technique to describe the long-time asymptotic of the DSW past the breaking point developing in the dispersionless limit. The picture that has globally emerged is that the physical phenomena and the tools employed to analyze such behavior are common to a wide class of partial differential equations models, both integrable and non-integrable.

Particular interest was devoted to DSW in hydrodynamics and in nonlinear optics, where many progresses have been made. In both areas the dispersive effects on breaking of waves was specifically assessed in the past both theoretically [73]–[75] and experimentally [76]–[78] in water waves (where DSW are commonly named as undular bores), as well as in fiber optics [79]–[81]. However, it is only recently that the renewed interest in DSWs have permitted to explore new regimes, to obtain new data with higher resolution, and to predict new phenomena [82]–[89]. This also allowed for making more accurate comparisons with the models in order to assess their limit of validity and the importance that previously neglected ingredients can have.

In this Chapter, we report a brief description of the generating mechanisms of dispersive shocks in optical fibers, and describe our experiments highlighting the role of the background on DSW visibility. We then report the experimental observation and the analytical description in the framework of the Whitham theory of the photonic analogue of the hydrodynamic dam breaking problem. We outline the theory we have developed to describe the emission of resonant radiation form DSW and our recent experimental results. We end the Chapter with the description of DSW in passive cavities and the high-order dispersion-induced emission of radiation.

3.2 Shock formation in optical fibers

For our purposes, a sufficiently accurate model for describing the propagation along an optical fiber of a pulse that modulates the a carrier at frequency ω_0 is the following NLSE:

$$iE_Z + ik_1 E_T - \frac{k_2}{2} E_{TT} + \gamma |E|^2 E = 0. \tag{3.1}$$

As far as the dispersive terms are concerned, for the time being, we restrict ourselves to the effect of leading order term, the second-order dispersion or GVD with coefficient k_2 (higher-order effects will be further discussed with reference to radiation driven by shock waves). When the GVD is weak, the correct way to derive a hydrodynamic limit of Eq. (3.1), is to make use of the Wentzel-Kramers-Brillouin (WKB) method (or, equivalently, the Madelung or geometric optics transformation) applied to the equation cast in the following semiclassical form:

$$i\varepsilon\psi_z - \beta_2 \frac{\varepsilon^2}{2} \psi_{tt} + |\psi|^2 \psi = 0, \tag{3.2}$$

where we have conveniently introduced the normalised variables $t = (T - k_1 Z)/T_0$ and $z = Z/\sqrt{L_d L_{nl}}$, $\beta_2 = \mathrm{sign}(k_2) = k_2/|k_2|$, as well as the following smallness dispersion parameter:

$$\varepsilon = \sqrt{\frac{L_{nl}}{L_d}} = \frac{1}{\sqrt{N}}, \tag{3.3}$$

where $L_{nl} = (\gamma P)^{-1}$ and $L_d = T_0^2/|k_2|$ are the nonlinear and dispersion length, respectively, $N = L_d/L_{nl}$ is the soliton order, $P = max(|E(Z=0,T)|^2)$ and T_0 are the peak power and the duration of the input envelope $E(Z=0,T)$. By inserting in Eq. (3.2) the WKB ansatz $u(t,z) = \sqrt{\rho(t,z)}\exp[iS(t,z)/\varepsilon]$, and introducing the chirp $u = -S_t$, we obtain:

$$\rho_z + \beta_2(\rho u)_t = 0, \tag{3.4}$$

$$u_z + \beta_2 u u_t + \rho_t = \varepsilon^2 \frac{1}{4}\left[\frac{\rho_{tt}}{\rho} - \frac{(\rho_t)^2}{2\rho^2}\right]_t. \tag{3.5}$$

Equations (3.4-3.5), without approximations, are fully equivalent to the NLSE (3.2). The so-called dispersionless limit of the NLSE is obtained by neglecting the RHS of Eq. (3.5), which is of higher-order $[O(\varepsilon^2)]$ with respect to the LHS of the equations that correspond to order $O(\epsilon^1)$ and $O(\epsilon^0)$, respectively. In this regime, the formation of the shock can be described in the framework of the reduced quasi-linear system of two equations [69], [71]:

$$\rho_z + \beta_2(\rho u)_t = 0; \qquad u_z + \beta_2 u u_t + \rho_t = 0. \tag{3.6}$$

The term dispersionless may be misleading, because terms due to the GVD still appears in Eqs. (3.6) through terms which retain the same order of the nonlinear terms. These terms turn out to be extremely important because they couple the self phase modulation (SPM) induced chirp to the power ρ. Therefore, when GVD is arbitrarily small but non-vanishing, the steepening of the pulse fronts can occur through SPM induced by Kerr effect.

Shock formation occurs when Eqs. (3.6) are hyperbolic, i.e. in the regime of normal GVD. In this case, the tendency to overtake is caused by the formation of a non-monotonic chirp which drives also the steepening of the power profile [80], until the gradients become so large that the dispersive effects associated with the RHS in Eq. (3.5) set in.

In the normal GVD regime ($\beta_2 = 1$), Eqs. (3.6) are identical to the shallow water equations (SWEs), which rule in 1D the propagation of the water elevation ρ and the (vertically averaged) horizontal velocity u, with interchanged role of space and time (in hydrodynamics the evolution variable is considered to be the time t, while the longitudinal distance plays the role of the time variable in fiber optics). In hydraulics these equations are also known as Saint Venant equations. Interestingly enough, they also have one to one correspondence to the so-called p-system which rule the gas dynamics for an isentropic gas with pressure law $p = \rho^2/2$. Importanty, the SWEs can also be cast in the diagonal form in terms of new variables $r^{\pm}(t,z) = u(t,z) \pm 2\sqrt{\rho}(t,z)$, which, in the language of the hyperbolic equation theory, are called Riemann invariants:

$$r_z^{\pm} + V^{\pm} r_t^{\pm} = 0, \tag{3.7}$$

where $V^{\pm} \equiv V^{\pm}(r^{\pm}) = (3r^{\pm} + r^{\mp})/4 = u \pm \sqrt{\rho}$ are the real eigenvelocities of the problem.

An additional formulation of Eqs. (3.6) refers to the form of a differential conservation law, which allows for introducing the classical shock waves with their characteristic associated velocities by means of extending the Rankine-Hugoniot (RH) condition [90] based on the integral formulation of the conservation law. For a scalar conservation law $u_z + f_t(u) = 0$, RH condition gives the shock velocity as:

$$\mathrm{V}_s = \frac{dt_s(z)}{dz} = \frac{[f]}{[u]}, \tag{3.8}$$

where $[\ldots]$ is the contracted notation for the difference of the quantity inside parenthesis across the jump. In the NLSE case the conservation law, which can be easily derived from Eqs. (3.6), is no longer a scalar one, but rather the following 2×2 vectorial form

$$\mathbf{q}_z + [\mathbf{f}(\mathbf{q})]_t = 0, \tag{3.9}$$

where $\mathbf{q} = (\rho, \rho u)^T$, and the flux turns out to be $\mathbf{f}(\mathbf{q}) = (\beta_2 \rho u, \beta_2 \rho u^2 + \rho^2/2)^T$. Physically, Eqs. (3.9) express the conservation of mass and momentum in differential form. When a classical shock (a step between left (ρ_L, u_L) and right (ρ_R, u_R) values) is introduced, the vectorial equivalent of the RH condition (3.8) can be introduced. However, since this becomes a vectorial condition which involves the same shock velocity V_s in the two components, it fixes not only the shock velocity but also the admissible values of the jump (i.e., the left (ρ_L, u_L) and right (ρ_R, u_R) values are not arbitrary but satisfies a constraint, a fact that bears no similarity with the scalar case) [82], [88], [90], [91]. The classical shock wave introduced in this way is crucial to develop a description of its dispersive regularization, i.e. of the DSW commonly observed in optical fibers. Furthermore, it is the key ingredient for properly describing the general evolution of step-like initial conditions. Below, we will discuss in more details the mechanisms of wave-breaking in the regime described by Eqs. (3.6), which is the one widely observed in nonlinear fiber optics experiments in the psec regime.

3.2.1 Mechanisms of wave-breaking in the normal GVD regime

The shallow water equations (3.6), or their equivalent diagonal [Eqs. (3.7)] or conservation law [Eqs. (3.9)] formulations, lead in general to the breaking of a smooth input pulse. For input bright and symmetric bell-shaped pulses $\psi_0 = \psi(t, z=0)$ with a generic finite background, steepening occurs symmetrically until two points of gradient catastrophe occur at finite distance on both the leading and trailing edges of the input pulse. The strong gradients are regularized by the dispersive term (RHS in Eqs. (3.4-3.5), which, in order to describe the post-breaking dynamics, is equivalent to reconsider the dimensionless NLSE:

$$i\varepsilon\psi_z - \frac{\varepsilon^2}{2}\psi_{tt} + |\psi|^2\psi = 0. \tag{3.10}$$

The dynamics ruled by Eq. (3.10) is smooth at any distance. The initial stage, ruled by Eqs. (3.6), is dominated by the nonlinearity which causes a steepening of the tails. The physical mechanism behind such steepening is the fact that the dominant Kerr nonlinearity induces a strong self-phase modulation. The acquired phase turns out to be proportional to the intensity $|\psi_0(t)|^2$, in turn implying an instantaneous frequency deviation or chirp $\delta\omega(t) = \partial_t \phi(t) = \partial|\psi_0(t)|^2$. Such a chirp is turned into an instantaneous change of velocity $\delta u(t) \propto -\delta\omega(t)$, according to the fact that in normally dispersive media the velocity decreases for increasing frequency. As a consequence the top parts of the pulse experience a larger absolute velocity towards the pulse tails (the velocity is negative on the leading edge of the pulse, and positive on the trailing edge, respetively), which is at the origin of the front steepening. Such process proceeds as the self-phase modulation grows along the fiber. However the point of infinite gradient (breaking) and successive overtaking is never reached. Indeed, as the gradient along the steepened front grows sufficiently large, the weak GVD becomes effective and spontaneous formation of oscillations start to become visible around the strongly steepened fronts. This usually occurs slightly before the breaking distance defined in the dispersionless limit ruled by Eqs. (3.6). The expanding oscillations form two symmetric DSWs, as shown in Fig. 3.1(b) for a Gaussian input, in dimensional units. They propagate and expands in opposite directions compared with the natural group-velocity of the wave.

A mathematical description of each of the two DSWs is possible on the basis of Whitham modu-

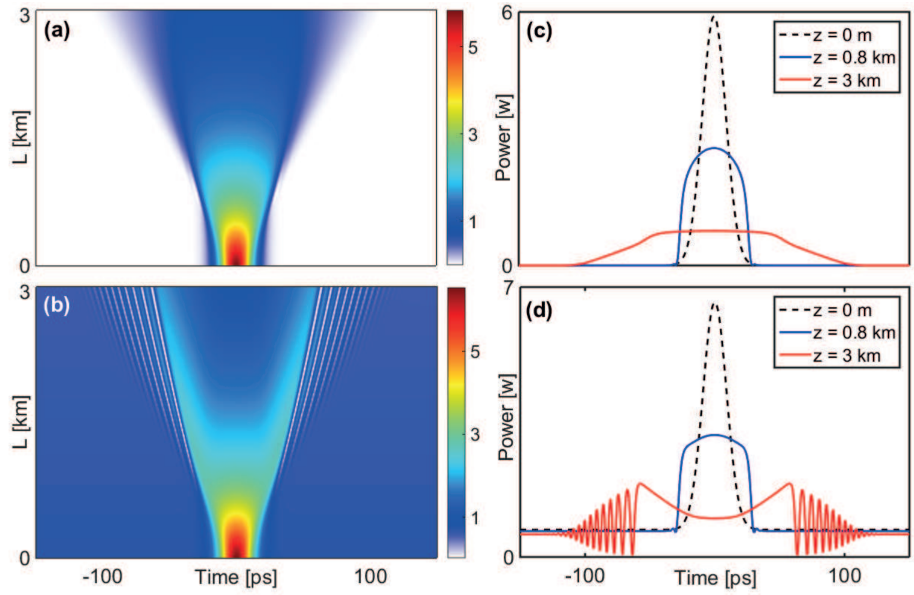

Figure 3.1 – (a-b) Level color-plot of power evolution (a) without and (b) with background, respectively, from numerical solution of Eq. (3.1). (c,d) intensity profiles for both cases at the output (red solid lines) and breaking distance $z = 0.8$ km (blue solid lines). The Gaussian input pulse (black dashed line) $A(t,0) = \sqrt{P}\exp(-t^2/t_0^2)$ with $P = 5.9$ W peak power and full width at half maximum duration $t_{FWHM} = \sqrt{2ln(2)}t_0 = 21.5$ ps, is superimposed on a background with power 0.6 W. Fiber parameters: $\beta_2 = 2.5 \times 10^{-26}\ s^2/m$, $\gamma = 3\ (W \cdot km)^{-1}$, losses $\alpha = 0.26\ dB/km$.

lation theory, which can be successfully formulated for the defocusing NLSE (3.10). According to such an approach, the DSW is described as a slowly varying modulation of a the invariant nonlinear traveling-wave periodic wave solution (so called dn-oidal or cn-oidal wave). The slowly varying parameters of such wave obey modulation equations which are obtained by performing a proper averaging [70] over the fast oscillation. For the defocusing NLSE the modulation equations are a set of four equations, which turns out to be hyperbolic and diagonalizable. A simple and smooth (rarefaction) solution of such equations allows to characterize the modulation and hence the DSW. An important point is that a single DSW is always characterized by two edges, as also clear from Fig. 3.1(b). One of the edge is such that the amplitude of the oscillations vanishes: this is the linear edge of the DSW (it corresponds to the trailing edge of the right-going DSW or the leading edge of the left-going DSW, see Fig. 3.1(b)). Over the opposite edge of the same DSW, which exhibits the deepest oscillation, the periodic solution locally reduces to a soliton (i.e. the modulus m of the Jacobian function locally tends to one): hence this is called the soliton edge of the DSW (it corresponds to the leading edge of the right-going DSW or the trailing edge of the left-going DSW, see Fig. 3.1(b)). The modulation theory allows to calculate the two velocities of the linear and soliton edges, respectively. However, it is worth pointing out that the modulation theory is an asymptotic method which provides a good description only for large enough propagation distances and/or small enough dispersion parameter ε. In any event the dynamics of DSWs developing from smooth initial data cannot have strict correspondence with the DSW construction based on the modulation equations, since the latter implies an initial condition for the modulation equation in the form of a step. Conversely, a quantitative test of

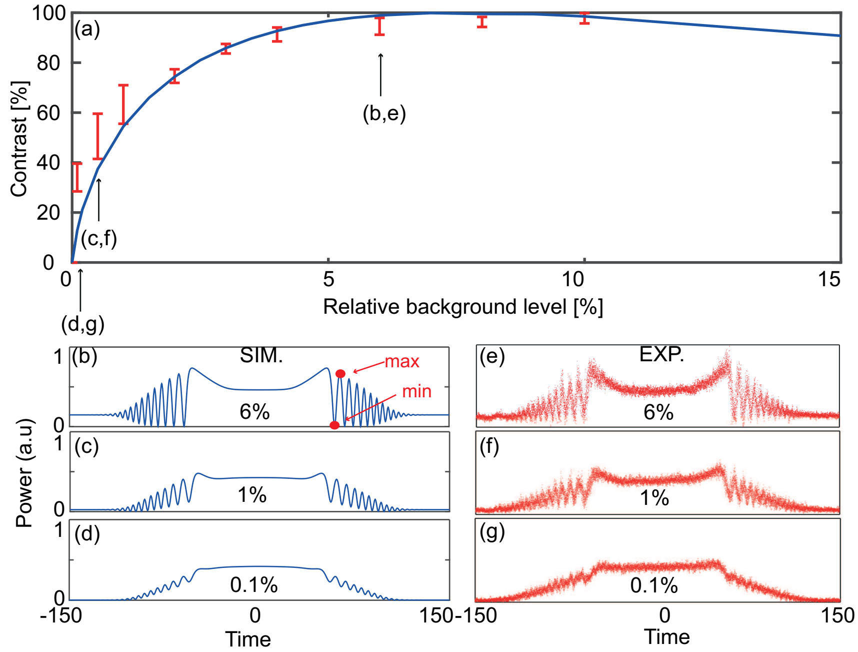

Figure 3.2 – Effect of pulse background on shock formation: (a) Contrast of the DSW fringe $(P_{max} - P_{min})/(P_{max} + P_{min})$, defined relative to the DSW leading edge, as shown in (b), versus percentage of the background (relative to the input peak power). (b) to (g): examples of different calculated and measured intensity profiles for 0.1, 1, and 6 % background level: (b) to (d) numerics from NLSE; (e) to (g) experimental results.

the outcome of the modulation theory becomes possible by injecting step-like pulses, a case that we treat separately in the following.

It is important to emphasize that the pulse background has a strong influence on the formation of the DSW, particularly in terms of the contrast of the oscillations. This is clear from Figs. 3.1, where Figs. 3.1(a,c) contrast the evolution relative to the input without background, with the case of the Gaussian with background in Fig. 3.1(b,d). This is the reason for which early measurements in fibers [81] reported a much lower contrast compared with later spatial experiments performed with non zero background [92]. We performed a detailed experimental study of the effects of the background [87]. Figure 3.2(a) summarizes the contrast of the oscillations (defined conventionally for the first fringe, as indicated in Fig. 3.2(b)) measured as a function of the background (in percent of the peak power of the pulse), while examples for background levels corresponding to 0.1, 1, 6% are shown in Fig. 3.2(b-g), comparing experimental results and NLSE simulations. As shown, the contrast of the oscillation is rapidly enahanced by increasing the background, reaching a saturated contrast of 100 % where the minimum power of the leading edge touches zero. At larger background levels the contrast smoothly decreases since such null point shifts from the leading edge of the DSW, a phenomenon that can be accurately described in the framework of the so-called dam breaking experiment concerning step initial data (see below). A physical insight into the role of the background can be gained as follows. The oscillating wavetrain in the DSW can be understood as the interference phenomenon between original components with zero chirp (the background) and new frequencies generated via the nonlinearity and GVD which coexist on the temporal regions which correspond to the steepened

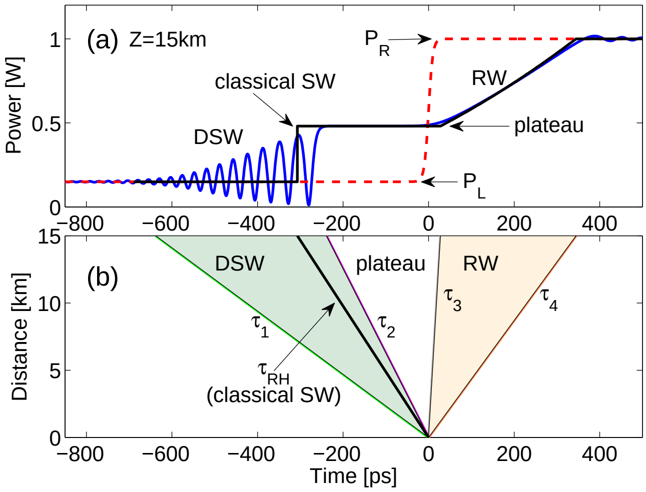

Figure 3.3 – (a) Snapshots comparing in real units the DSW-RW pair (solid blue curve) obtained from the NLSE with step-like input $E(T,0) = [P_L + (P_R - P_L)(1 + \tanh(T/T_r))/2]^{1/2}$ (dashed red) with the ideal dispersionless solution of the SWEs (solid black). (b) Wedges in real-world time-distance plane (T,Z), corresponding to the RW (fable orange), the DSW (green) and the plateau in between (white). The boundaries correspond to slopes $\sqrt{k_2 \gamma P_R}\tau_j$, $j = 1,2,3,4$. Here $k_2 = 176$ ps^2/km, $\gamma = 3$ (W km)$^{-1}$, $P_R = 1$ W, $P_L = 150$ mW, $T_r = 10$ ps, as in the experiment.

tails of the pulse. The resulting pattern is characterized by the frequency difference and a visibility which depends on the amplitude ratio between such frequency components, thus requiring the background to be sufficiently large to give rise to a large contrast.
It is worth emphasizing that, in the spectral (Fourier) domain, the wave-breaking process is characterised by a strong spectral broadening. Indeed the steepening process corresponds to the generation of high frequencies in the spectrum. Beyond the breaking distance the spectrum does not substantially reshape while the DSW spread (see Fig. 3.6(b) below, for an example of this behaviour). In this regime, roughly speaking, the spectrum extends up to the highest frequencies of the generally non-monochromatic oscillations. We have recently proposed an estimate of the broadening, see [89]. Such a dramatic spectral broadening has been shown to be highly beneficial for several applications such as supercontinuum generation and comb spectroscopy [93].

3.3 Riemann problem and dam breaking

In the theory of quasi-linear hyperbolic partial differential equations such as the SWEs, a fundamental problem is the evolution of a step-like initial condition, which is known as the Riemann problem [90]. The solution to such problem is indeed a building block for understanding the scenario of possible evolutions as well as for developing numerical schemes of integration (Riemann solvers). According to the general theory, a step-like initial condition of a 2×2 problem, such as the SWEs, decays into a pair of fundamental waves, which can be of the shock wave or rarefaction wave type, respectively. In general a step initial condition involves a jump in both the variables ρ and u, which vary from the left (ρ_L, u_L) to the right (ρ_R, u_R) constant state, where, without loss of generality, the step is assumed to be located in $t = 0$, so that subscripts L and R refer to $t < 0$ and $t > 0$, respectively. In terms of Riemann invariants one has also step-initial conditions from the left values $r_L^{\pm} = u_L \pm \sqrt{\rho}_L$ to the right values $r_R^{\pm} = u_R \pm \sqrt{\rho}_R$. According to the specific value of the four boundaries $r_{L,R}^{\pm}$, the SWEs give rise to different evolutions which involve the decay into wave pairs of the type: (i) rarefaction-rarefaction; (ii) shock-shock; (iii) rarefaction-shock [72], [90]. In particular, the latter case can be accessed by implementing only a step in the power variable ρ with the initial chirp being identically vanishing, which can be more easily accessed experimentally. In this case, the Riemann problem for the SWEs is known, in the context of hydrodynamics, as the dam-break problem, namely, the 1D evolution that follows the instantaneous removal (rupture) of a dam separating different downstream (ρ_L) and upstream ($\rho_R > \rho_L$) levels of still water. In this case the solution to the SWEs is composed by a rarefaction wave and a classical shock wave pointing in opposite directions (upstream and downstream, respectively) separated by a constant expanding plateau. Figure 3.3 illustrates the profile of ρ for such solution (see black solid line in Fig. 3.3(a)), contrasting it with the dispersive counterpart obtained from the numerical solution of the full NLSE (blue solid line in Fig. 3.3(a)) with step-like initial power profile (dashed red line in Fig. 3.3(a)). As shown, the solution arising from the SWEs or dispersionless limit gives a quantitatively good description of the NLSE dynamics for what concerns the smooth part that includes the rarefaction wave and the plateau. Conversely, the classical shock is replaced by a DSW as expected on the basis of the general principles illustrated before. In this situation, the edge velocities of the DSW can be predicted by applying the Whitham averaging theory. Such velocities are conveniently expressed in terms of the self-similar variable $\tau = t/z$. In the present case the boundary conditions for the shock are given by the intermediate constant values of the plateau $\rho_i = (\sqrt{\rho_L} + \sqrt{\rho_R})^2/4$, $u_i = \sqrt{\rho_L} - \sqrt{\rho_R}$ and the quiescent left state $\rho_L, u_L = 0$. This allows for expressing the linear (say τ_1) and the soliton (say τ_2) edge velocities as a function of ρ_L and ρ_R only, obtaining:

$$\tau_2 = -\frac{\sqrt{\rho_L} + \sqrt{\rho_R}}{2}; \;\; \tau_1 = \frac{\rho_L - 2\rho_R}{\sqrt{\rho_R}}. \tag{3.11}$$

Conversely, the Whitham averaging give for the edge velocities of the rarefaction wave, say τ_3 and τ_4, the same expression which is obtained in the dispersionless limit from the SWEs, which read as:

$$\tau_4 = \sqrt{\rho_R}; \;\; \tau_3 = \frac{3\sqrt{\rho_L} - \sqrt{\rho_R}}{2}. \tag{3.12}$$

All of such velocities define, in the plane (t, z), the wedges where the three components (rarefaction, plateau, and DSW) expand, as displayed in Fig. 3.3(b).
Importantly, unlike experiments performed with smooth pulse waveform, the dam-break problem gives the unique opportunity to quantitatively test the Whitham modulation theory against experimental results. In this respect, it is important to emphasize that the modulation theory predicts for the DSW a critical transition where the DSW envelope is no longer monotone (as in Fig. 3.3(a)), but rather exhibit cavitation associated with the appearance of a vacuum point where the optical intensity vanishes. Such a transition occurs when the crucial parameter, namely the ratio of quiescent states $r = \rho_L/\rho_R$, decreases below the threshold value $r = r_{th} = 1/9 \simeq 0.11$. In the limit $r \to 0$ ($\rho_L \to 0$), the vacuum point shifts towards the linear edge of the DSW, but at the same time, the amplitude of the DSW oscillations vanishes. In this limit the shock disappears and the dynamics involves a single rarefaction wave, recovering the solution of the SWEs in the so-called dry bed case (a vanishing level of water downstream) [94].

We have recently observed the dam-breaking dynamics by means of a full fiber set-up [88]. The input shape, obtained by means of an electro-optic modulator driven by a generator of

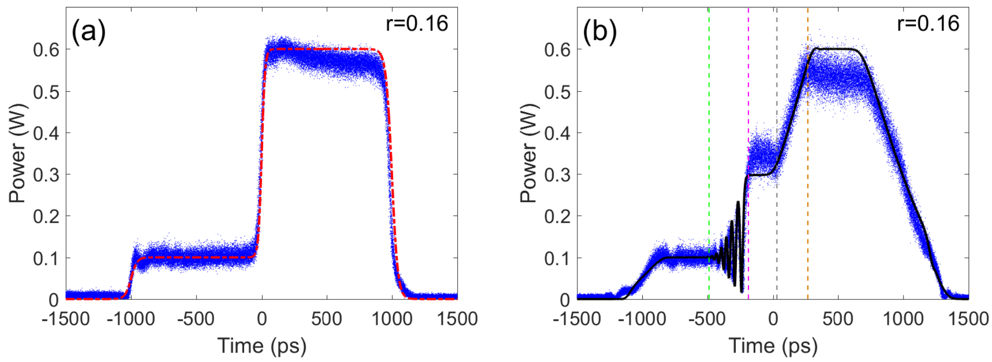

Figure 3.4 – Temporal traces of the whole waveform: experiment (blue dots) vs. numerics based on the NLSE (black curve; the input is in dashed red): (a) input power profile; (b) output power profile after propagation along a 15 km long fiber. The vertical dashed lines give the predicted delays of the edges of the DSW (magenta and green lines, from Eqs. (3.11)) and the RW (gray and orange lines, from Eqs. (3.12)), respectively.

arbitrary waveform is shown in Fig. 3.4(a). This shape allows for observing the formation of the rarefaction-DSW pair for the increasing step between the two states with non-vanishing powers P_L and P_R, while observing, at the same time, the dry-bed dynamics on the decreasing step from P_R to zero. The parameter of the fiber employed in the experiment are reported in the caption of Fig. 3.3. The relatively large GVD ($k_2 = 176$ ps^2/km) permits to have the oscillation period of the DSW, which scales as $\sqrt{k_2/\gamma P_i}$, in the tens of psec range, allowing for a good resolution of the DSW. An other crucial feature of the experiment is the compensation of the fiber losses, which would cause a strong deviation from the expected dynamics, by means of a counterpropagating Raman pump. Figure 3.4(b) shows the output profile after the propagation through the 15 km fiber. The measured profile clearly show the rarefaction-DSW structure, which turns out to be in good agreement with the NLSE simulation and with the delays calculated from modulation theory (dashed vertical lines). Conversely, only a rarefaction is observed on the trailing edge of the pulse.
Figure 3.5 shows a detail of the DSW soliton edge, obtained for a fixed $P_R = 1$ W and variable P_L (variable ratio r). The measured profiles clearly show the critical transition to cavitation at the threshold value $r = 0.11$ (in full quantitative agreement with modulation theory), where the soliton at the edge of the DSW becomes black. Further decreasing r makes the vacuum point shifting towards the linear edge of the DSW, again in good quantitative agreement with modulation theory and NLSE simulations.

3.4 Resonant radiation emitted by dispersive shocks

Bright solitons propagating in standard or photonic crystal fibers close to the zero-dispersion wavelength (ZDW) are known to emit resonant radiation (RR), also called dispersive wave (DW), in the region of normal GVD. The underlying mechanism is the resonant coupling with linear dispersive waves induced by higher-order dispersion [95]. The emission of RR is usually thought to be a prerogative of solitons, but experimental observations [96] and our theoretical investigations [91], [97], proved that this is not necessarily the case. In particular, the DSWs, which develop in the regime of weak dispersion, resonantly amplify RR at frequencies given by a

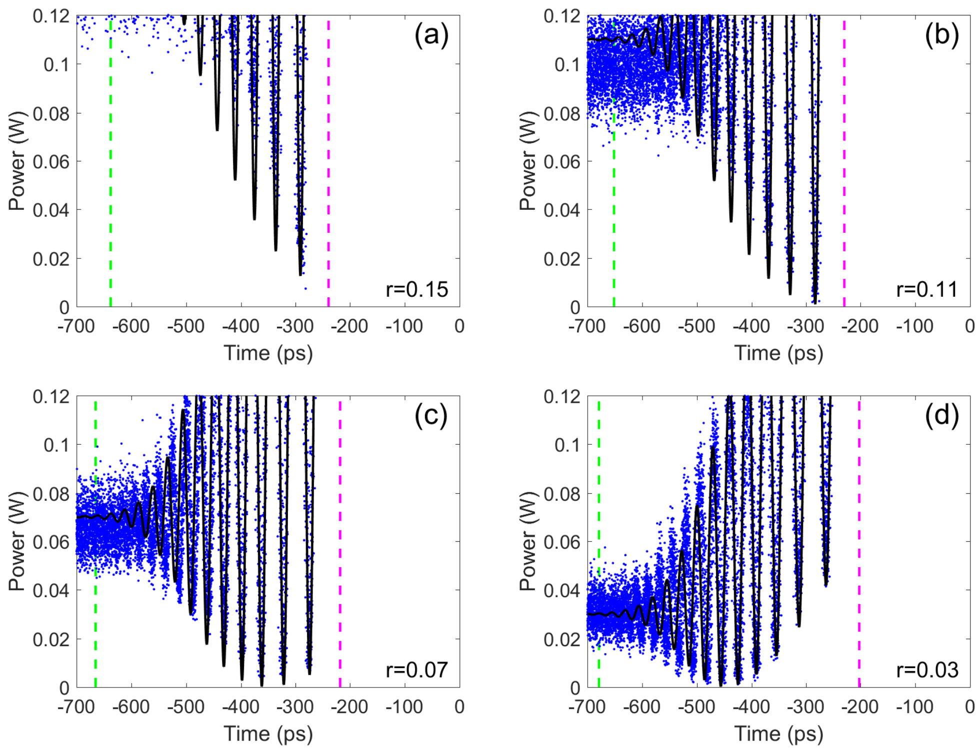

Figure 3.5 – (a-d) Zoom around the soliton edge of the DSW, showing the transition to cavitation, for fixed $P_R = 1$ W and different fractions $r = P_L/P_R$: (a) 0.15; (b) 0.11 (cavitation threshold); (c) 0.07; (d) 0.03.

specific phase-matching selection rule. In fact, the strong spectral broadening that accompanies wave-breaking seeds linear waves, which may be resonantly amplified thanks to the well defined velocity of the shock front.
Consider, for example, a standard telecom fiber (Corning MetroCor) with nonlinear and dispersion parameters as follows: $\gamma = 2.5$ W^{-1}km^{-1}, $k_2 = 6.4$ ps^2/km, $k_3 = 0.134$ ps^3/km, and $k_4 = -9 \times 10^{-4}$ ps^4/km (higher-order terms are negligible), which gives a ZDW $\lambda_{ZDW} = 1625$ nm [96]. Figure 3.6 shows the temporal and spectral propagation of a hyperbolic secant pulse in the normal dispersion regime of the fiber, obtained from the numerical solution of generalized NLSE, which accounts for higher-order nonlinear terms in full integral form [98]. The pulse undergoes a steepening of the leading and trailing edge, that leads to wave breaking at a propagation distance of 20 meters. After the breaking, two DSWs develop with broken symmetry (in time) due to the presence of third order dispersion. The spectrum is broadest at the breaking point, and clearly shows a narrowband peak in the anomalous dispersion region. This peak can be interpreted as a resonant radiation emitted by the leading edge of the pulse. In the next Section, we will show how to predict the spectral position of this resonant radiation.

3.4.1 Phase matching condition

We develop our analysis starting from the NLSE suitably extended to account for the effects of higher order dispersion (HOD). In particular we extend the semiclassical form of NLSE [Eq.

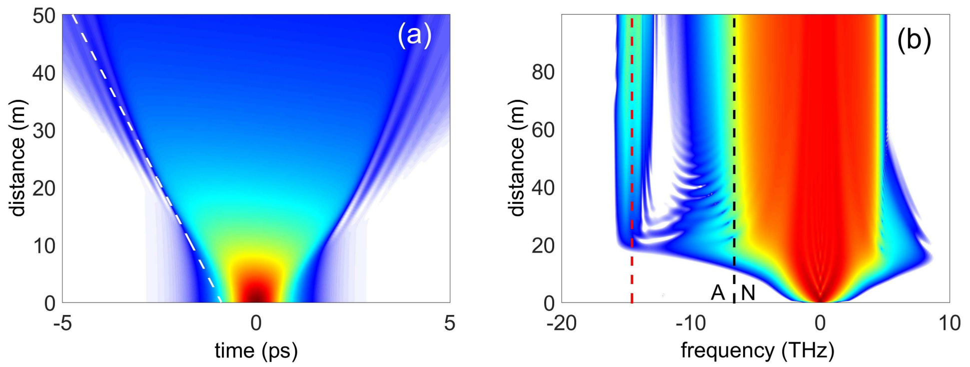

Figure 3.6 – Temporal (a) and spectral (b) evolution of an input sech pulse $P_0 = 600$ W, $T_0 = 850$ fs, at $\lambda_p = 1568.5$ nm (normal GVD). A/N labels anomalous/normal GVD regions, and the dashed red lines stand for the RR detuning predicted by Eq. (3.16) with velocity given by oblique dashed line in (a).

(3.2)] to include HOD terms, while we safely neglect Raman and self-steepening due to the pulse duration and power range that we consider. By defining the dispersion coefficients as $\beta_n = \partial_\omega^n k / \sqrt{(L_{nl})^{n-2}(\partial_\omega^2 k)^n}$, we recover the defocusing NLSE in the weakly dispersing form:

$$i\varepsilon\partial_z\psi + d(i\varepsilon\partial_t)\psi + |\psi|^2\psi = 0, \tag{3.13}$$
$$d(i\varepsilon\partial_t) = \sum_{n\geq 2} \tfrac{\beta_n}{n!}(i\varepsilon\partial_t)^n = -\tfrac{\varepsilon^2}{2}\partial_t^2 - i\tfrac{\beta_3\varepsilon^3}{6}\partial_t^3 + \tfrac{\beta_4\varepsilon^4}{24}\partial_t^4 + \ldots$$

where we considered normal GVD ($\beta_2 = 1$). Note that the normalized dispersive operator $d(i\varepsilon\partial_t)$ has progressively smaller terms, weighted by powers of the parameter $\varepsilon \ll 1$ and coefficients β_n. The process of wave-breaking ruled by Eq. (3.13) can be described by applying again the Madelung transformation $\psi = \sqrt{\rho}\exp(iS/\varepsilon)$. At leading-order in ε, we obtain a quasi-linear hydrodynamic reduction, with $\rho = |\psi|^2$ and $u = -S_t$ equivalent density and velocity of the flow, which can be further cast in the form [91]:

$$\rho_z + \left[\beta_2\rho u + \frac{\beta_3}{2}\rho u^2 + \frac{\beta_4}{6}\rho u^3 + \ldots\right]_t = 0, \tag{3.14}$$
$$(\rho u)_z + \left[\beta_2\rho u^2 + \frac{\beta_3}{2}\rho u^3 + \frac{\beta_4}{6}\rho u^4 + \ldots + \frac{1}{2}\rho^2\right]_t = 0, \tag{3.15}$$

of a conservation law $\mathbf{q}_z + [\mathbf{f}(\mathbf{q})]_t = 0$ for mass and momentum, with $\mathbf{q} = (\rho, \rho u)$, which suitably extends Eqs. (3.9). For small $\beta_{3,4}$, Eqs. (3.14-3.15) continue to be hyperbolic, thus admit weak solutions in the form of classical shock waves, i.e. traveling jumps from left (ρ_l, u_l) to right (ρ_r, u_r) values, whose velocity V_c can be found from the generalised RH condition (i.e., the natural extension of Eq. (3.8) as discussed before): $V_c(\mathbf{q}_l - \mathbf{q}_r) = [\mathbf{f}(\mathbf{q}_l) - \mathbf{f}(\mathbf{q}_r)]$ [90]. However, the jump is regularized by GVD in the form of a DSW. In this regime, the shock velocity can be identified with the velocity V_s of the steep front near the deepest oscillation (DSW leading edge), which differs from V_c and can be determined numerically. For very specific initial contitions, it can be determined analytically [91]. The strong spectral broadening that accompanies steep front formation can act as an efficient seed for RR which are phase-matched to the shock in its moving frame at velocity V_s.

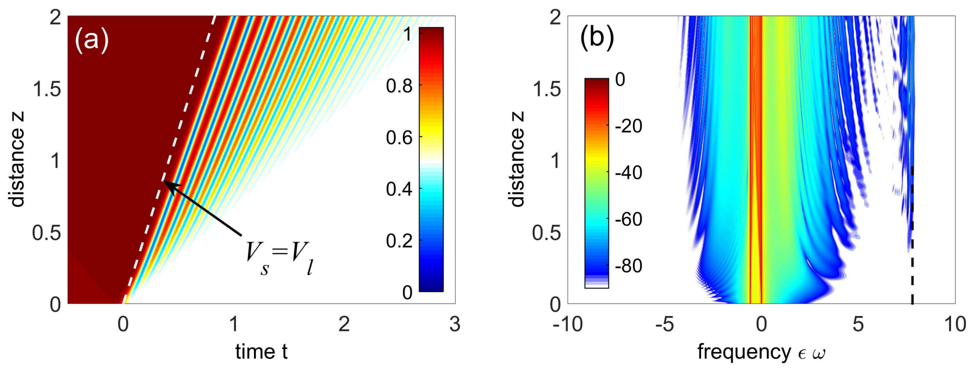

Figure 3.7 – Radiating DSW ruled by NLSE (3.13) with $\varepsilon = 0.03$, input step $\rho_l, \rho_r = 1, 0.5$, and TOD $\beta_3 = -0.35$: (a) Color level plot of density $\rho(t,z)$ (the dashed line gives the DSW leading edge velocity V_l); (b) corresponding spectral evolution.

In order to calculate the frequency of the DW, we assume an input pump $\psi_0 = \psi(t, z = 0)$ with central frequency $\omega_p = 0$ [i.e., in real-world units ω_p coincides with ω_0, around which $d(i\varepsilon\partial_t)$ in Eq. (3.13) is expanded]. Let us denote as $V_s = dt/dz$ the "velocity" of the SW near a wave-breaking point and as $\tilde{d}(\varepsilon\omega) = \sum_n \frac{\beta_n}{n!}(\varepsilon\omega)^n$ the Fourier transform of $d(i\varepsilon\partial_t)$. Linear waves $\exp(ik(\omega)z - i\omega t)$ are resonantly amplified when their wavenumber in the shock moving frame, which reads as $k(\omega) = \frac{1}{\varepsilon}\left[\tilde{d}(\omega) - V_s(\varepsilon\omega)\right]$ equals the pump wavenumber $k_p = k(\omega_p = 0) = 0$. Denoting also as k_{nl} the difference between the nonlinear contributions to the pump and RR wavenumber (the nonlinear contribution to the wawenumber of the resonant radiation is induced by cross-phase modulation with a non-zero background, on top of which RR propagates), respectively, the radiation is resonantly amplified at frequency detuning $\omega = \omega_{RR}$ that solves the explicit equation [91]

$$\sum_n \frac{\beta_n}{n!}(\varepsilon\omega)^n - V_s(\varepsilon\omega) = \varepsilon k_{nl}. \tag{3.16}$$

We show below that Eq. (3.16) correctly describes the RR emitted by a DSW. At variance with solitons of the focusing NLSE where $V_s(\omega_p = 0) = 0$ [95], DSWs possess non-zero velocity V_s, which must be carefully evaluated, having great impact on the determination of ω_{RR}.

3.4.2 Step-like pulses

We consider first a step initial value that allows us to calculate analytically the velocity. Without loss of generality, we take $\beta_3 < 0$. Specifically, we consider the evolution of an initial jump from the "left" state $\rho_l, u_l = 0$ for $t < 0$ to the "right" state $\rho_r(< \rho_l), u_r = 2(\sqrt{\rho_r} - \sqrt{\rho_l})$ for $t > 0$ [82], [91]. The leading edge of the resulting DSW can be approximated by a gray soliton, whose velocity can be calculated as $V_l = \sqrt{\rho_l} + u_r = 2\sqrt{\rho_r} - \sqrt{\rho_l}$ [82], [91].

If we account for $k_{nl} = k_{nl}^{sol} - k_{nl}^{RR} = -\frac{1}{\varepsilon}\rho_l$ arising from the soliton $k_{nl}^{sol} = \rho_l/\varepsilon$ and the cross-induced contribution $k_{nl}^{RR} = 2\rho_l/\varepsilon$ to the RR, Eq. (3.16) explicitly reads as

$$\frac{\beta_3}{6}(\varepsilon\omega)^3 + \frac{\beta_2}{2}(\varepsilon\omega)^2 - V_s(\varepsilon\omega) + \rho_l = 0. \tag{3.17}$$

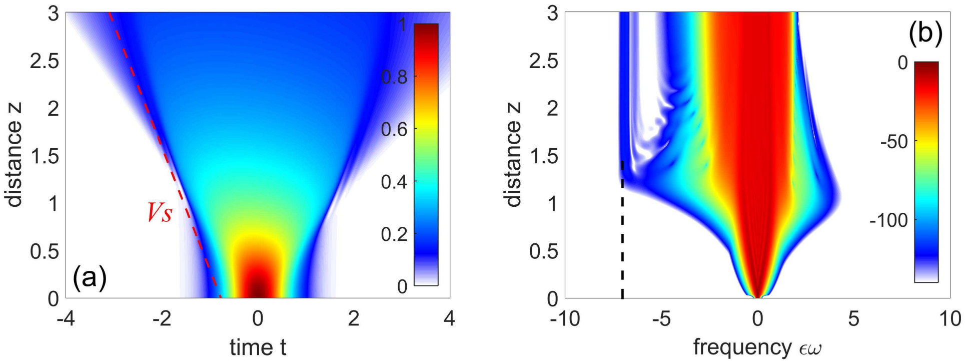

Figure 3.8 – (a,b) Temporal and spectral evolution of a Gaussian pulse without background emitting RR, for $\beta_3 = 0.35$, and $\varepsilon = 0.03$.

Real solutions $\omega = \omega_{RR}$ of Eq. (3.17) correctly predict the RR as long as $|\beta_3| < 0.5$, as shown by the NLSE simulation in Fig. 3.7. The DSW displayed in Fig. 3.7(a) clearly exhibits a spectral RR peak besides spectral shoulders due to the oscillating front, as shown by the spectral evolution in Fig. 3.7(b). Perfect agreement is found between the RR peak obtained in the numerics and the prediction [dashed vertical line in Fig. 3.7(b)] from Eq. (3.17) with velocity $V_s = V_l$. We also point out that k_{nl} represents a small correction, so ω_{RR} can be safely approximated by dropping the last term in Eq. (3.17) to yield $\varepsilon\omega_{RR} = \frac{3}{2\beta_3}\left(-\beta_2 \pm \sqrt{\beta_2^2 + 8V_s\beta_3/3}\right)$, that can be reduced to the simple formula $\varepsilon\omega_{RR} = -\frac{3\beta_2}{\beta_3}$ [96] only when $\beta_3 V_s \to 0$.

3.4.3 Bright pulses

The behaviors of step initial data are basically recovered for pulse waveforms that are more manageable in experiments. As shown in Fig. 3.8, RR occurs also in the limit of vanishing background, allowing us to conclude that a bright pulse does not need to be a soliton (as in the focusing NLSE, $\beta_2 = -1$) to radiate. In fact, resonant amplification of linear waves occurs via SWs also in the opposite regime where the nonlinearity strongly enforces the effect of leading-order dispersion, the only key ingredients being a well defined velocity of the front and the spectral broadening that seeds the RR at phase-matching. Experimental evidence for such RR scenario was reported quite recently [96], corresponding to numerical simulations reported in Fig.3.8. The physical parameters used to obtain Fig. 3.8, gives normalized parameters $\varepsilon \simeq 0.07$ and $\beta_3 \simeq 0.37$, typical of the wave-breaking regime ($\varepsilon \ll 1$) with perturbative third order dispersion (TOD). Since $\beta_3 > 0$, the radiating shock turns out to be the one on the leading edge ($t < 0$), and its velocity $V_s = -0.75$, inserted in Eq. (3.16), gives a negative frequency detuning $\Delta f_{RR} = \omega_{RR} T_0^{-1}/2\pi \simeq 13$ THz, in excellent agreement with the value reported in Ref. [96]. We performed a detailed numerical study of this particular case, including Raman effects in [97].

3.4.4 Periodic input

We are interested in the evolution ruled by Eq. (3.13) subject to the dual-frequency initial condition

$$\psi_0 = \sqrt{\eta}\exp(i\omega_p t/2) + \sqrt{1-\eta}\exp(-i\omega_p t/2), \tag{3.18}$$

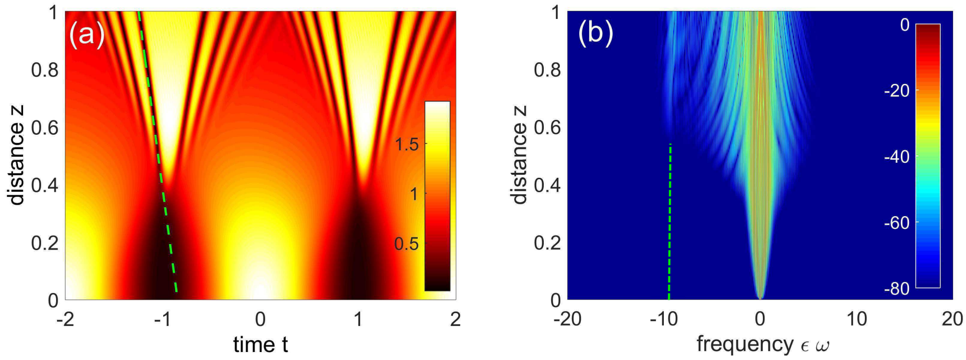

Figure 3.9 – RR emitted by shock with asymmetric pumping $\eta = 0.3$, and $\varepsilon = 0.04$: (a) temporal and (b) spectral colormap evolution for $\beta_3 = 0.3$; Dashed line in (a) highlights the DSW edge velocity $V = -0.4$. Vertical dashed line in (b) indicates ω_{RR} from Eq. (3.16) with $k_{nl} = -|\psi_0|^2/\varepsilon$.

where we fix the normalized frequency $\omega_p \equiv \Omega T_0 = \pi$ by choosing $T_0 = 1/2\Delta f = \pi/\Omega$. The dynamics is ruled, in this case, by the single smallness parameter $\varepsilon = \Delta f \sqrt{4k_2/(\gamma P)}$ [99]. Here η accounts for the possible imbalance of the input spectral lines. In this case a frequency comb is generated thanks to multiple four wave mixing (mFWM). Formation of DSWs, occurring in the regime of weak normal dispersion ($\beta_2 = 1$), enhances the broadening of the comb towards high orders of mFWM. We have demonstrated that, when such DSWs are excited sufficiently close to a ZDW, they are expected to generate RR, owing to phase-matching with linear waves induced by higher-order dispersion [100]. An example of the RR ruled by TOD (we set $\beta_3 = 0.3$) is shown in Fig. 3.9 for an imbalanced input [$\eta = 0.3$ in Eq. (3.18)]. The colormap evolution in Fig. 3.9(a) clearly shows that the initial waveform undergoes wave-breaking around $z \sim 0.4$. The mechanism of breaking has been analysed in details in Ref. [99] and involves two gradient catastrophes occurring across each minimum of the injected modulation envelope. The GVD regularizes the catastrophes leading to the formation of two DSWs, where the individual oscillations in the trains exhibits dark soliton features, moving with nearly constant darkness and velocity inversely proportional to it. Importantly, the breaking scenario is weakly affected by TOD; However, one can notice that the darkest soliton-like oscillation emits RR. This radiation has much higher frequency than the comb spacing and turns out to be generated over the CW plateau of the leading edge labeled ψ_0. This is clear from Fig. 3.9(b), which shows the enhancement of such frequency at the distance of breaking where the strong spectral broadening associated with the shock acts as a seed for the phase-matched (resonant) frequency.

3.4.5 Experimental observations

We have observed experimentally the emission of multiple dispersive waves from a DSW [101]. Each individual dispersive wave can be associated to one particular soliton-like oscillation in the modulated nonlinear wave using the theory described above. The DSW has been generated by launching two delayed co-propagating pulses in the normal dispersion region of the optical fiber [102]. At the initial stage of propagation, the two pulses temporally broaden and acquire a linear chirp due to dispersion and self-phase modulation. Once they overlap in time, they interfere forming a pulse with sinusoidally modulated intensity. With further propagation, this temporal modulation nonlinearly reshapes into a DSW, which asymptotically approach a train of dark

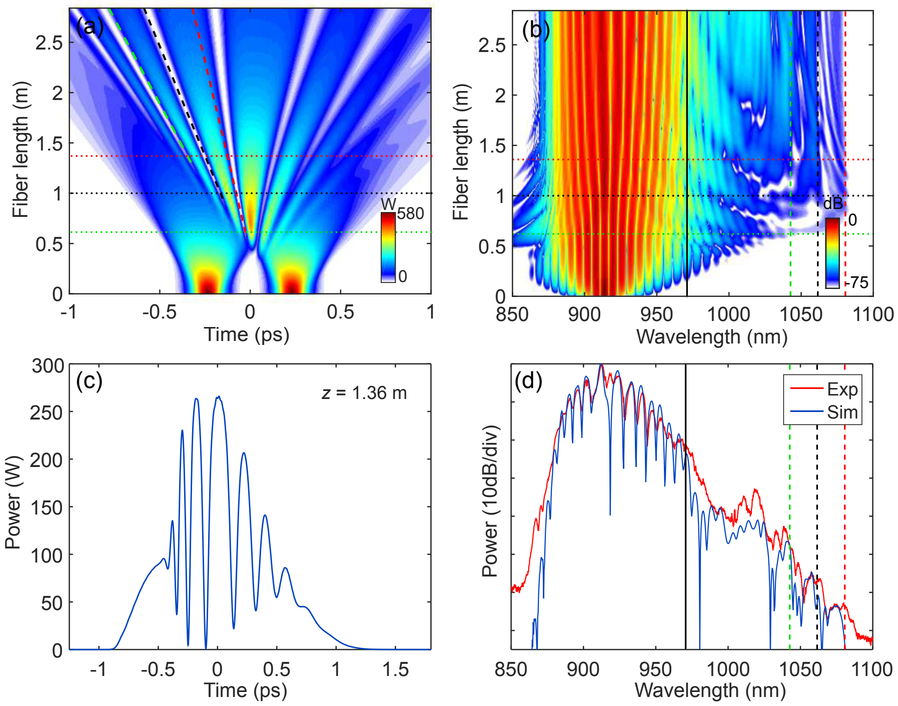

Figure 3.10 – Generation of RRs from multiple dark solitons. (a) Simulated temporal evolution versus fiber length. The dashed lines correspond to the velocity of each soliton emitting a DW. (b) Corresponding spectral evolution versus length. The vertical solid and dashed lines correspond respectively to the ZDW and the RR wavelengths calculated using Eq. (3.16) with the corresponding soliton velocity [of same color as in (a)]. In (a) and (b), the fiber lengths at which RRs are emitted ($z = 1.36$, 1 and 0.62 m) are represented by dotted horizontal lines. (c) Simulated temporal evolution at $z = 1.36$ m, i.e. where the first RR is emitted. (d) Simulated (blue line) and measured (red line) spectra at the output of a 2.8 m-long PCF. Initial pulse delay: 465 fs.

solitons [102].

Figure 3.10 summarizes the numerical and experimental results obtained for an input delay of 465 fs. The temporal map plotted in Fig. 3.10(a) shows that six dips are formed within the first meter of propagation. The corresponding spectral map shown in Fig. 3.10(b) exhibits three main radiations in the anomalous dispersion region. The first one, generated after a propagation length of 1.36 m, is located at 1038 nm, the second one generated after 1 m is located at 1058 nm, and the third one generated after 0.62 m is located at 1076 nm. The temporal profile simulated at 1.36 m (i.e. where the first RR is emitted) is represented in Fig. 3.10(c). It shows that the three dark solitons located on the leading edge (with negative velocities) are much sharper and shorter than the three ones of the trailing edge (having positive velocities). As outlined before, we calculated the velocity V_s of each soliton from the (t,z) map (illustrated by dashed lines in Fig. 3.10(a) for the three shortest dark solitons) and we calculated the corresponding phase-matched RR wavelength from Eq. (3.16). They are represented in Fig. 3.10(b) with the corresponding color, and show good agreement with the observed radiations in simulations. Finally, Fig. 3.10(d) shows the experimental output spectrum in red solid line, which is in excellent agreement with

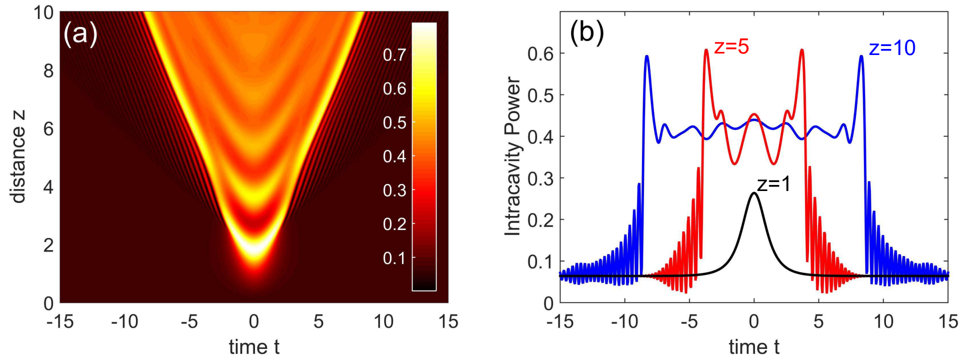

Figure 3.11 – DSW generation ruled by Eq. (3.19). (a) Color level plot of intracavity power $|\psi(z,t)|^2$. (b) Snapshots of intracavity power at difference distances. Here $\varepsilon = 0.1$, $\delta = \pi/10$, $\alpha = 0.03$

the simulated one (in blue) and with solutions of the phase-matching relation (Eq. (3.16)) for the three fastest solitons (vertical dashed lines). These results highlight the generation of three RRs originating from the three different dark solitons which can be identified through their group velocity.

3.5 Shock waves in passive cavities

Passive nonlinear cavities which are externally driven have been recently become popular, and have been implemented both in fiber rings and monolithic microresonators. They are exploited for fundamental studies as well as impactful applications such as the formation of wide-span frequency combs. Such resonators exhibit extremely rich dynamics characterized by a host of phenomena such as bistability, modulational instability and soliton formation, as discussed in Chapter 1. It has been recently shown that passive cavities admits a novel dynamical behavior featuring the formation of dispersive-dissipative shock waves [103]. These phenomena are well captured by a mean the Lugiato-Lefever equation. By accounting for HOD, a generalized LLE can expressed in dimensionless units as:

$$i\varepsilon\psi_z + d(i\varepsilon\partial_t)\psi + |\psi|^2\psi = [\delta - i\alpha]\psi + iS, \tag{3.19}$$

where we adopt the normalisation introduced in Ref. [103], [104]. We just recall that the parameter $\varepsilon = \sqrt{L/L_d} \ll 1$ (L and $L_d = T_0^2/k_2$ are the fiber (cavity) length and the dispersion length associated with time scale T_0 and GVD) quantifies the smallness of the GVD and the HOD introduced through the operator $d(i\varepsilon\partial_t) = \sum_{n\geq 2}\beta_n(i\varepsilon\partial_t)^n/n! = -\beta_2\varepsilon^2\partial_t^2/2 - i\beta_3\varepsilon^3\partial_t^3/6 + \ldots$, where the coefficients $\beta_n = \partial_\omega^n k/\sqrt{(L)^{n-2}(\partial_\omega^2 k)^n}$ [note that $\beta_2 = \mathrm{sign}(\partial_\omega^2 k)$] are related to real-world HOD $\partial_\omega^n k$.
Let us first neglect the HOD terms ($\beta_n = 0$, $n > 2$). Equation (3.19) can exhibit a bistable response with two coexisting stable branches of CW solutions. A DSW can be seen as a fast oscillating modulated wavetrain that connects two sufficiently different quasi-stationary states. Starting from a cavity biased on the lower state, one can easily reach a different state on the upper branch by using an addressing external pulse with moderate power. In this regime the intracavity pulse

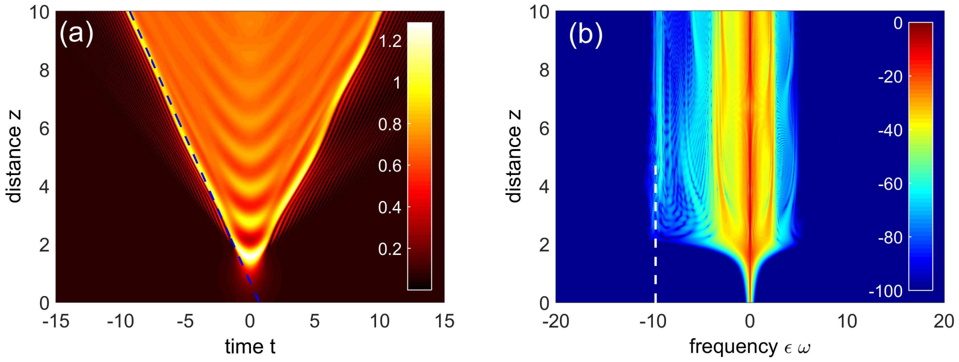

Figure 3.12 – Temporal (a) and spectral (b) evolution of a shock. Parameters: $\beta_2 = 1$, $\varepsilon = 0.1$, $\delta = \pi/6$, $\beta_3 = 0.25$ and $\alpha = 0.03$. Dashed blue line in (a) represents the front velocity $V_s = -1$; dashed line in (b) stands for the value of $\varepsilon\omega_{RR} = -9.6$ calculated from Eq. (3.20).

edges undergo initial steepening, which is mainly driven by the Kerr effect, tending to form shock waves. The strong gradient associated with the steepened fronts enhances the impact of GVD, which ends up inducing the formation of wavetrains that connect the two states of the front. An example is reported in Fig. 3.11, by using the injected field $S(t) = \sqrt{P} + \sqrt{P_p}\mathrm{sech}(t)$ with $P = 0.0041$ and $P_p = 0.16P$.
As shown for the conservative case in the previous Section, the presence of HOD may lead the shock to radiate [104]. We concentrate on the first relevant dispersive perturbation, i.e. third order dispersion (TOD $\beta_3 \neq 0$), but the scenario is qualitatively similar for others order of HOD. An example is shown in Fig. 3.12, for the same injected field used for the example reported Fig. 3.11. In the temporal domain the effect of TOD is to induce an asymmetry between the leading and trailing fronts. The most striking feature is visible in the spectral propagation shown Fig. 3.11(b), where an additional frequency component, well detached from the shock spectrum, is generated starting at a distance $z \approx 2$. The frequency of this radiation can be found by means of a perturbation approach [104], similar to those developed for the conservative case. If in the limit of small losses α, we find that the frequency of the RR must satisfy the following equation:

$$\left[\beta_3 \frac{(\varepsilon\omega)^3}{6} + \beta_2 \frac{(\varepsilon\omega)^2}{2} - V_s(\varepsilon\omega) - \delta\right] + 2P_{uH} = 0, \tag{3.20}$$

where P_{uH} is the power of the higher state of the front, propagating with velocity V_s where RR is shed. This equation is very similar to Eq. (3.17), but it contains the cavity detuning δ as an additional parameter.

3.6 Conclusions

We have reported the principal results of our studies of dispersive shock waves in optical fibers. We have outlined the mechanisms that rule the wave breaking and the dispersive regularization processes in the framework of the NLSE. We showed experimentally that the background of the pulses greatly enhances the visibility of a DSW. We mimicked the process of the breaking of a dam in an optical fiber, which has also permitted to experimentally test Whitham modulation theory. We have described the dispersive perturbation of DSWs in fibers and resonators. We have developed a theory to predict the frequency of the emitted dispersive waves and performed experiments in optical fibers.

3.6.1 Personal contribution and scientific production

I have initiated independently these works at PhLAM, with the support of the ANR project NoAWE which I coordinate since 2014. My contribution in these studies was to obtain the funding, to perform the theoretical and numerical analysis, to coordinate the experiments and to supervise the students. The overall outcomes of these activities are:

- 1 ANR project, call *Accueil de Chercheurs de Haut Niveau*
- 6 peer-reviewed papers (1 *Physical Review Letters*) [J4,J5,J11,J14,J37,J41]
- 3 international invited conferences [I2,I6,I18]
- 3 international conferences [C1,C10,C19]
- 4 book chapters [B1,B3,B4,B6]

CHAPTER 4

Interaction between solitons and dispersive waves

This Chapter resumes the principal results of our theoretical and experimental investigations on the interaction between solitons and dispersive waves in optical fibers. We have exploited fibers with an engineered dispersion profile along the propagation coordinate in order to control the characteristics of the linear and nonlinear waves involved in the processes. The analyzed phenomena encompass the annihilation of a soliton into a polycrhomatic dispersive wave, the trasformation of a dispersive wave into a soliton, the tunneling of a soliton through a potential barrier, the realization of an optical event horizon and the emission of multiple dispersive waves in a fiber with periodic dispersion.

4.1 Introduction

The concept of soliton, introduced by Zabusky and Kruskal fifty years ago [68], is one of the most impactful and influential discovery of the twentieth century that revolutionized the field of nonlinear physics. A soliton is a special wave that propagates without changing its shape and collides elastically with other wavepackets: it is so a very robust and stable entity. Initially introduced for Korteweg-de Vries equation, it has extended to several other systems (called integrable) [105], encompassing the nonlinear Schrödinger equation, which describes light pulses propagation in optical fibers. However, perturbations can break the integrability of these systems and can even spoil the conservation laws of solitons, leading to their creation and/or annihilation. In optical fibers, the integrability breaking of the NLSE can lead, for example, to inelastic collisions of orthogonally polarized solitons [106]. Other perturbations, such as intrinsic higher-order dispersion and nonlinearity of optical fibers, also break the integrability and give rise to additional phenomena such as the emission of a dispersive wave [95] or the soliton self-frequency shift (SSFS) [107]. Combined with these effects, optical fibers with axially-varying dispersion (periodic or not) may also constitute a source of perturbation for solitons. For instance, a single soliton can emit multiple DWs or polychromatic DWs [108], [109] as a result of the changing dispersion topography.
In this Chapter we report on a few processes which entail the transformation of solitons and their interplay with linear waves. We have exploited the flexibility given by topographic fibers,

where the group velocity dispersion can be engineered as desired, to control the interactions under consideration. We first describe the generation of a large-band dispersive wave resulting from the annihilation of a soliton, which enters a fiber section with normal dispersion. We then describe the transformation of a dispersive wave into a fundamental soliton by exploiting a suitable fiber taper, a process that we termed solitonization. We illustrate the tunnelling of a soliton trough a normal dispersion fiber section, which mimic a longitudinal potential barrier. We report the implementation of the analogue of an event horizon in an optical fiber, where the dispersive wave experiencing the horizon is emitted by the input soliton, which also represents the moving barrier. We end the Chapter by describing the emission of multiple dispersive waves by a nonlinear wave, either a soliton or a shock wave, in a fiber with a periodic modulation of group velocity dispersion.

4.2 Soliton annihilation

In this section we show that a soliton progressively going from anomalous to normal dispersion region becomes completely annihilated [110]. It is continuously converted into a polychromatic DW spanning over hundreds of nanometers. We consider the case where a fundamental soliton is excited by launching a transform limited pulse with a 130 fs FWHM duration around 950 nm, with a peak power of 110 W, in a specifically designed fiber. The fiber is uniform over the first 4.5 m and then it is tapered down so that both ZDWs [depicted by solid lines in Figs. 4.1(a) and (c)] decreases until they join each other at 6 m. After this point, the fiber has normal GVD all over the spectral range of interest here. The spectral dynamics, displayed in Figs. 4.1(a) and (c) for simulations and experiments respectively, show the initial propagation of a soliton until 5.5 m, where it crosses the second ZDW and thus enters the normal GVD region. At this point, an exremely strong spectral broadening occurs, indicating that the pulse experiences an enhanced nonlinear effect. In fact, as long as the soliton spectrum starts to cross the ZDW, the emission of a dispersive wave is initiated. Since the second ZDW keeps decreasing and crossing the soliton, there is a continuous emission of radiation into the dispersive wave. Because the GVD properties of the fiber continuously changes, the phase-matching relation [95] linking the soliton and the dispersive wave continuously changes too, resulting in the generation of a broad radiation termed polychromatic dispersive wave [109], [110]. The time domain evolution is reported in Fig. 4.1(b), where it can be seen that the significant spectral broadening occurring at around 6 m is accompanied by a strong temporal broadening, which is consistent with the generation of a dispersive, strongly chirped pulse. This was confirmed experimentally by recording autocorrelation traces before and after the tapered section. At 4.5 m [Fig. 4.1(e)], the pulse has a duration of 113 fs (blue markers) and is well fitted by a square hyperbolic secant function, in good agreement with the simulation result (red solid line), which confirms its solitonic nature. But soon after the tapered section, at 6.5 m, the autocorrelation trace is much longer and has a distorted profile, again in agreement with simulations. At this point, there is no clue of the presence of a soliton, which has therefore totally been annihilated into a polychromatic dispersive wave.

4.3 Solitonization of a dispersive wave

We have showed numerically and experimentally that a dispersive wave initially emitted from a soliton can be transformed itself into a fundamental soliton, a process that we termed solitonization [111]. This is achieved by using an axially varying fiber where the longitudinal evolution of dispersion is tailored to compress the initially dispersive wave into a femtosecond scale

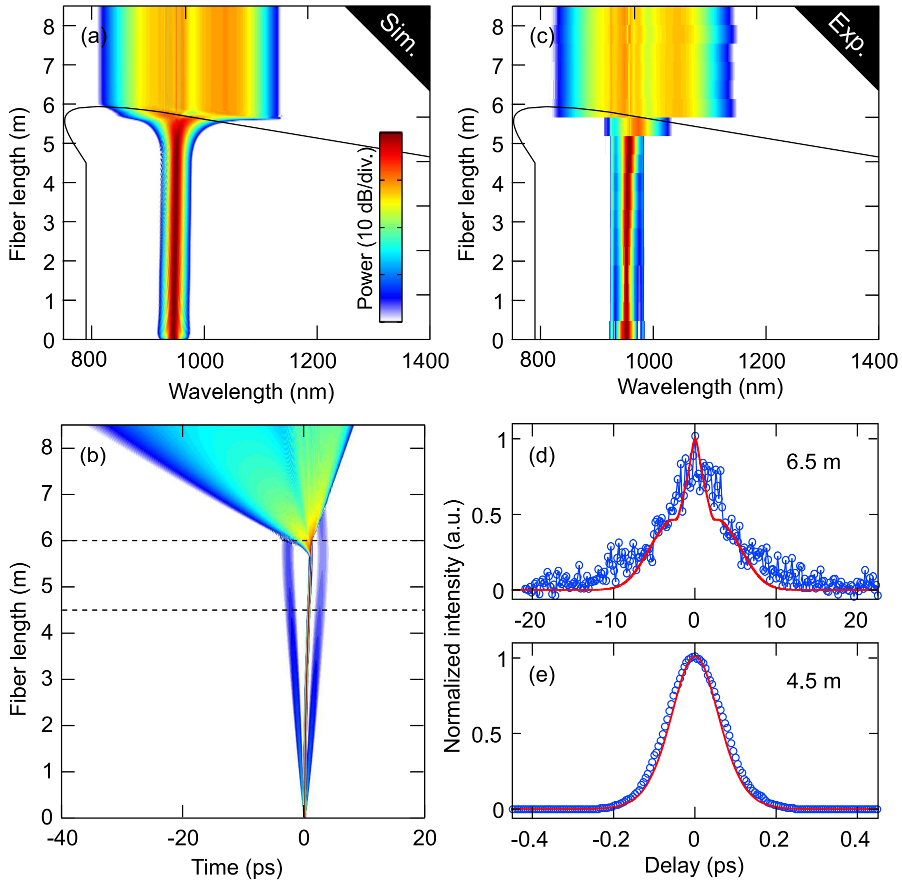

Figure 4.1 – (a,b) Numerical simulations and (c,d,e) experimental results showing the annihilation of a fundamental soliton into a polychromatic dispersive wave. (a) and (b) correspond respectively to the simulated spectral and temporal evolutions. (c) Measured spectral evolution versus fiber length. (d,e) Measured autocorrelation trace (open blue circles) and simulated ones (red solid line) at fiber length of (e) 4.5 m and (d) 6.5 m. Black solid lines in (a) and (c) depict the ZDWs. Dashed lines in (b) depict the limits of the tapered section.

pulse. We consider a soliton launched in the vicinity of the ZDW so that it emits a dispersive wave in the normal GVD region. Once the dispersive wave is emitted, the fiber parameters are changed so that the GVD at the dispersive wave wavelength becomes anomalous. The results are summarized in Fig. 4.2. The input pulse is transform limited with a 140 fs FWHM duration. It is centered around 881 nm and has a peak power of 42 W. The spectral evolution versus fiber length [simulations in Fig. 4.2(a) and experiments in Fig. 4.2(c)] shows the emission of a dispersive wave around 840 nm but does not highlight much change after the GVD change occurring between 5 and 7 m. The simulated time domain simulation of Fig. 4.2(b) provides much more information about the dynamics. The soliton decelerates due to the combined effects of spectral recoil and Raman-induced self-frequency shift and the dispersive wave, which starts spreading out, is located slightly behind it, as expected. Once it enters the tapered region (indicaded by the two dashed lines), the dispersive wave accelerates due to changing dispersion and crosses the soliton. At the same time, it recompresses and further propagates as a short pulse

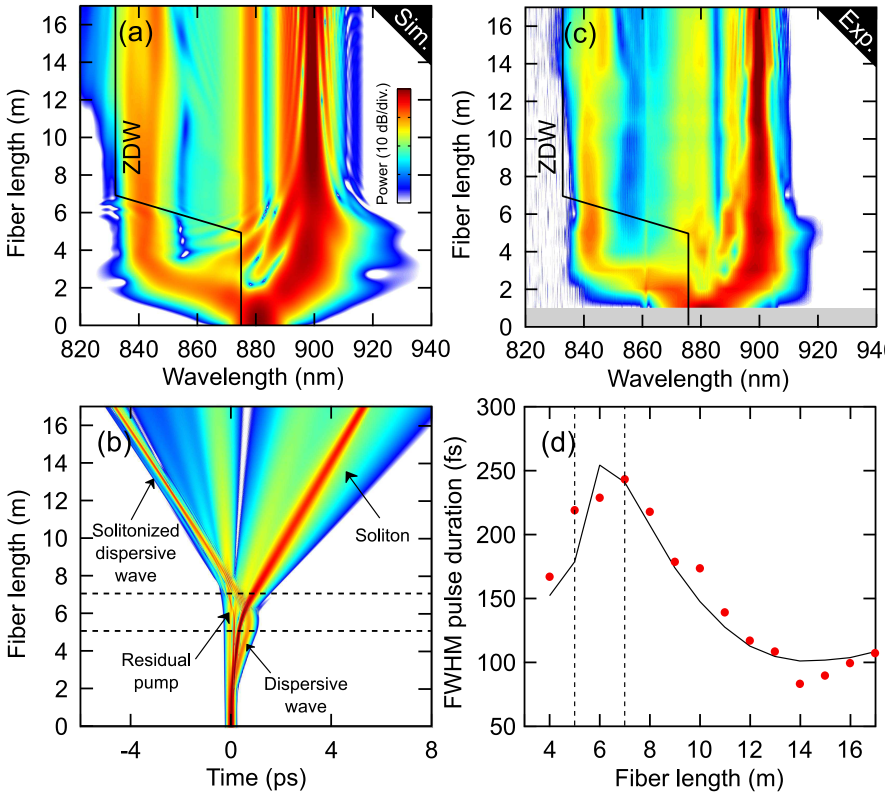

Figure 4.2 – (a,b) Numerical simulations and (c,d) experimental results showing the transformation of a dispersive wave into a fundamental soliton. (a) and (b) correspond respectively to the simulated spectral and temporal evolutions. (c) Measured spectral evolution versus fiber length. (d) Measured pulse duration around 840 nm (red full circles) and simulated one (black solid line). Black solid lines in (a) and (c) depict the ZDW. Dashed lines in (b) and (d) depict the limits of the tapered section.

in the remaining section of the fiber, recalling the behavior of a soliton. In fact, the solution of the direct Zakarov-Shabat scattering problem, reveals that the dispersive wave has indeed been transformed into a fundamental soliton [111] and propagates as such in the remaining anomalous dispersion region. Experimental autocorrelation measurements reported in Fig. 4.2(d) confirm this behavior: the pulse duration initially increases and then decreases after the tapered region, where they are perfectly fitted by square hyperbolic secant functions [111].

4.4 Soliton tunnelling

In this Section we report the observation of the longitudinal soliton tunneling effect [112], where a fundamental soliton, initially propagating in the anomalous dispersion region of a fiber, can pass through a normal dispersion barrier without being substantially affected. Figure 4.3(a) shows the simulated temporal profile along the propagation distance in the fiber, for an input pulse centered around 1485 nm (launched in anomalous GVD region), and a peak power P_{peak}

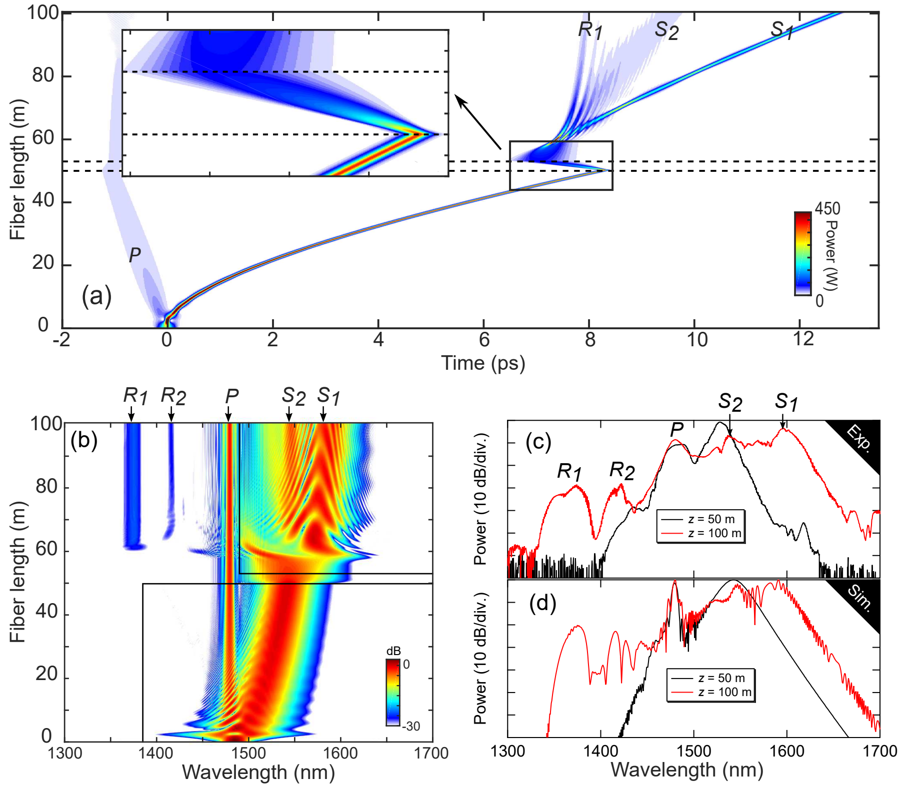

Figure 4.3 – (a) Simulated temporal profile against the fiber length. The dashed horizontal lines mark the normal GVD tunnel. (b) Simulated spectrum against the fiber length. The black line corresponds to the ZDW. (c) Experimental spectrum measurement at $z = 50$ m (black curve) and at the fiber output $z = 100$ m (red curve). (d) Corresponding numerical simulation. R_1, R_2, P, S_1, S_2 respectively stand for the different components of the output spectrum: radiation 1 and 2, pump residue, soliton 1 and 2.

of 240 W. At the initial stage, the soliton rapidly separates from the pump P and strongly decelerates due to SSFS, as observed in the spectral domain in Fig. 4.3(b). Inside the second fiber section, the pulse strongly broadens temporally due to normal GVD. Afterwards, the pulse enters the final anomalous dispersion fiber section, where it temporally recompresses and reshapes into a fundamental soliton, denoted as S_1 in the figure. A second weak pulse S_2 can be also observed around 9.5 ps at the end of the third fiber. Performing a simulation over a much longer distance of 200 m, we noticed that the S_2 pulse remains stable as a second (weak) soliton. A dispersive wave indicated as R_1 is observed from 60 m in Fig. 4.3(a). Figure 4.3(b) shows the corresponding simulated spectral dynamics. At the initial stage of propagation, we observe the generation of a fundamental soliton, which undergoes SSFS, and pump residues. In the second fiber section, where the GVD is normal, the pulse experiences strong dispersion and its peak power decreases, so that the Raman frequency shift rapidly stops. Afterwards, the pulse reaches the last fiber section at z = 53 m, where again propagation occurs in the anomalous GVD region. From about 60 m, we can identify the formation of two solitary pulses (labeled S_1 and S_2), which reach 1547 nm and 1590 nm at 100 m, respecively. Simultaneously, two small radiative waves are generated at 1375 nm and 1416 nm (R_1 and R_2), which satisfy the phase matching relation linking dispersive waves to solitons [95]. The solution of the direct Zakharov-Shabat scattering problem further confirms that S_1 and S_2 correspond to two different discrete eigenvalues, that is they are indeed solitons [112]. These results provide a theoretical evidence of the process of longitudinal soliton tunnelling, in which a soliton can tunnel through a potential barrier made of a short normal GDV fiber section. In order to study the soliton tunneling effect experimentally, we constructed a composite fiber by splicing three dispersion shifted fibers with length and ZDW corresponding to the parameters of the previous numerical simulations. The result is shown in Fig. 4.3(c), where we compare the experimental spectrum at the composite fiber output ($z = 100$ m, red line) with the spectrum measured at the input of the normal GVD section ($z = 50$ m, black line) after a cutback. In Fig. 4.3(c) we can clearly identify the incident soliton entering the normal GVD section at 1528 nm (black line), along with the two output solitons around 1536 nm (S_2) and 1597 nm (S_1) on the red curve. In the output spectrum, we also see the two dispersive waves (R_1 around 1365 nm and R_2 around 1420 nm) generated from the two solitons S_1 and S_2, in excellent agreement with the numerical simulations, reported in Fig. 4.2(d). In addition to these spectral measurements, we performed autocorrelation measurements after successive cutbacks of the fiber (not showed here see [112]), which confirmed the temporal behavior reported in Fig. 4.3(a).

4.5 Optical event horizons from the collision of a soliton and its own dispersive wave

Event horizons can be mimicked in optical fibers by the nonlinear interaction of a weak linear radiation (usually termed probe wave) with an intense copropagating soliton [113]. So-called fiber event horizons (FEHs) occur when the probe wave, travelling at a different group velocity with respect to the soliton, is unable to pass through it during their collision. The probe wave is therefore reflected onto the soliton which acts as a nonlinear barrier altering its group velocity. In the spectral domain, this results in the frequency conversion of the probe wave at ω_P into a reflected wave (RW) at $\omega = \omega_R$ that satisfies the phase-matching (PM) condition [114]:

$$D(\omega) = D(\omega_P), \tag{4.1}$$

where $D(\omega) = \beta(\omega) - \beta(\omega_S) - \beta_1 \times (\omega - \omega_S)$ denotes the wavenumber in a reference frame moving with the soliton, $\beta(\omega)$ is the fiber propagation constant and $\beta_1 = \partial_\omega \beta(\omega_S)$ is the group velocity at the soliton frequency ω_S. The analogy between event horizons and the nonlinear reflection of a weak probe onto a soliton has attracted much interest over the past few years and opens new perspectives in the control of light. We have shown experimentally that this process is actually very robust, as FEHs can be observed from the collision between a soliton and the dispersive wave emitted directly from this soliton at the early stage of propagation [115]. The soliton is excited by an ultrashort pulse and generates a phase-matched DW acting as the probe wave. The collision between the soliton and this DW is controlled by using a photonic crystal fiber (PCF) with a longitudinally varying dispersion landscape. The varying dispersion along the fiber enhances the deceleration of the soliton, reshapes the DW trajectory in the time domain and also modifies the PM condition Eq. (4.1) so that the DW collide with the soliton in the vicinity of its group velocity matching (GVM) wavelength.

FEHs can be rigorously described by means of the theory of the mixing between a soliton and a DW [114]. If we consider a probe whose frequency is near the group velocity matching frequency, which collides with a fundamental soliton, the reflection and transmission coefficients can be

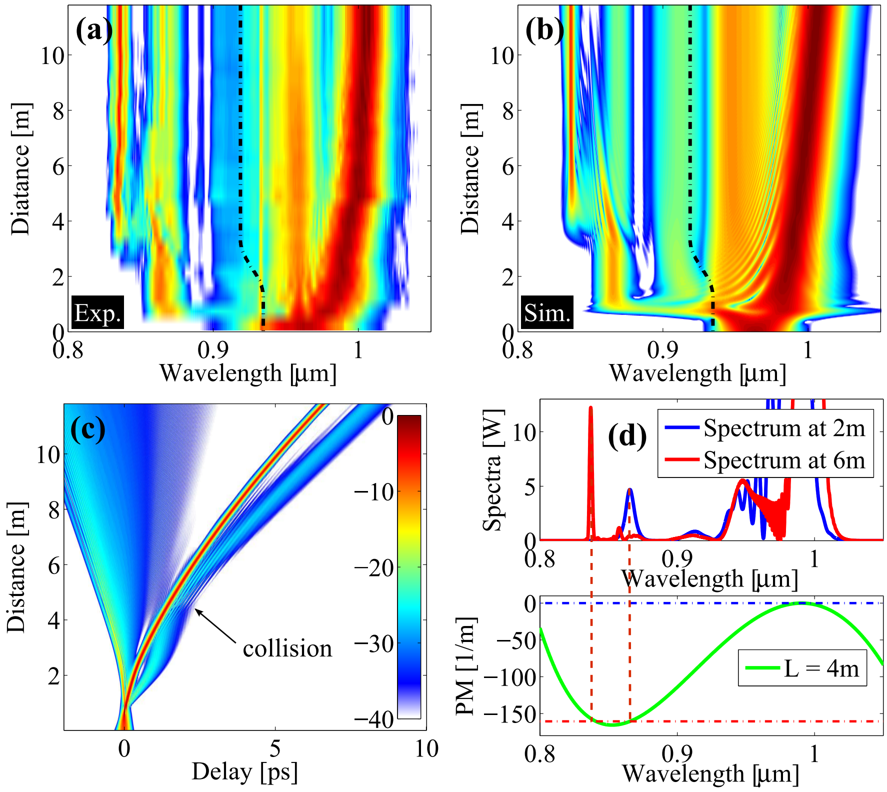

Figure 4.4 – Measured (a) and simulated (b) spectral dynamics illustrating a FEH with a pump peak power of 90 W. Black dashed lines depict the ZDW. (c) Simulated temporal dynamics. (d) Top: simulated spectra at fiber lengths of 2 m (blue line) and 6 m (red line), *i.e.* respectively before and after collision. Bottom: Graphical solution of phase-matching Eq. (4.1) at 4 m. Green curve, $D(\omega)$; horizontal dashed red line, $D(\omega_P)$.

calculated analytically as [115]

$$\rho(\Omega) = \frac{\cosh^2\left(\frac{\sqrt{15}}{2}\pi\right)}{\sinh^2(\pi\Omega T_0) + \cosh^2\left(\frac{\sqrt{15}}{2}\pi\right)}, \tag{4.2}$$

$$\tau(\Omega) = \frac{\sinh^2(\pi\Omega T_0)}{\sinh^2(\pi\Omega T_0) + \cosh^2\left(\frac{\sqrt{15}}{2}\pi\right)}. \tag{4.3}$$

Interestingly, with our approximations, the conversion efficiency ρ does not depend on β_2 for a fundamental soliton.

Figure 4.4(a) displays the experimental spectral dynamics for a pump peak power of 90 W. Corresponding numerical simulations are shown in Fig. 4.4(b) and 4.4(c) (respectively in the spectral and time domain). They were performed using a generalized nonlinear Schrödinger equation taking the full frequency dependance of the dispersion curve into account, as well as Kerr (including self-steepening) and Raman nonlinearities, with the parameters extracted from

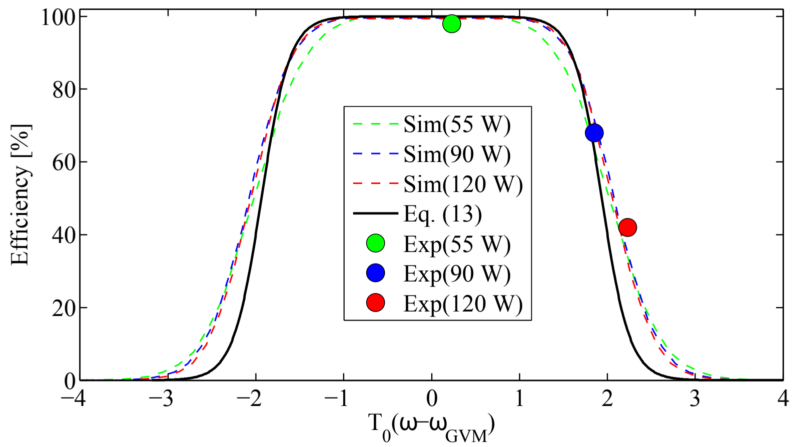

Figure 4.5 – Simulated conversion efficiencies into the idler wave versus probe wavelength, for pump powers of 55, 90 and 120 W (green, blue and red lines respectively). Markers are experimental data, assuming a soliton duration of 95, 68 and 53 fs. Thick black line is the analytically calculated conversion efficiency Eq. (4.2)

the experiment. The spectral dynamics is in excellent quantitative agreement with the cutback measurement of Fig. 4.4(a). The dynamics scenario is as follows. The pump pulse excites a fundamental soliton which first emits a DW at 865 nm within the first meter, due to its proximity to the input ZDW. The soliton then undergoes Raman effect, which results in its deceleration in the time domain (Fig. 4.4(c)). Then, the variation of the group velocity along the transition region makes the soliton further decelerate and simultaneously reshapes the DW trajectory in the time domain. This induces an inevitable collision between the soliton and the DW around 4 m (Fig. 4.4(c)). In the spectral domain, this results in the conversion of the DW into a RW centered at 837 nm according to the PM process described by Eq. (4.1). In our experiment, nearly 85% of the DW energy before collision (blue line in Fig. 4.4(d)) is converted into the RW after collision (red line in Fig. 4.4(d)). A remarkable reflection of the DW on the soliton is also apparent in the temporal domain, which is the signature of a FEH. The bottom curve of Fig. 4.4(d) confirms that the generated RW follows the PM relation of Eq. (4.1) involving the colliding DW and soliton.

We studied the conversion efficiency into the RW after collision with the soliton. Previous studies of FEHs using pump-probe configurations pointed out the role of the probe wavelength in the conversion efficiency into the idler wave [116]. In our case, the Raman soliton acts as the pump wave and the DW initially emitted from the soliton acts as the probe wave. Therefore, we first extracted all parameters of these two waves from numerical simulations, before the collision occurs. Then, we kept them constant except for the probe wavelength, which has been artificially tuned (which is equivalent to vary its group velocity relatively to the soliton) and studied the conversion efficiency into the RW after collision with the soliton. The results are reported in Fig. 4.5, where green, blue and red lines in show the simulated conversion efficiency versus probe wavelength obtained for 55 W, 90 W and 120 W input peak power, respectively. Markers in corresponding color are experimental conversion efficiencies extracted from measurements. The soliton duration T_0 has been calculated from the experimental spectra, assuming a transform-limited hyperbolic secant pulse. Note that a 100 % conversion efficiency is not reachable in this case, thus preventing the existence of an event horizon in strict sense. This is caused by the fact that soliton and DW located exactly at GVM wavelengths cannot collide. Around this point, the conversion efficiency decreases symmetrically to zero with increasing probe detuning.

Our experiments demonstrate that the conversion efficiency into the RW can be investigated by simply adjusting the input peak power in our experimental scheme, which is equivalent to tuning the probe wavelength in pump-probe configurations. In all cases, the simulated and measured conversion efficiencies are in remarkably good agreement with the analytical curve obtained using Eq. (4.2).

4.6 Emission of multiple dispersive waves in dispersion oscillatig fibers

In this Section we show theoretically and experimentally that a localized nonlinear wave can emit multiple resonant radiations in a dispersion oscillating fiber [117]. The nonlinear wave can be either a soliton, generated when pumping in the anomalous dispersion region, or a shock wave, generated when pumping in the normal dispersion region, as described in the previous Chapter.

Perturbation theory allows us to predict the frequency detunings ω_{RR} of the resonant radiations that can be excited in a DOF. They turn out to be given by the roots of the following expression:

$$\hat{D}(\omega_{RR}) - k_{nl} = \frac{2\pi}{\Lambda} m, \;\; m = 0, \pm 1, \pm 2, \ldots \tag{4.4}$$

where $\hat{D}(\omega) = -\Delta k_1 \omega + \beta_2 \omega^2/2 + \beta_3 \omega^3/6 + \ldots$ is the average linear dispersion in the pump reference frame. $\beta_3 \equiv d^3k/d\omega^3$ and Δk_1 arises from the deviation of the actual group-velocity from the natural one [91], [97]). In Eq. (4.4), k_{nl} is a well defined nonlinear wavenumber fixed by power. For a bright soliton $k_{nl} = \gamma P/2$, where P and γ are the soliton peak power and the fiber nonlinearity, whereas for a shock wave $k_{nl} = -\gamma P_b$, being P_b the power of the background field over which the RR propagates [91], [97]. Equation (4.4) expresses momentum conservation: it states that the difference between the momentum of the linear waves and the momentum generated by the nonlinear pump must be equal to the virtual momentum carried by the periodic modulation of the dispersion.

We verified that Eq. (4.4) describes accurately the parametric excitation of RR in both GVD regimes. A clear illustration of this phenomenon is provided in Fig. 4.6, which shows the simulated evolution of a hyperbolic secant pulse based on the NLSE with included periodic GVD and dispersion slope β_3. Figure 4.6(a) displays the time domain evolution of a pulse with $P = 15$ W, corresponding to a nearly fundamental soliton launched in a 150 m long DOF of period $\Lambda = 5$ m. Strong radiation traveling slower than the soliton becomes visible beyond the activation distance $z_a \sim 20$ m, corresponding to maximum pulse compression. In the spectral domain, the radiation modes correspond to several distinct and well defined frequencies [see Fig. 4.6(b,c)] that agree with the prediction based on Eq. (4.4) (vertical green lines). The peak detuned by ~ 9 THz from the pump turns out to be the standard RR [$m = 0$ in Eq. (4.4)], whereas other twelve peaks originate from the periodic perturbation [$m \neq 0$ in Eq. (4.4)].

When pumping in the normal GVD regime, we selected a higher peak power and duration ($P = 100\ W$, $280\ fs$) in order to access wave-breaking, and a shorter modulation period ($\Lambda = 0.5\ m$) in order to have resonances in a realistic frequency span. In this case, the localized state is the shock front that emerges over the pulse leading edge after the breaking and activation distance $z \sim 8$ m, which is clearly visible in Fig. 4.6(d). Also in this regime, we identify a first spectral peak at -15 THz in the anomalous GVD region [see Fig. 4.6(e,f)] as the standard RR ($m = 0$ mode) due to β_3, while other five peaks are clearly visible. These are parametrically excited resonant modes that correspond to $m = \pm 1, \pm 2, 3$, whose position are also well predicted by Eq.

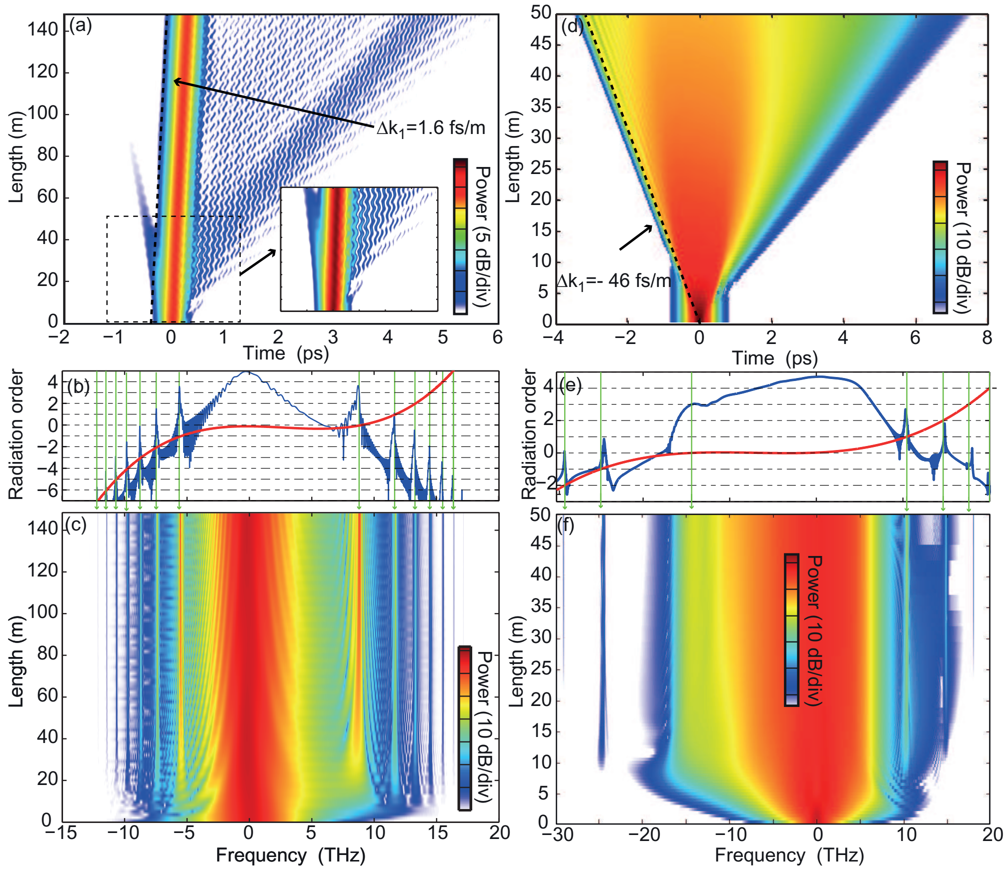

Figure 4.6 – Numerical simulation of a soliton (a-c) and a shock wave (d-f) emitting multiple resonant radiation. (a,d): colormap of the temporal evolution of power (log scale) along the fiber; (b,e): output spectra superimposed on the dispersion relation $\hat{D}(\omega) - k_{nl}$ (red curve). The vertical green lines correspond to the resonances determined by the graphical solution of Eq. (4.4); (c,f): colormap evolution of the spectrum along the fiber.

(4.4)(see vertical green lines).

We have designed two experiments in order to observe the parametrically excited resonances from both solitons and DSWs. In a first experiment, a 150 fs pulse centered at 1075 nm was launched in a 150 m-long DOF with a modulation period of 5 m. Figure 4.7(a) shows the longitudinal profile of the fiber diameter measured during the draw process (left axis) and the corresponding calculated zero dispersion wavelength (ZDW, right axis). An experimental power map, representing the output spectrum recorded for increasing pump peak power, is plotted in Fig. 4.7(b). It shows that, for increasing pump peak power, the spectrum rapidly evolves from a hyperbolic secant shape to a much more structured and highly asymmetric one containing more and more sharp spectral resonances. More precisely, these discrete spectral sidebands correspond to the parametric excitation of the RR that stems from the periodic variation of the second order dispersion. The experiments are well reproduced by numerical simulation and by the theory of Eq. (4.4) for all the values of the power. An example is detailed in Fig. 4.7(c) .

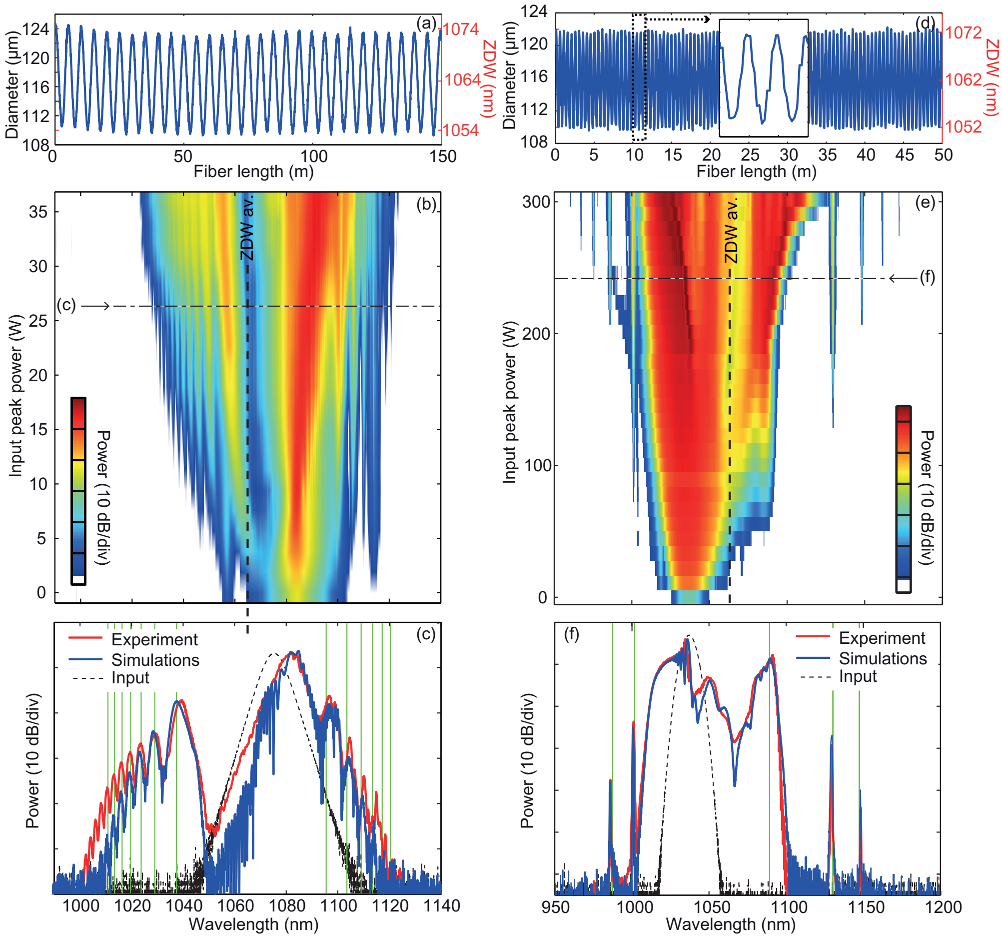

Figure 4.7 – Parametrically excited multiple resonances from a fundamental soliton (left panels) and from a DSW (right panels): experimental results. (a,d): Longitudinal evolution of the DOF diameter (left vertical axis) and consequent zero-dispersion wavelength (ZDW, right vertical axis) used for the soliton (a) and dispersive shock waves (d) experiments. (b,e): Experimental power maps showing the development of asymmetric sidebands with increasing pump peak power. (c,f): Comparison between experimental (red lines) and simulated spectra (blue lines) for a pump peak power of 26.4 W in the soliton case (c) and of 234 W in the dispersive shock wave case (f). Vertical green lines depict the resonance from Eq. (4.4).

The second experiment presented here is devoted to investigating radiating DSWs. The DOF is shorter (50 m) as well as the modulation period (0.5 m, see longitudinal profile in Fig. 4.7(d)). It has been pumped with 280 fs pulses. The pump wavelength was tuned to 1037 nm so that it lies in the normal average dispersion region required to generate a shock wave from a few hundreds of watts of peak power. Figure 4.7(e) shows the experimental power map. Starting at about 50 W, a RR peak is generated across the average zero dispersion wavelength. For increasing pump peak powers, additional discrete spectral sidebands corresponding to parametrically excited RR appear, similarly to the soliton case. These results are again in excellent agreement with

numerical simulations and with Eq. (4.4), as shown in Fig. 4.7(f).
To summarize, we have demonstrated that localized states (either a soliton or a dispersive shock wave) can efficiently emit multiple resonant radiations at different frequencies, as a result of the quasi-momentum associated to a DOF. Our experimental results are well supported by numerical simulations and by the perturbative analysis that leads to Eq. (4.4).

4.7 Conclusions

In this Chapter we reported the results of our theoretical and experimental investigations on the interaction between solitons and dispersive waves in optical fibers. We have exploited fibers with an engineered dispersion profile along the propagation coordinate in order to control the characteristics of the linear and nonlinear waves involved in the processes. We described the annihilation of a soliton into a polycrhomatic dispersive wave, the trasformation of a dispersive wave into a soliton, the tunneling of a soliton through a potential barrier, the realization of an optical event horizon and the emission of multiple dispersive waves in a fiber with periodic dispersion.

4.7.1 Personal contribution and scientific production

The study of nonlinear phenomena in topographic fibers was already well established at my arrival at PhLAM. I was able to insert in this research line by giving a deeper theoretical support. The synergy between the experimental facilities and know-how of the nonlinear photonics group and my theoretical expertise, has generated an important number of publications. The overall outcomes of these activities are:

- 11 peer-reviewed papers [J6,J12,J16,J18,J24,J25,J28,J29,J30,J33,J35]
- 1 international invited conference [I1]
- 5 international conferences [C2,C5,C6,C17,C18]
- 1 book chapter [B2]

Conclusions and Perspectives

This manuscript describes the principal research activities that I have conducted at Laboratoire de Physique de Laser, Atomes et Molécules since 2014.
The first subject discussed in this Thesis is modulation instability in dispersion oscillating fiber ring cavities. I started this study just after my arrival at PhLAM, by performing a theoretical investigation which predicted the existence of parametric instability in DOF cavities. In collaboration with Arnaud Mussot, we designed an experiment to confirm the analytic predictions. We found that there was enough work to develop an entire PhD thesis, so we hired François Copie under co-supervision (thesis defended on October 2017). We managed to implement the cavity and to observe the competition between Turing (classical MI) and Faraday (parametric MI) instabilities. This line of research is still active. We are focusing on the study of the roundtrip-to-roundtrip temporal dynamics, to the weak dispersion regime, to convective instabilities and to chaos. These aspect are the subject of the PhD of Florent Bessin, started in October 2016. Moreover, I have very recently developed a theoretical model, which extends the Lugiato-Lefever equation to regimes of high nonlinear phase shift, where states supported by different cavity resonances can exist and compete [J3]. This study is at the very beginning, and I expect that the new model can unveil novel phenomena paving the way to design additional experiments.
The second subject is the nonlinear stage of modulational instability in dispersion oscillating fibers. This work has been issued by the fruitful collaboration with the mathematicians of Laboratoire Painlevé (Stephan de Bièvre, Guillaume Dujardin, Simona Rota-Nodari), which I had the pleasure to conduct in the framework of LABEX CEMPI. During this work, I exploited my interdisciplinary profile, which made me the middle-person between the mathematicians and the experimenters. As a result, we published a first work reporting theory and experiments in fibers with a dispersion profile mimicking a train of Dirac impulses. We then obtained the theoretical results described in Chapter 2, and we are now concentrating on the corresponding experiments. Over the short term, we want to observe the predicted off-resonant parametric amplification in a dispersion oscillating fiber. On a longer timescale, we plan to observe Fermi-Pasta-Ulam recurrence and parametric-resonance breathers in DOFs. A complex set-up has been built in collaboration with Arnaud Mussot and Pascal Szriftgiser, in order to measure the spatial evolution of amplitude and phase of three spectral components (pump and MI sidebands) interacting non-linearly in the fibers.
The third subject is the development of dispersive shock waves in optical fibers. I gave several theoretical contributions in this field, in collaboration with Stefano Trillo, the most important being the prediction of emission of resonant radiation from shock waves. Shock waves are the core of the ANR project NoAWE (*Nonlinear Dynamics of Abnormal Wave Events*), started in 2014, of which I am the principal investigator. The achievement of an ANR project as coordinator is one of the most important step in my career, which allowed me to build and lead a research

group in full autonomy. In fact, the post-doc of Gang Xu, who performed the experiments on dam breaking and the PhD of Tomy Marest, who performed the experiments of dispersive wave emission from a dispersive shock, were both funded by NoAWE. Several works are under-progress in this area. We are studying other configurations of the Riemann problem, where the input condition is a step in both amplitude and instantaneous frequency. A post-doc will be hired soon in order to continue the works initiated by Gang Xu. In collaboration with Alexandre Kudlinski, we are also exploring shock waves in multimode fibers, from both a theoretical and experimental point of view. This rather unexplored area is the topic of the PhD thesis of Carlos Mas Arabi (co-supervision with Alexandre Kudlinski), funded by the ANR NoAWE.
The fourth subject is the interaction between dispersive waves and solitons in topographic fibers. I performed these studies in strict collaboration with Alexandre Kudlinski. Indeed, I started to work at PhLAM supported by a post-doc grant funded by the ANR project TOPWAVE (*Topographic optical fibers:new prospects in nonlinear guided-wave optics*) coordinated by Alexandre Kudlinski. We discovered and observed experimentally several processes entailing the interplay and transformation of solitons and dispersive waves in fibers presenting a dispersion profile evolving along the propagation coordinate. One of the first and most important results has been the theoretical prediction and experimental observation of emission of multiple resonant radiations in fibers with periodic dispersion. We are currently extending this concept to multi-mode fibers, where the periodic dispersion profile can compete with the self-imaging pattern generated by the interference of the propagating modes.

Bibliography

[1] V. E. Zakharov and L. A. Ostrovsky, "Modulation instability: The beginning", *Physica D: Nonlinear Phenomena*, vol. 238, p. 540, 2009.

[2] G. Van Simaeys, P. Emplit, and M. Haelterman, "Experimental Demonstration of the Fermi-Pasta-Ulam Recurrence in a Modulationally Unstable Optical Wave", *Physical Review Letters*, vol. 87, p. 033 902, 2001.

[3] ——, "Experimental study of the reversible behavior of modulational instability in optical fibers", *Journal of the Optical Society of America B*, vol. 19, p. 477, 2002.

[4] B. Kibler, J. Fatome, C. Finot, G. Millot, F. Dias, G. Genty, N. Akhmediev, and J. M. Dudley, "The Peregrine soliton in nonlinear fibre optics", *Nature Physics*, vol. 6, p. 790, 2010.

[5] B. Kibler, J. Fatome, C. Finot, G. Millot, G. Genty, B. Wetzel, N. Akhmediev, F. Dias, and J. M. Dudley, "Observation of Kuznetsov-Ma soliton dynamics in optical fibre", *Scientific Reports*, vol. 2, p. 463, 2012.

[6] J. M. Dudley, G. Genty, and S. Coen, "Supercontinuum generation in photonic crystal fiber", *Reviews of Modern Physics*, vol. 78, p. 1135, 2006.

[7] J. M. Dudley and J. Taylor, *Supercontinuum Generation in Optical Fibers*, 1st ed. Cambridge University Press, Apr. 2010.

[8] D. R. Solli, C. Ropers, P. Koonath, and B. Jalali, "Optical rogue waves", *Nature*, vol. 450, p. 1054, 2007.

[9] P. Del'Haye, A. Schliesser, O. Arcizet, T. Wilken, R. Holzwarth, and T. J. Kippenberg, "Optical frequency comb generation from a monolithic microresonator", *Nature*, vol. 450, p. 1214, 2017.

[10] T. Hansson, D. Modotto, and S. Wabnitz, "Dynamics of the modulational instability in microresonator frequency combs", *Physical Review A*, vol. 88, p. 023 819, 2013.

[11] K. Tai, A. Hasegawa, and A. Tomita, "Observation of modulational instability in optical fibers", *Physical Review Letters*, vol. 56, p. 135, 1986.

[12] M. E. Marhic, *Fiber Optical Parametric Amplifiers, Oscillators and Related Devices*, 1st ed. Cambridge University Press, 2007.

[13] J. Hansryd, P. A. Andrekson, M. Westlund, J. Li, and P.-O. Hedekvist, "Fiber-based optical parametric amplifiers and their applications", *IEEE Journal of Selected Topics in Quantum Electronics*, vol. 8, p. 506, 2002.

[14] C. Caucheteur, D. Bigourd, E. Hugonnot, P. Szriftgiser, A. Kudlinski, M. Gonzalez-Herraez, and A. Mussot, "Experimental demonstration of optical parametric chirped pulse amplification in optical fiber", *Optics Letters*, vol. 35, p. 1786, 2010.

[15] S. Radic, "Parametric signal processing", *IEEE Journal of Selected Topics in Quantum Electronics*, vol. 18, p. 670, 2012.

[16] A. M. Turing, "The Chemical Basis of Morphogenesis", *Philosophical Transactions of the Royal Society B: Biological Sciences*, vol. 237, p. 37, 1952.

[17] G.-L. Oppo, "Formation and control of Turing patterns and phase fronts in photonics and chemistry", *Journal of Mathematical Chemistry*, vol. 45, p. 95, 2009.

[18] J. K. Jang, M. Erkintalo, S. Coen, and S. G. Murdoch, "Temporal tweezing of light through the trapping and manipulation of temporal cavity solitons", *Nature Communications*, vol. 6, p. 7370, 2015.

[19] S. B. Papp, K. Beha, P. Del'Haye, F. Quinlan, H. Lee, K. J. Vahala, and S. A. Diddams, "Microresonator frequency comb optical clock", *Optica*, vol. 1, p. 10, 2014.

[20] V. Brasch, E. Lucas, J. D. Jost, M. Geiselmann, and T. J. Kippenberg, "Self-referenced photonic chip soliton Kerr frequency comb", *Light: Science & Applications*, vol. 6, e16202, 2017.

[21] M. Droques, A. Kudlinski, G. Bouwmans, G. Martinelli, and A. Mussot, "Experimental demonstration of modulation instability in an optical fiber with a periodic dispersion landscape", *Optics Letters*, vol. 37, p. 4832, 2012.

[22] F. Matera, A. Mecozzi, M. Romagnoli, and M. Settembre, "Sideband instability induced by periodic power variation in long-distance fiber links", *Optics Letters*, vol. 18, p. 1499, 1993.

[23] C. Finot, J. Fatome, A. Sysoliatin, A. Kosolapov, and S. Wabnitz, "Competing four-wave mixing processes in dispersion oscillating telecom fiber", *Optics Letters*, vol. 38, p. 5361, 2013.

[24] A. Armaroli and F. Biancalana, "Tunable modulational instability sidebands via parametric resonance in periodically tapered optical fibers", *Optics Express*, vol. 20, p. 25 096, 2012.

[25] M. Conforti, A. Mussot, A. Kudlinski, and S. Trillo, "Modulational instability in dispersion oscillating fiber ring cavities", *Optics letters*, vol. 39, p. 4200, 2014.

[26] K. Staliunas, C. Hang, and V. V. Konotop, "Parametric patterns in optical fiber ring nonlinear resonators", *Physical Review A*, vol. 88, p. 023 846, 2013.

[27] A. M. Perego, N. Tarasov, D. V. Churkin, S. K. Turitsyn, and K. Staliunas, "Pattern generation by dissipative parametric instability", *Physical Review Letters*, vol. 116, p. 028 701, 2016.

[28] A. H. Nayfeh and D. T. Mook, *Nonlinear oscillations*. Wiley, 1979.

[29] M. Faraday, "On a Peculiar Class of Acoustical Figures and on Certain Forms Assumed by Groups of Particles upon Vibrating Elastic Surfaces", *Philosophical Transactions of the Royal Society of London*, vol. 121, p. 299, 1831.

[30] F. Copie, M. Conforti, A. Kudlinski, A. Mussot, and S. Trillo, "Competing Turing and Faraday instabilities in longitudinally modulated passive resonators", *Physical Review Letters*, vol. 116, p. 143 901, 2016.

[31] F. Copie, M. Conforti, A. Kudlinski, S. Trillo, and A. Mussot, "Dynamics of Turing and Faraday instabilities in a longitudinally modulated fiber-ring cavity", *Optics Letters*, vol. 42, p. 435, 2017.

[32] L. A. Lugiato and R. Lefever, "Spatial Dissipative Structures in Passive Optical Systems", *Physical Review Letters*, vol. 58, p. 2209, 1987.

[33] M. Haelterman, S. Trillo, and S. Wabnitz, "Dissipative modulation instability in a nonlinear dispersive ring cavity", *Optics Communications*, vol. 91, p. 401, 1992.

[34] F. Copie, M. Conforti, A. Kudlinski, A. Mussot, F. Biancalana, and S. Trillo, "Instabilities in passive dispersion oscillating fiber ring cavities", *The European Physical Journal D*, vol. 71, p. 133, 2017.

[35] K. Ikeda and O. Akimoto, "Instability Leading to Periodic and Chaotic Self-Pulsations in a Bistable Optical Cavity", *Physical Review Letters*, vol. 48, p. 617, 1982.

[36] M. Conforti, F. Copie, A. Mussot, A. Kudlinski, and S. Trillo, "Parametric instabilities in modulated fiber ring cavities", *Optics Letters*, vol. 41, pp. 5027–5030, 2016.

[37] M. Haelterman, S. Trillo, and S. Wabnitz, "Additive-modulation-instability ring laser in the normal dispersion regime of a fiber", *Optics Letters*, vol. 17, p. 745, 1992.

[38] M. Anderson, Y. Wang, F. Leo, S. Coen, M. Erkintalo, and S. G Murdoch, "Coexistence of Multiple Nonlinear States in a Tristable Passive Kerr Resonator", *Physical Review X*, vol. 7, p. 031 031, 2017.

[39] M. Conforti and F. Biancalana, "Multi-resonant Lugiato–Lefever model", *Optics Letters*, vol. 42, p. 3666, 2017.

[40] S. Coen, M. Haelterman, P. Emplit, L. Delage, L. M. Simohamed, and F. Reynaud, "Bistable switching induced by modulational instability in a normally dispersive all-fibre ring cavity", *Journal of Optics B*, vol. 1, p. 36, 1999.

[41] S. Rota Nodari, M. Conforti, G. Dujardin, A. Kudlinski, A. Mussot, S. Trillo, and S. De Bièvre, "Modulational instability in dispersion-kicked optical fibers", *Physical Review A*, vol. 92, p. 013 810, 2015.

[42] X. Wang, D. Bigourd, A. Kudlinski, K. K. Y. Wong, M. Douay, L. Bigot, A. Lerouge, Y. Quiquempois, and A. Mussot, "Correlation between multiple modulation instability side lobes in dispersion oscillating fiber", *Optics Letters*, vol. 39, p. 1881, 2014.

[43] D. R. Solli, G. Herink, B. Jalali, and C. Ropers, "Fluctuations and correlations in modulation instability", *Nature Photonics*, vol. 6, p. 463, 2012.

[44] B. Wetzel, A. Stefani, L. Larger, P. A. Lacourt, J. M. Merolla, T. Sylvestre, A. Kudlinski, A. Mussot, G. Genty, F. Dias, and J. M. Dudley, "Real-time full bandwidth measurement of spectral noise in supercontinuum generation", *Scientific Reports*, vol. 2, p. 882, 2012.

[45] A. F. J. Runge, N. G. R. Broderick, and M. Erkintalo, "Dynamics of soliton explosions in passively mode-locked fiber lasers", *Journal of the Optical Society of America B*, vol. 33, p. 46, 2016.

[46] J. Hammer, P. Hosseini, C. R. Menyuk, P. S. J. Russell, and N. Y. Joly, "Single-shot reconstruction of spectral amplitude and phase in a fiber ring cavity at a 80 MHz repetition rate", *Optics Letters*, vol. 41, p. 4641, 2016.

[47] G. Herink, B. Jalali, C. Ropers, and D. R. Solli, "Resolving the build-up of femtosecond mode-locking with single-shot spectroscopy at 90 MHz frame rate", *Nature Photonics*, vol. 10, p. 321, 2016.

[48] K. Goda and B. Jalali, "Dispersive Fourier transformation for fast continuous single-shot measurements", *Nature Photon*, vol. 7, p. 102, 2013.

[49] L. Rayleigh, "XVII. On the maintenance of vibrations by forces of double frequency, and on the propagation of waves through a medium endowed with a periodic structure", *Philosophical Magazine Series 5*, vol. 24, p. 145, 1887.

[50] K. L. Turner, S. A. Miller, P. G. Hartwell, N. C. MacDonald, S. H. Strogatz, and S. G. Adams, "Five parametric resonances in a microelectromechanical system", *Nature*, vol. 396, p. 149, 1998.

[51] M. F. Yu, G. J. Wagner, R. S. Ruoff, and M. J. Dyer, "Realization of parametric resonances in a nanowire mechanical system with nanomanipulation inside a scanning electron microscope", *Physical Review B*, vol. 66, p. 073 406, 2002.

[52] R. Di Leonardo, G. Ruocco, J. Leach, M. J. Padgett, A. J. Wright, J. M. Girkin, D. R. Burnham, and D. McGloin, "Parametric Resonance of Optically Trapped Aerosols", *Physical Review Letters*, vol. 99, p. 010 601, 2007.

[53] F. Brau, H. Vandeparre, A. Sabbah, C. Poulard, A. Boudaoud, and P. Damman, "Multiple-length-scale elastic instability mimics parametric resonance of nonlinear oscillators", *Nature Physics*, vol. 7, p. 56, 2011.

[54] L. Salasnich, A. Parola, and L. Reatto, "Periodic quantum tunnelling and parametric resonance with cigar-shaped Bose-Einstein condensates", *Journal of Physics B: Atomic, Molecular and Optical Physics*, vol. 35, p. 315, 2002.

[55] K. Staliunas, S. Longhi, and G. J. de Valcárcel, "Faraday Patterns in Bose-Einstein Condensates", *Physical Review Letters*, vol. 89, p. 210 406, 2002.

[56] P. Engels, C. Atherton, and M. A. Hoefer, "Observation of Faraday Waves in a Bose-Einstein Condensate", *Physical Review Letters*, vol. 98, p. 095 301, 2007.

[57] N. J. Smith and N. J. Doran, "Modulational instabilities in fibers with periodic dispersion management", *Optics Letters*, vol. 21, p. 570, 1996.

[58] J. C. Bronski and J. N. Kutz, "Modulational stability of plane waves in nonreturn-to-zero communications systems with dispersion management", *Optics Letters*, vol. 21, p. 937, 1996.

[59] J. J. García-Ripoll, V. M. Pérez-García, and P. Torres, "Extended Parametric Resonances in Nonlinear Schrödinger Systems", *Physical Review Letters*, vol. 83, p. 1715, 1999.

[60] M. Droques, A. Kudlinski, G. Bouwmans, G. Martinelli, and A. Mussot, "Dynamics of the modulation instability spectrum in optical fibers with oscillating dispersion", *Physical Review A*, vol. 87, p. 013 813, 2013.

[61] N. N. Akhmediev, V. M. Eleonskii, and N. E. Kulagin, "Exact first-order solutions of the nonlinear Schrodinger equation", *Theoretical and Mathematical Physics*, vol. 72, p. 809, 1987.

[62] S. Trillo and S. Wabnitz, "Dynamics of the nonlinear modulational instability in optical fibers", *Optics Letters*, vol. 16, p. 986, 1991.

[63] C. B. Clausen, O. Bang, and Y. S. Kivshar, "Spatial Solitons and Induced Kerr Effects in Quasi-Phase-Matched Quadratic Media", *Physical Review Letters*, vol. 78, p. 4749, 1997.

[64] G. El and M. Hoefer, "Dispersive shock waves and modulation theory", *Physica D: Nonlinear Phenomena*, vol. 333, p. 11, 2016.

[65] G. B. Whitham, *Linear and Nonlinear Waves*. John Wiley & Sons, Inc., 1999.

[66] S. S. Moiseev and R. Z. Sagdeev, “Collisionless shock waves in a plasma in a weak magnetic field”, *Journal of Nuclear Energy. Part C, Plasma Physics, Accelerators, Thermonuclear Research*, vol. 5, p. 43, 1963.

[67] R. J. Taylor, D. R. Baker, and H. Ikezi, “Observation of Collisionless Electrostatic Shocks”, *Physical Review Letters*, vol. 24, p. 206, 1970.

[68] N. J. Zabusky and M. D. Kruskal, “Interaction of "Solitons" in a Collisionless Plasma and the Recurrence of Initial States”, *Physical Review Letters*, vol. 15, p. 240, 1965.

[69] A. V. Gurevich and L. P. Pitaevskii, “Nonstationary structure of a collisionless shock wave”, *Journal of Experimental and Theoretical Physics*, vol. 65, p. 291, 1974.

[70] G. B. Whitham, “Non-Linear Dispersive Waves”, *Proceedings of the Royal Society A: Mathematical, Physical and Engineering Sciences*, vol. 283, no. 1393, p. 238, 1965.

[71] A. V. Gurevich and A. L. Krylov, “Dissipationless Shock Waves in Media with Positive Dispersion”, *Journal of Experimental and Theoretical Physics*, vol. 65, p. 944, 1987.

[72] G. A. El, V. V. Geogjaev, A. V. Gurevich, and A. L. Krylov, “Decay of an initial discontinuity in the defocusing NLS hydrodynamics”, *Physica D: Nonlinear Phenomena*, vol. 87, p. 186, 1995.

[73] T. B. Benjamin and M. J. Lighthill, “On Cnoidal Waves and Bores”, *Proceedings of the Royal Society A: Mathematical, Physical and Engineering Sciences*, vol. 224, p. 448, 1954.

[74] D. H. Peregrine, “Calculations of the development of an undular bore”, *Journal of Fluid Mechanics*, vol. 25, p. 321, 1966.

[75] R. S. Johnson, “Shallow Water Waves on a Viscous Fluid—The Undular Bore”, *Physics of Fluids*, vol. 15, p. 1693, 1972.

[76] N. J. Zabusky and C. J. Galvin, “Shallow-water waves, the Korteweg-deVries equation and solitons”, *Journal of Fluid Mechanics*, vol. 47, p. 811, 1971.

[77] J. L. Hammack and H. Segur, “The Korteweg-de Vries equation and water waves. Part 2. Comparison with experiments”, *Journal of Fluid Mechanics*, vol. 65, p. 289, 1974.

[78] J. L. Hammack, “A note on tsunamis: their generation and propagation in an ocean of uniform depth”, *Journal of Fluid Mechanics*, vol. 60, p. 769, 1973.

[79] W. J. Tomlinson, R. H. Stolen, and A. M. Johnson, “Optical wave breaking of pulses in nonlinear optical fibers”, *Optics Letters*, vol. 10, p. 457, 1985.

[80] D. Anderson, M. Desaix, M. Lisak, and M. L. Quiroga–Teixeiro, “Wave breaking in nonlinear-optical fibers”, *Journal of the Optical Society of America B*, vol. 9, p. 1358, 1992.

[81] J. E. Rothenberg and D. Grischkowsky, “Observation of the formation of an optical intensity shock and wave breaking in the nonlinear propagation of pulses in optical fibers”, *Physical Review Letters*, vol. 62, p. 531, 1989.

[82] M. A. Hoefer, M. J. Ablowitz, I. Coddington, E. A. Cornell, P. Engels, and V. Schweikhard, “Dispersive and classical shock waves in Bose-Einstein condensates and gas dynamics”, *Physical Review A*, vol. 74, p. 023 623, 2006.

[83] N. Ghofraniha, C. Conti, G. Ruocco, and S. Trillo, “Shocks in Nonlocal Media”, *Physical Review Letters*, vol. 99, p. 043 903, 2007.

[84] C. Conti, A. Fratalocchi, M. Peccianti, G. Ruocco, and S. Trillo, “Observation of a Gradient Catastrophe Generating Solitons”, *Physical Review Letters*, vol. 102, p. 083 902, 2009.

[85] J. Fatome, C. Finot, G. Millot, A. Armaroli, and S. Trillo, "Observation of Optical Undular Bores in Multiple Four-Wave Mixing", *Physical Review X*, vol. 4, p. 021 022, 2014.

[86] S. Trillo, M. Klein, G. Clauss, and M. Onorato, "Observation of dispersive shock waves developing from initial depressions in shallow water", *Physica D: Nonlinear Phenomena*, vol. 333, p. 276, 2016.

[87] G. Xu, A. Mussot, A. Kudlinski, S. Trillo, F. Copie, and M. Conforti, "Shock wave generation triggered by a weak background in optical fibers", *Optics Letters*, vol. 41, p. 2656, 2016.

[88] G. Xu, M. Conforti, A. Kudlinski, A. Mussot, and S. Trillo, "Dispersive Dam-Break Flow of a Photon Fluid", *Physical Review Letters*, vol. 118, p. 254 101, 2017.

[89] A. Parriaux, M. Conforti, A. Bendahmane, J. Fatome, C. Finot, S. Trillo, N. Picqué, and G. Millot, "Spectral broadening of picosecond pulses forming dispersive shock waves in optical fibers", *Optics Letters*, vol. 42, p. 3044, 2017.

[90] R. J. LeVeque, *Finite Volume Methods for Hyperbolic Problems*. Cambridge: Cambridge University Press, 2002.

[91] M. Conforti, F. Baronio, and S. Trillo, "Resonant radiation shed by dispersive shock waves", *Physical Review A*, vol. 89, p. 013 807, 2014.

[92] W. Wan, S. Jia, and J. W. Fleischer, "Dispersive superfluid-like shock waves in nonlinear optics", *Nature Physics*, vol. 3, p. 46, 2007.

[93] G. Millot, S. Pitois, M. Yan, T. Hovhannisyan, A. Bendahmane, T. W. Hänsch, and N. Picqué, "Frequency-agile dual-comb spectroscopy", *Nature Photonics*, vol. 10, p. 27, 2015.

[94] Y. Kodama and S. Wabnitz, "Analytical theory of guiding-center nonreturn-to-zero and return-to-zero signal transmission in normally dispersive nonlinear optical fibers", *Optics Letters*, vol. 20, p. 2291, 1995.

[95] N. Akhmediev and M. Karlsson, "Cherenkov radiation emitted by solitons in optical fibers", *Physical Review A*, vol. 51, p. 2602, 1995.

[96] K. E. Webb, Y. Q. Xu, M. Erkintalo, and S. G. Murdoch, "Generalized dispersive wave emission in nonlinear fiber optics", *Optics Letters*, vol. 38, p. 151, 2013.

[97] M. Conforti and S. Trillo, "Dispersive wave emission from wave breaking", *Optics Letters*, vol. 38, p. 3815, 2013.

[98] G. P. Agrawal, *Nonlinear Fiber Optics*. Academic Press, 2006.

[99] S. Trillo and A. Valiani, "Hydrodynamic instability of multiple four-wave mixing", *Optics Letters*, vol. 35, p. 3967, 2010.

[100] M. Conforti and S. Trillo, "Radiative effects driven by shock waves in cavity-less four-wave mixing combs", *Optics Letters*, vol. 39, p. 5760, 2014.

[101] T. Marest, C. Mas Arabí, M. Conforti, A. Mussot, C. Milián, D. V. Skryabin, and A. Kudlinski, "Emission of dispersive waves from a train of dark solitons in optical fibers", *Optics Letters*, vol. 41, p. 2454, 2016.

[102] J. E. Rothenberg and H. K. Heinrich, "Observation of the formation of dark-soliton trains in optical fibers", *Optics Letters*, vol. 17, p. 261, 1992.

[103] S. Malaguti, G. Bellanca, and S. Trillo, "Dispersive wave-breaking in coherently driven passive cavities", *Optics Letters*, vol. 39, p. 2475, 2014.

[104] S. Malaguti, M. Conforti, and S. Trillo, "Dispersive radiation induced by shock waves in passive resonators", *Optics Letters*, vol. 39, p. 5626, 2014.

[105] M. A. Ablowitz and P. A. Clarkson, *Solitons, Nonlinear Evolution Equations and Inverse Scattering*. Cambridge: Cambridge University Press, 1991, vol. 149.

[106] B. A. Malomed and S. Wabnitz, "Soliton annihilation and fusion from resonant inelastic collisions in birefringent optical fibers", *Optics Letters*, vol. 16, p. 1388, 1991.

[107] F. M. Mitschke and L. F. Mollenauer, "Discovery of the soliton self-frequency shift", *Optics Letters*, vol. 11, p. 659, 1986.

[108] A. Bendahmane, F. Braud, M. Conforti, B. Barviau, A. Mussot, and A. Kudlinski, "Dynamics of cascaded resonant radiations in a dispersion-varying optical fiber", *Optica*, vol. 1, p. 243, 2014.

[109] C. Milián, A. Ferrando, and D. V. Skryabin, "Polychromatic Cherenkov radiation and supercontinuum in tapered optical fibers", *Journal of the Optical Society of America B*, vol. 29, p. 589, 2012.

[110] A. Kudlinski, S. F. Wang, A. Mussot, and M. Conforti, "Soliton annihilation into a polychromatic dispersive wave", *Optics Letters*, vol. 40, p. 2142, 2015.

[111] F. Braud, M. Conforti, A. Cassez, A. Mussot, and A. Kudlinski, "Solitonization of a dispersive wave", *Optics Letters*, vol. 41, p. 1412, 2016.

[112] T. Marest, F. Braud, M. Conforti, S. Wabnitz, A. Mussot, and A. Kudlinski, "Longitudinal soliton tunneling in optical fiber", *Optics Letters*, vol. 42, p. 2350, 2017.

[113] T. G. Philbin, C. Kuklewicz, S. Robertson, S. Hill, F. König, and U. Leonhardt, "Fiber-Optical Analog of the Event Horizon", *Science*, vol. 319, p. 1367, 2008.

[114] D. V. Skryabin and A. V. Gorbach, "Colloquium : Looking at a soliton through the prism of optical supercontinuum", *Reviews of Modern Physics*, vol. 82, p. 1287, 2010.

[115] S. F. Wang, A. Mussot, M. Conforti, A. Bendahmane, X. L. Zeng, and A. Kudlinski, "Optical event horizons from the collision of a soliton and its own dispersive wave", *Physical Review A*, vol. 92, p. 023 837, 2015.

[116] G. Genty, J. M. Dudley, and M. Erkintalo, "Do optical event horizons really exist? The physics of nonlinear reflection at a soliton boundary", in *Advanced Photonics Congress (2012), paper NW3D.2*, Optical Society of America, 2012, NW3D.2.

[117] M. Conforti, S. Trillo, A. Mussot, and A. Kudlinski, "Parametric excitation of multiple resonant radiations from localized wavepackets", *Scientific Reports*, vol. 5, p. 9433, 2015.

APPENDIX A

Publication list

A.1 Peer-reviewed papers in international journals (95)

J1. M. Conforti, C. Mas Arabi, A. Mussot, and A. Kudlinski, "Fast and accurate modelling of nonlinear pulse propagation in graded-index multimode fibers," Opt. Lett. 42, 4004 (2017)

J2. A. Mussot, M. Conforti, S. Trillo, F. Copie, and A. Kudlinski, "Modulational instability in dispersion oscillating fibers," Adv. Opt. Phot. (to appear)

J3. M. Conforti and F. Biancalana, "Multi-resonant Lugiato-Lefever model," Opt. Lett. 42, 3666 (2017).

J4. A. Parriaux, M. Conforti, A. Bendahmane, J. Fatome, C. Finot, S. Trillo, N. Picqué, and G. Millot, "Spectral broadening of picosecond pulses forming dispersive shock waves in optical fibers," Opt. Lett. 42, 3044 (2017).

J5. G. Xu, M. Conforti, A. Kudlinski, A. Mussot, and S. Trillo, "Dispersive Dam-Break Flow of a Photon Fluid," Phys. Rev. Lett. 118, 254101 (2017).

J6. T. Marest, F. Braud, M. Conforti, S. Wabnitz, A. Mussot, and A. Kudlinski, "Longitudinal soliton tunneling in optical fiber," Opt. Lett. 42, 2350 (2017).

J7. F. Copie, M. Conforti, A. Kudlinski, A. Mussot, F. Biancalana, and S. Trillo, "Instabilities in passive dispersion oscillating fiber ring cavities," Eur. Phys. J. D 71, 133 (2017).

J8. F. Copie, M. Conforti, A. Kudlinski, S. Trillo, and A. Mussot, "Modulation instability in the weak dispersion regime of a dispersion modulated passive fiber-ring cavity," Opt. Express 25, 11283 (2017).

J9. F. Copie, M. Conforti, A. Kudlinski, S. Trillo, and A. Mussot, "Dynamics of Turing and Faraday instabilities in a longitudinally modulated fiber-ring cavity," Opt. Lett. 42, 435 (2017).

J10. M. Conforti, A. Mussot, A. Kudlinski, S. Rota Nodari, G. Dujardin, S. De Biévre, A. Armaroli, and S. Trillo, "Heteroclinic Structure of Parametric Resonance in the Nonlinear Schrödinger Equation," Phys. Rev. Lett. 117, 13901 (2016).

J11. G. Xu, A. Mussot, A. Kudlinski, S. Trillo, F. Copie, and M. Conforti, "Shock wave generation triggered by a weak background in optical fibers," Opt. Lett. 41, 2656 (2016).

J12. C. Mas Arabi, F. Bessin, A. Kudlinski, A. Mussot, D. Skryabin, and M. Conforti, "Efficiency of four-wave mixing between orthogonally polarized linear waves and solitons in a birefringent fiber," Phys. Rev. A 94, 63847 (2016).

J13. B. Frisquet, B. Kibler, P. Morin, F. Baronio, M. Conforti, G. Millot, and S. Wabnitz, "Optical Dark Rogue Wave," Sci. Rep. 6, 20785 (2016).

J14. T. Marest, C. Mas Arabi, M. Conforti, A. Mussot, C. Milián, D. V. Skryabin, and A. Kudlinski, "Emission of dispersive waves from a train of dark solitons in optical fibers," Opt. Lett. 41, (2016).

J15. M. Conforti, F. Copie, A. Mussot, A. Kudlinski, and S. Trillo, "Parametric instabilities in modulated fiber ring cavities," Opt. Lett. 41, 5027 (2016).

J16. F. Braud, M. Conforti, A. Cassez, A. Mussot, and A. Kudlinski, "Solitonization of a dispersive wave," Opt. Lett. 41, 1412 (2016).

J17. F. Copie, M. Conforti, A. Kudlinski, A. Mussot, and S. Trillo, "Competing Turing and Faraday Instabilities in Longitudinally Modulated Passive Resonators," Phys. Rev. Lett. 116, 143901 (2016).

J18. M. Conforti, S. Trillo, A. Kudlinski, and A. Mussot, "Multiple QPM Resonant Radiations Induced by MI in Dispersion Oscillating Fibers," IEEE Photonics Technol. Lett. 28, 740 (2016).

J19. M. Conforti, A. Mussot, J. Fatome, A. Picozzi, S. Pitois, C. Finot, M. Haelterman, B. Kibler, C. Michel, and G. Millot, "Turbulent dynamics of an incoherently pumped passive optical fiber cavity: Quasisolitons, dispersive waves, and extreme events," Phys. Rev. A 91, 023823 (2015).

J20. B. Frisquet, B. Kibler, J. Fatome, P. Morin, F. Baronio, M. Conforti, G. Millot, and S. Wabnitz, "Polarization modulation instability in a Manakov fiber system," Phys. Rev. A 92, 53854 (2015).

J21. S. R. Nodari, M. Conforti, G. Dujardin, A. Kudlinski, A. Mussot, S. Trillo, and S. De Bièvre, "Modulational instability in dispersion-kicked optical fibers," Phys. Rev. A 92, 13810 (2015).

J22. A. Bendahmane, A. Mussot, A. Kudlinski, P. Szriftgiser, M. Conforti, S. Wabnitz, and S. Trillo, "Optimal frequency conversion in the nonlinear stage of modulation instability," Opt. Express 23, 30861 (2015).

J23. S. Chen, F. Baronio, J. M. Soto-Crespo, P. Grelu, M. Conforti, and S. Wabnitz, "Optical rogue waves in parametric three-wave mixing and coherent stimulated scattering," Phys. Rev. A 92, 33847 (2015).

J24. S. F. Wang, A. Mussot, M. Conforti, A. Bendahmane, X. L. Zeng, and A. Kudlinski, "Optical event horizons from the collision of a soliton and its own dispersive wave," Phys. Rev. A 92, 23837 (2015).

J25. S. F. Wang, A. Mussot, M. Conforti, X. L. Zeng, and A. Kudlinski, "Bouncing of a dispersive wave in a solitonic cage," Opt. Lett. 40, 3320 (2015).

J26. F. Copie, A. Kudlinski, M. Conforti, G. Martinelli, and A. Mussot, "Modulation instability in amplitude modulated dispersion oscillating fibers," Opt. Express 23, 3869 (2015).

J27. F. Baronio, S. Chen, P. Grelu, S. Wabnitz, and M. Conforti, "Baseband modulation instability as the origin of rogue waves," Phys. Rev. A 91, 33804 (2015).

J28. A. Kudlinski, S. F. Wang, A. Mussot, and M. Conforti, "Soliton annihilation into a polychromatic dispersive wave," Opt. Lett. 40, 2142 (2015).

J29. A. Bendahmane, A. Mussot, M. Conforti, and A. Kudlinski, "Observation of the stepwise blue shift of a dispersive wave preceding its trapping by a soliton," Opt. Express 23, 16595 (2015).

J30. M. Conforti, S. Trillo, A. Mussot, and A. Kudlinski, "Parametric excitation of multiple resonant radiations from localized wavepackets," Sci. Rep. 5, 9433 (2015).

J31. S. Dal Conte, M. Conforti, D. Petti, E. Albisetti, S. Longhi, R. Bertacco, C. De Angelis, G. Cerullo, and G. Della Valle, "Disentangling electrons and lattice nonlinear optical response in metal-dielectric Bragg filters," Phys. Rev. B 89, 125122 (2014).

J32. K. Krupa, F. Baronio, M. Conforti, S. Trillo, A. Tonello, and V. Couderc, "Zero focusing via competing nonlinearities in beta-barium-borate crystals," Opt. Lett. 39, 925 (2014).

J33. M. Billet, F. Braud, A. Bendahmane, M. Conforti, A. Mussot, and A. Kudlinski, "Emission of multiple dispersive waves from a single Raman-shifting soliton in an axially-varying optical fiber," Opt. Express 22, 25673 (2014).

J34. F. Baronio, M. Conforti, A. Degasperis, S. Lombardo, M. Onorato, and S. Wabnitz, "Vector Rogue Waves and Baseband Modulation Instability in the Defocusing Regime," Phys. Rev. Lett. 113, 34101 (2014).

J35. A. Bendahmane, F. Braud, M. Conforti, B. Barviau, A. Mussot, and A. Kudlinski, "Dynamics of cascaded resonant radiations in a dispersion-varying optical fiber," Optica 1, 243 (2014).

J36. M. Conforti, F. Baronio, M. Levenius, and K. Gallo, "Broadband parametric processes in $\chi^{(2)}$ nonlinear photonic crystals," Opt. Lett. 39, 3457 (2014).

J37. S. Malaguti, M. Conforti, and S. Trillo, "Dispersive radiation induced by shock waves in passive resonators," Opt. Lett. 39, 5626 (2014).

J38. G. Xu, J. Garnier, M. Conforti, and A. Picozzi, "Generalized description of spectral incoherent solitons," Opt. Lett. 39, 4192 (2014).

J39. M. Conforti, A. Mussot, A. Kudlinski, and S. Trillo, "Modulational instability in dispersion oscillating fiber ring cavities," Opt. Lett. 39, 4200 (2014).

J40. M. Conforti, F. Baronio, and S. Trillo, "Resonant radiation shed by dispersive shock waves," Phys. Rev. A 89, 13807 (2014).

J41. M. Conforti and S. Trillo, "Radiative effects driven by shock waves in cavity-less four-wave mixing combs," Opt. Lett. 39, 5760 (2014).

J42. M. Conforti, "Exact cascading nonlinearity in quasi-phase-matched quadratic media," Opt. Lett. 39, 2427 (2014).

J43. G. Della Valle, F. Scotognella, A. R. S. Kandada, M. Zavelani-Rossi, H. Li, M. Conforti, S. Longhi, L. Manna, G. Lanzani, and F. Tassone, "Ultrafast Optical Mapping of Nonlinear Plasmon Dynamics in Cu 2–x Se Nanoparticles," J. Phys. Chem. Lett. 4, 3337 (2013).

J44. A. Marini, M. Conforti, G. Della Valle, H. W. Lee, T. X. Tran, W. Chang, M. A. Schmidt, S. Longhi, P. St J Russell, and F. Biancalana, "Ultrafast nonlinear dynamics of surface plasmon polaritons in gold nanowires due to the intrinsic nonlinearity of metals," New J. Phys. 15, 13033 (2013).

J45. J. Krauth, A. Steinmann, R. Hegenbarth, M. Conforti, and H. Giessen, "Broadly tunable femtosecond near- and mid-IR source by direct pumping of an OPA with a 417 MHz Yb:KGW oscillator," Opt. Express 21, 11516 (2013).

J46. M. Conforti, N. Westerberg, F. Baronio, S. Trillo, and D. Faccio, "Negative-frequency dispersive wave generation in quadratic media," Phys. Rev. A 88, 13829 (2013).

J47. M. Conforti, A. Marini, T. X. Tran, D. Faccio, and F. Biancalana, "Interaction between optical fields and their conjugates in nonlinear media," Opt. Express 21, 31239 (2013).

J48. M. Conforti, F. Baronio, and S. Trillo, "Competing wave-breaking mechanisms in quadratic media," Opt. Lett. 38, 1648 (2013).

J49. A. Auditore, M. Conforti, C. De Angelis, and A. B. Aceves, "Dark–antidark solitons in waveguide arrays with alternating positive–negative couplings," Opt. Commun. 297, 125 (2013).

J50. F. Baronio, M. Conforti, A. Degasperis, and S. Lombardo, "Rogue Waves Emerging from the Resonant Interaction of Three Waves," Phys. Rev. Lett. 111, 114101 (2013).

J51. M. Conforti and S. Trillo, "Dispersive wave emission from wave breaking," Opt. Lett. 38, 3815 (2013).

J52. M. Conforti and F. Baronio, "Extreme high-intensity and ultrabroadband interactions in anisotropic BBO crystals," J. Opt. Soc. Am. B 30, 1041 (2013).

J53. F. Baronio, M. Conforti, C. De Angelis, D. Modotto, S. Wabnitz, M. Andreana, A. Tonello, P. Leproux, and V. Couderc, "Second and third order susceptibilities mixing for supercontinuum generation and shaping," Opt. Fiber Technol. 18, 283 (2012).

J54. M. Levenius, M. Conforti, F. Baronio, V. Pasiskevicius, F. Laurell, C. De Angelis, and K. Gallo, "Multistep quadratic cascading in broadband optical parametric generation," Opt. Lett. 37, 1727 (2012).

J55. F. Baronio, M. Conforti, C. De Angelis, M. Andreana, A. Tonello, and V. Couderc, "Tunable light source from large band conversion of continuum in a quadratic crystal," Laser Phys. Lett. 9, 359 (2012).

J56. G. Della Valle, M. Conforti, S. Longhi, G. Cerullo, and D. Brida, "Real-time optical mapping of the dynamics of nonthermal electrons in thin gold films," Phys. Rev. B 86, 155139 (2012).

J57. M. Conforti, C. De Angelis, T. R. Akylas, and A. B. Aceves, "Modulational stability and gap solitons of gapless systems: Continuous versus discrete limits," Phys. Rev. A 85, 63836 (2012).

J58. F. Baronio, A. Degasperis, M. Conforti, and S. Wabnitz, "Solutions of the Vector Nonlinear Schrödinger Equations: Evidence for Deterministic Rogue Waves," Phys. Rev. Lett. 109, 44102 (2012).

J59. M. Conforti, F. Baronio, and S. Trillo, "Dispersive shock waves in phase-mismatched second-harmonic generation," Opt. Lett. 37, 1082 (2012).

J60. M. Conforti and G. Della Valle, "Derivation of third-order nonlinear susceptibility of thin metal films as a delayed optical response," Phys. Rev. B 85, 245423 (2012).

J61. F. Scotognella, G. Della Valle, A. R. Srimath Kandada, D. Dorfs, M. Zavelani-Rossi, M. Conforti, K. Miszta, A. Comin, K. Korobchevskaya, G. Lanzani, L. Manna, and F. Tassone, "Plasmon Dynamics in Colloidal Cu 2– x Se Nanocrystals," Nano Lett. 11, 4711 (2011).

J62. F. Baronio, M. Andreana, M. Conforti, G. Manili, V. Couderc, C. De Angelis, and A. Barthélémy, "Soliton triads ensemble in frequency conversion: from inverse scattering theory to experimental observation," Opt. Express 19, 13192 (2011).

J63. M. Andreana, F. Baronio, M. Conforti, A. Tonello, C. De Angelis, and V. Couderc, "Mode-locking operation of a flash-lamp-pumped Nd:YAG laser at 1.064μm with Zakharov-Manakov solitons," Laser Phys. Lett. 8, 795 (2011).

J64. A. Degasperis, M. Conforti, F. Baronio, S. Wabnitz, and S. Lombardo, "The Three-Wave Resonant Interaction Equations: Spectral and Numerical Methods," Lett. Math. Phys. 96, 367 (2011).

J65. M. Conforti, F. Baronio, C. De Angelis, M. Marangoni, and G. Cerullo, "Theory and experiments on multistep parametric processes in nonlinear optics," J. Opt. Soc. Am. B 28, 892 (2011).

J66. M. Conforti, F. Baronio, and A. Degasperis, "Modulational instability of dark solitons in three wave resonant interaction," Phys. D Nonlinear Phenom. 240, 1362 (2011).

J67. M. Conforti, C. De Angelis, and T. R. Akylas, "Energy localization and transport in binary waveguide arrays," Phys. Rev. A 83, 43822 (2011).

J68. M. Conforti, F. Baronio, and C. De Angelis, "Modeling of ultrabroadband and single-cycle phenomena in anisotropic quadratic crystals," J. Opt. Soc. Am. B 28, 1231 (2011).

J69. M. Conforti and F. Baronio, "Soliton dynamics in velocity matched ultrafast frequency conversion processes," Eur. Phys. J. D 64, 115 (2011).

J70. M. Guasoni and M. Conforti, "Complex dispersion relation of a double chain of lossy metal nanoparticles," J. Opt. Soc. Am. B 28, 1019 (2011).

J71. F. Baronio, M. Conforti, C. De Angelis, A. Degasperis, M. Andreana, V. Couderc, and A. Barthélémy, "Velocity-Locked Solitary Waves in Quadratic Media," Phys. Rev. Lett. 104, 113902 (2010).

J72. M. Conforti, F. Baronio, and C. De Angelis, "Nonlinear envelope equation for broadband optical pulses in quadratic media," Phys. Rev. A 81, 53841 (2010).

J73. M. Conforti, F. Baronio, and C. De Angelis, "Ultrabroadband Optical Phenomena in Quadratic Nonlinear Media," IEEE Photonics J. 2, 600 (2010).

J74. M. Guasoni, M. Conforti, and C. De Angelis, "Light propagation in nonuniform plasmonic subwavelength waveguide arrays," Opt. Commun. 283, 1161 (2010).

J75. M. Conforti and M. Guasoni, "Dispersive properties of linear chains of lossy metal nanoparticles," J. Opt. Soc. Am. B 27, 1576 (2010).

J76. M. Marangoni, D. Brida, M. Conforti, A. D. Capobianco, C. Manzoni, F. Baronio, G. F. Nalesso, C. De Angelis, R. Ramponi, and G. Cerullo, "Synthesis of picosecond pulses by spectral compression and shaping of femtosecond pulses in engineered quadratic nonlinear media," Opt. Lett. 34, 241 (2009).

J77. F. Baronio, M. Conforti, M. Andreana, V. Couderc, C. De Angelis, S. Wabnitz, A. Barthélémy, and A. Degasperis, "Frequency generation and solitonic decay in three wave interactions," Opt. Express 17, 13889 (2009).

J78. M. Marangoni, G. Sanna, D. Brida, M. Conforti, G. Cirmi, C. Manzoni, F. Baronio, P. Bassi, C. De Angelis, and G. Cerullo, "Observation of spectral drift in engineered quadratic nonlinear media," Appl. Phys. Lett. 93, 21107 (2008).

J79. M. Conforti, F. Baronio, C. De Angelis, G. Sanna, D. Pierleoni, and P. Bassi, "Spectral shaping of femtosecond pulses in aperiodic quasi-phase-matched gratings," Opt. Commun. 281, 1693 (2008).

J80. M. Conforti, C. de Angelis, U. K. Sapaev, and G. Assanto, "Pulse shaping via Backward Second Harmonic Generation," Opt. Express 16, 2115 (2008).

J81. M. Conforti, M. Guasoni, and C. De Angelis, "Subwavelength diffraction management," Opt. Lett. 33, 2662 (2008).

J82. F. Baronio, M. Conforti, A. Degasperis, and S. Wabnitz, "Three-Wave Trapponic Solitons for Tunable High-Repetition Rate Pulse Train Generation," IEEE J. Quantum Electron. 44, 542 (2008).

J83. A. Parini, G. Bellanca, S. Trillo, M. Conforti, A. Locatelli, and C. De Angelis, "Self-pulsing and bistability in nonlinear Bragg gratings," J. Opt. Soc. Am. B 24, 2229 (2007).

J84. M. Conforti, F. Baronio, A. Degasperis, and S. Wabnitz, "Parametric frequency conversion of short optical pulses controlled by a CW background," Opt. Express 15, 12246 (2007).

J85. A. Degasperis, M. Conforti, F. Baronio, and S. Wabnitz, "Effects of nonlinear wave coupling: Accelerated solitons," Eur. Phys. J. Spec. Top. 147, 233 (2007).

J86. D. Modotto, M. Conforti, A. Locatelli, and C. De Angelis, "Imaging Properties of Multimode Photonic Crystal Waveguides and Waveguide Arrays," J. Light. Technol. 25, 402 (2007).

J87. M. Conforti, F. Baronio, and C. De Angelis, "From femtosecond infrared to picosecond visible pulses: temporal shaping with high-efficiency conversion," Opt. Lett. 32, 1779 (2007).

J88. A. Tonello, S. Pitois, S. Wabnitz, G. Millot, T. Martynkien, W. Urbanczyk, J. Wojcik, A. Locatelli, M. Conforti, and C. De Angelis, "Frequency tunable polarization and intermodal modulation instability in high birefringence holey fiber," Opt. Express 14, 397 (2006).

J89. M. Lauritano, A. Parini, G. Bellanca, S. Trillo, M. Conforti, A. Locatelli, and C. De Angelis, "Bistability, limiting, and self-pulsing in backward second-harmonic generation: a time-domain approach," J. Opt. A Pure Appl. Opt. 8, S494 (2006).

J90. D. Boffi, M. Conforti, and L. Gastaldi, "Modified edge finite elements for photonic crystals," Numer. Math. 105, 249 (2006).

J91. A. Degasperis, M. Conforti, F. Baronio, and S. Wabnitz, "Stable Control of Pulse Speed in Parametric Three-Wave Solitons," Phys. Rev. Lett. 97, 93901 (2006).

J92. A. Locatelli, M. Conforti, D. Modotto, and C. De Angelis, "Discrete negative refraction in photonic crystal waveguide arrays," Opt. Lett. 31, 1343 (2006).

J93. M. Conforti, F. Baronio, A. Degasperis, and S. Wabnitz, "Inelastic scattering and interactions of three-wave parametric solitons," Phys. Rev. E 74, 65602 (2006).

J94. A. Locatelli, M. Conforti, D. Modotto, and C. De Angelis, "Diffraction engineering in arrays of photonic crystal waveguides," Opt. Lett. 30, 2894 (2005).

J95. M. Conforti, A. Locatelli, C. De Angelis, A. Parini, G. Bellanca, and S. Trillo, "Self-pulsing instabilities in backward parametric wave mixing," J. Opt. Soc. Am. B Opt. Phys. 22, 2178 (2005).

A.2 Book chapters (7)

B1. S. Trillo and M. Conforti, "Shock Waves," in "Handbook of Optical Fibers," Springer (to appear)

B2. A. Kudlinski, D. Skryabin, A. Mussot, and M. Conforti, "Emission of Dispersive Waves from Solitons in Optical Fibers," in "Handbook of Optical Fibers," Springer (to appear)

B3. M. Conforti, G. Xu, A. Mussot, A. Kudlinski and S. Trillo, "Observation of the rupture of a photon dam in an optical fiber," in "Nonlinear Guided Wave Optics: A testbed for extreme waves," IOP Publishing Ltd. (to appear)

B4. S. Trillo and M. Conforti, "Wave-Breaking and Dispersive Shock Wave Phenomena in Optical Fibers," in "Shaping Light in Nonlinear Optical Fibers," Wiley 2017 (ISBN: 978-1-119-08812-7)

B5. A. Mussot, M. Conforti, and A. Kudlinski, "Modulation Instability in Periodically Modulated Fibers," in "Shaping Light in Nonlinear Optical Fibers," Wiley 2017 (ISBN: 978-1-119-08812-7)

B6. M. Conforti, and S. Trillo, "Dispersive Shock Waves: From Water Waves to Nonlinear Optics," in "Rogue and Shock Waves in Nonlinear Dispersive Media," Springer 2016 (Lecture Notes in Physics 926, ISBN: 978-3-319-39214-1).

B7. F. Baronio, M. Conforti, C. De Angelis, A. Degasperis, S. Lombardo, and S. Wabnitz, "Frequency conversion based on three-wave parametric solitons," in "Advances in Lasers and Electro Optics," Intech 2010 (ISBN: 978-953-307-088-9).

A.3 Invited Conferences (14)

I1. A. Kudlinski, M. Conforti, and A. Mussot, "Interactions between solitons and dispersive waves in optical fibers," Nonlinear Photonics, Sydney, Australia, September 2016.

I2. M. Conforti, "Background-enhanced dispersive shock generation in optical fibers," Workshop on Abnormal Wave Events (W-AWE 2016), Nice, France, June 2016.

I3. K. Gallo, M. Levenius, and M. Conforti, "Twin-beam Optical Parametric Generation and Cascaded Processes in Hexagonally Poled Nonlinear Lattices," Progress In Electromagnetics Research Symposium (PIERS 2015), Prague, July 2015.

I4. A. Aceves, F. Baronio, M. Conforti, A. Degasperis, B. Frisquet, B. Kibler, S. Lombardo, G. Millot, P. Morin, and S. Wabnitz, "Multicomponent Rogue Waves," Progress In Electromagnetics Research Symposium (PIERS 2015), Prague, July 2015.

I5. A. Kudlinski, M. Conforti, A. Bendhamane, F. Copie, F. Braud, S. Wang, S. Rota Nodari, G. Dujardin, S. De Bièvre, S. Trillo, and A. Mussot, "Topographic optical fibers: a new degree of freedom in nonlinear optics," Frontiers in Optics, San Jose, California, October 2015.

I6. M. Conforti, "Emission of radiation from dispersive shock waves," Rogue waves and shock waves in nonlinear dispersive media, Cargese, France, July 2015

I7. A. Kudlinski, M. Conforti, A. Bendhamane, F. Copie, F. Braud, S. Wang, S. Rota Nodari, G. Dujardin, S. De Bièvre, S. Trillo, and A. Mussot, "Topographic optical fibers: a new degree of freedom in nonlinear optics," Asia Communications and Photonics Conference, Hong Kong, November 2015.

I8. M. Conforti, "Vector Rogue Waves and Baseband Modulation Instability in the Defocusing Regime," Workshop on Abnormal Wave Events (W-AWE 2014), Nice, France, June 2014.

I9. K. Gallo, K. Stensson, M. Levenius, M. Swillo, G. Bjork, and M. Conforti, "Twin-beam parametric processes in nonlinear photonic crystals," International Conference on Transparent Optical Networks (ICTON 2014), Graz, Austria, July 2014.

I10. M. Conforti, F. Baronio, and C. De Angelis, "Nonlinear envelope equation for broadband optical pulses in quadratic media," SIMAI conference on Applied and Industrial Mathematics, Cagliari, Italy, June 2010.

I11. F. Baronio, M. Conforti, C. De Angelis, A. Degasperis, M. Andreana, V. Couderc, and A. Barthélémy, "Observation of velocity-locked three-wave interaction solitons," 19th International Laser Physics Workshop, Foz do Iguaçu, Brazil, July 2010.

I12. M. Conforti, F. Baronio, A. Degasperis, and S. Wabnitz, "Three waves resonant interaction solitons: novel features and applications in nonlinear optics," SIAM Conference on Nonlinear Waves and Coherent Structures (NW08), Rome (Italy), July 2008.

I13. F. Baronio, M. Conforti, A. Degasperis, and S. Wabnitz, "Control of velocity-locked three wave parametric solitons and soliton based frequency conversion in quadratic nonlinear optics," 8th Mediterranean Workshop and Topical Meeting "Novel Optical Materials and Applications" (NOMA-07), Cetraro (Italy), June 2007.

I14. S. Wabnitz, A. Tonello, S. Pitois, G. Millot, T. Martynkien, W. Urbanczyk, J. Wojcik, A. Locatelli, M. Conforti, and C. De Angelis, "Experiments and theory of tunable broadband parametric gain in photonic crystal fibers," 12th Conference on Laser Optics (LO'2006), St. Perersburg (Russia), June 2006.

A.4 International peer-reviewed conferences (59)

C1. G. Xu, A. Mussot, A. Kudlinski, S. Trillo, F. Copie, and M. Conforti, "Observation of the breaking of a pulse on a weak background in optical fibers," oral presentation, Laser Science to Photonic Applications (CLEO-QELS 2016), San Jose, California, June 2016.

C2. F. Braud, M. Conforti, A. Cassez, A. Mussot, and A. Kudlinski, "Transformation of a dispersive wave into a fundamental soliton," oral presentation, Laser Science to Photonic Applications (CLEO-QELS 2016), San Jose, California, June 2016.

C3. F. Copie, M. Conforti, A. Kudlinski, S. Trillo, and A. Mussot, "Observation of Turing and Faraday instabilities in a bistable passive resonator," oral presentation, Laser Science to Photonic Applications (CLEO-QELS 2016), San Jose, California, June 2016.

C4. M. Conforti, A. Mussot, A. Kudlinski, S. Rota Nodari, G. Dujardin, S. De Bièvre, A. Armaroli, and S. Trillo, "Nonlinear Stage of Modulation Instability in Dispersion Oscillating Fibers," poster presentation, Laser Science to Photonic Applications (CLEO-QELS 2016), San Jose, California, June 2016.

C5. C. Mas Arabi, F. Bessin, A. Mussot, A. Kudlinski, D. Skryabin, and M. Conforti, "Vector collisions between solitons and dispersive waves," oral presentation, Nice Optics, Nice, France, October 2016.

C6. C. Mas Arabi, F. Bessin, A. Mussot, A. Kudlinski, D. Skryabin, and M. Conforti, "Conversion efficiency of vector scattering between solitons and dispersive waves," oral presentation, Nonlinear Photonics, Sydney, Australia, September 2016.

C7. M. Conforti, A. Mussot, A. Kudlinski, S. Rota Nodari, G. Dujardin, S. De Bièvre, A. Armaroli, and S. Trillo, "Heteroclinic Structure of Parametric Resonance in Fibers with Periodic Dispersion," oral presentation, Nonlinear Photonics, Sydney, Australia, September 2016.

C8. F. Copie, M. Conforti, A. Kudlinski, A. Mussot, and S. Trillo, "Roundtrip-to-roundtrip evolution of Faraday and Turing instabilities in dispersion oscillating fiber ring resonators," oral presentation, Nonlinear Photonics, Sydney, Australia, September 2016.

C9. F. Baronio, S. Wabnitz, and M. Conforti, "Baseband Modulation Instability as the Origin of Rogue Waves," Nonlinear Evolution Equations and Dynamical Systems (NEEDS 2015), oral presentation, Sardina, Italy, May 2015.

C10. M. Conforti and S. Trillo, "Emission of radiation from perturbed dispersive shock waves," Nonlinear Evolution Equations and Dynamical Systems (NEEDS 2015), oral presentation, Sardina, Italy, May 2015.

C11. F. Baronio, S. Wabnitz, S. Chen, P. Grelu, and M. Conforti, "Baseband Modulation Instability as the Origin of Rogue Waves," poster presentation, CLEO-Europe 2015, Munich, June 2015.

C12. M. Conforti, S. Rota Nodari, G. Dujardin, A. Mussot, and S. Trillo, "Modulation instability in periodically dispersion kicked optical fibers," poster presentation, CLEO-Europe 2015, Munich, June 2015.

C13. G. Xu, J. Garnier, S. Trillo, M. Conforti, D. Churkin, S. Turitsyn, and A. Picozzi, "Towards a Generalized Weak Langmuir Optical Turbulence," oral presentation, CLEO-Europe 2015, Munich, June 2015.

C14. A. Bendahmane, A. Mussot, A. Kudlinski, P. Szriftgiser, M. Conforti, S. Wabnitz, and S. Trillo, "Optimal conversion in the depleted stage of modulation instability," oral presentation, CLEO-Europe 2015, Munich, June 2015.

C15. B. Frisquet, B. Kibler, J. Fatome, P. Morin, F. Baronio, M. Conforti, G. Millot, and S. Wabnitz, "Observation of Black Vector Rogue Waves in the Normal Dispersion Regime of Optical Fibers," oral presentation, CLEO-Europe 2015, Munich, June 2015.

C16. F. Copie, M. Conforti, A. Kudlinski, S. Trillo, and A. Mussot, "Demonstration of Modulation Instability in dispersion oscillating fiber ring cavity," oral presentation, CLEO-Europe 2015, Munich, June 2015.

C17. M. Conforti, S. Trillo, A. Mussot, and A. Kudlinski, "Emission of quasi-resonant radiations in dispersion oscillating fibers," poster presentation, CLEO-Europe 2015, Munich, June 2015.

C18. S. Wang, A. Mussot, M. Conforti, A. Bendahmane, X. Zeng, and A. Kudlinski, "Optical Event Horizons in a Dispersion Varying Optical Fiber," poster presentation, CLEO-Europe 2015, Munich, June 2015.

C19. S. Malaguti, M. Conforti, G. Bellanca, and S. Trillo, "Radiating Dissipative-Dispersive Shock Waves via Bistability in Passive Microcavities," Nonlinear Photonics, oral presentation, Barcelona, Spain, July 2014.

C20. F. Baronio, M. Conforti, A. Degasperis, S. Lombardo, M. Onorato, and S. Wabnitz, "Vector rogue waves and modulation instability in the defocusing regime," Nonlinear Photonics, oral presentation, Barcelona, Spain, July 2014.

C21. M. Conforti, A. Marini, D. Faccio, and F. Biancalana, "Interaction between positive and negative frequencies in nonlinear optics," Nonlinear Photonics, oral presentation, Barcelona, Spain, July 2014.

C22. M. Conforti, A. Mussot, A. Kudlinski, and S. Trillo, "Modulational instability and pulse generation in dispersion oscillating fiber ring cavities," Nonlinear Photonics, oral presentation, Barcelona, Spain, July 2014.

C23. B. Kibler, B. Frisquet, P. Morin, J. Fatome, F. Baronio, M. Conforti, G. Millot, and S. Wabnitz, "Manakov Polarization Modulation Instability in Normal Dispersion Optical Fiber," Nonlinear Photonics, oral presentation, Barcelona, Spain, July 2014.

C24. M. Conforti, F. Baronio, M. Levenius, and K. Gallo, "Broadband parametric processes in quadratic nonlinear photonic crystals," Nonlinear Photonics, poster presentation, Barcelona, Spain, July 2014.

C25. B. Kibler, B. Frisquet, P. Morin, J. Fatome, F. Baronio, M. Conforti, G. Millot, and S. Wabnitz, "Observation of Manakov Polarization Modulation Instability in the Normal Dispersion Regime of Randomly Birefringent Telecom Optical Fiber," European Conference of Optical Communications (ECOC 2014), oral presentation, Cannes, France, September 2014.

C26. M. Conforti and F. Baronio, "Modelling of broadband electric field propagation in nonlinear dielectric media," European Conference on Modelling and Simulation, oral presentation, Brescia, Italy, May 2014.

C27. M. Conforti, F. Baronio, and S. Trillo, "Resonant radiation induced by wave-breaking," Frontiers in Optics 2013, oral presentation, Orlando, California, October 2013.

C28. A. Marini, M. Conforti, G. Della Valle, and F. Biancalana, "Ultrafast interband nonlinear dynamics of surface plasmon polaritons in gold nanowires," Laser Science to Photonic Applications (CLEO-QELS 2012), oral presentation, San Jose, California, June 2013.

C29. M. Conforti, N. Westerberg, F. Baronio, S. Trillo, and D. Faccio, "Negative frequency resonant radiation in quadratic crystals," poster presentation, CLEO-Europe 2013, Munich, May 2013.

C30. M. Conforti, F. Baronio, and S. Trillo, "Competing Wave-Breaking Mechanisms in Dispersive Second Harmonic Generation," oral presentation, CLEO-Europe 2013, Munich, May 2013.

C31. F. Baronio, M. Conforti, A. Degasperis, and S. Wabnitz," Rogue Waves of the Vector Nonlinear Schrödinger Equations," oral presentation, CLEO-Europe 2013, Munich, May 2013.

C32. F. Baronio, A. Degasperis, M. Conforti, and S. Wabnitz, "Deterministic freak waves of vector nonlinear Schrödinger equations," Nonlinear Evolution Equations and Dynamical Systems (NEEDS 2012), oral presentation, Crete, Greece, July 2012.

C33. M. Conforti, F. Baronio, and S. Trillo, "Dispersive shock waves in phase mismatched second harmonic generation," Nonlinear Evolution Equations and Dynamical Systems (NEEDS 2012), oral presentation, Crete, Greece, July 2012.

C34. M. Conforti, F. Baronio, and S. Trillo, "Dispersive shock waves in quadratic media," Nonlinear Photonics (NP 2012), oral presentation, Colorado Springs, Colorado, June 2012.

C35. M. Conforti, F. Baronio, and C. De Angelis, "Modelling of supercontinuum generation in quadratic crystals," Laser Science to Photonic Applications (CLEO-QELS 2012), oral presentation, San Jose, California, May 2012.

C36. M. Levenius, M. Conforti, F. Baronio, V. Pasiskevicious, F. Laurell, and K. Gallo, "Quadratic Cascading effects in broadband optical parametric generation," Advanced Solid-State Photonics (ASSP), oral presentation, San Diego, California, February 2012.

C37. S. Baruffolo, M. Conforti, C. De Angelis, A. Flammini, and E. Sisinni, "A finite element aided tool for the design of microwave resonant sensors," poster presentation, IEEE International Instrumentation and Measurement Technology Conference (I2MTC 2011), Hangzhou, China, May 2011.

C38. M. Conforti, F. Baronio, and C. De Angelis, "Nonlinear envelope equation for broadband optical pulses in quadratic media," Nonlinear Waves - Theory and Applications, oral presentation, Beijing, China, June 2010.

C39. M. Marangoni, D. Brida, M. Conforti, A.D. Capobianco, C. Manzoni, C. De Angelis, R. Ramponi, and G. Cerullo, "Arbitrarily shaped picosecond pulses by spectral compression of femtosecond pulses in engineered quadratic media," Proc. CLEO/Europe 2009, Munich, Germany, June 2009.

C40. F. Baronio, M. Conforti, M. Andreana, V. Couderc, C. De Angelis, S. Wabnitz, A. Degasperis, and A. Barthélémy, "Frequency generation and solitonic decay in three-wave nonlinear interactions," DGAO-SIOF Conference, oral presentation, Brescia (Italy), June 2009.

C41. M. Marangoni, D. Brida, M. Conforti, A. D. Capobianco, C. Manzoni, F. Baronio, G. F. Nalesso, C. De Angelis, R. Ramponi, and G. Cerullo, "Synthesis and shaping of picosecond pulses by frequency conversion of femtosecond pulses in engineered quadratic media," DGAO-SIOF Conference, oral presentation, Brescia (Italy), June 2009.

C42. F. Baronio, M. Conforti, C. De Angelis, A. Degasperis, S. Wabnitz, M. Andreana, V. Couderc, and A. Barthélémy, "Experimental Evidence of Three-Wave Zakharov-Manakov Solitons," Nonlinear Evolution Equations and Dynamical Systems (NEEDS 2009), oral presentation, Sardinia (Italy), May 2009.

C43. M. Marangoni, D. Brida, C. Manzoni, R. Ramponi, G. Cerullo, M. Conforti, F. Baronio, and C. De Angelis, "Synthesis and Shaping of Picosecond Pulses by Frequency Conversion of Femtosecond Pulses in Engineered Quadratic Media," CLEO/IQEC 2009, oral presentation, Baltimore (Maryland), May 2009.

C44. M. Conforti, M. Guasoni, F. Gringoli, and C. De Angelis, "Diffraction management in metal dielectric nanoscale periodic media," 2nd European Topical Meeting on Nanophotonics and Metamaterials, poster presentation, Seefeld (Tirol), Austria, January 2009.

C45. M. Marangoni, D. Brida, G. Cirmi, C. Manzoni, G. Cerullo, D. Fusaro, F. M. Pigozzo, A. D. Capobianco, F. Baronio, M. Conforti, and C. De Angelis, "Tunable narrow-bandwidth picosecond pulses by spectral compression of femtosecond pulses in second-order nonlinear crystals," Conference on Lasers and Electro-Optics (CLEO), oral presentation, San Jose (USA), May 2008.

C46. F. Baronio, M. Conforti, A. Degasperis, and S. Wabnitz, "Three-wave trapponic solitons for tunable high repetition rate pulse train generation," 2008 IEEE/LEOS Winter Topical Meetings, oll presentation, Sorrento (Italy), January 2008.

C47. M. Conforti, F. Baronio, S. Wabnitz, and A. Degasperis, "Parametric frequency conversion of optical simulton pulses," Conference on Lasers and Electro-Optics (CLEO), poster presentation, Baltimore (USA), May 2007.

C48. A. Degasperis, M. Conforti, F. Baronio, and S. Wabnitz, "Propagation and interactions of three-wave parametric solitons," International workshop on Instabilities, Patterns and Spatial Solitons (IPSSO), oral presentation, Metz (France), March 2007.

C49. A. Degasperis, M. Conforti, F. Baronio, and S. Wabnitz, "Propagation stability and interactions of novel three-wave parametric solitons," 19th Annual Meeting of the IEEE Lasers & Electro-Optics Society (LEOS 2006), oral presentation, Montreal (Canada), November 2006.

C50. A. Locatelli, M. Conforti, D. Modotto, and C. De Angelis, "Anomalous refractive effects in photonic crystal waveguide arrays," EOS Topical Meeting on Nanophotonics, Metamaterials, and Optical Microcavities, poster presentation, Paris (France), October 2006.

C51. A. Degasperis, M. Conforti, F. Baronio, S. Wabnitz, "Propagation and stability of novel parametric interaction solitons," 12th Conference on Laser Optics (LO'2006), oral presentation, St. Perersburg (Russia), June 2006.

C52. M. Conforti, A. Locatelli, C. De Angelis, A. Parini, M. Lauritano, S. Trillo, G. Bellanca, "Self pulsing due to backward second-harmonic generation in engineered PPLN: the role of the induced cubic nonlinearity," 12th Conference on Laser Optics (LO'2006), poster presentation, St. Perersburg (Russia), June 2006.

C53. A. Tonello, S. Pitois, S. Wabnitz, G. Millot, T. Martynkien, W. Urbanczyk, J. Wojcik, A. Locatelli, M. Conforti, and C. De Angelis, "Observation of Frequency Tunable Cross-Phase Modulation Instabilities in Highly Birefringent Photonic Crystal Fiber" , Conference on Lasers and Electro-Optics/Quantum Electronics and Laser Science Conference (CLEO/QELS 2006), oral presentation, Long Beach (California, USA), May 2006.

C54. A. Locatelli, M. Conforti, D. Modotto, and C. De Angelis, "Discrete Negative Refraction and Left-Handed Propagation in Photonic Crystal Waveguide Arrays," Conference on Lasers and Electro-Optics / Quantum Electronics and Laser Science Conference (CLEO/QELS 2006), poster presentation, Long Beach (California, USA), May 2006.

C55. M. Lauritano, S. Trillo, G. Bellanca, M. Conforti, A. Locatelli, and C. De Angelis, "Time-domain analysis of parametric frequency conversion," Optical Waveguide Theory and Numerical Modelling (OWTNM 2006), oral presentation, Varese (Italy), April 2006.

C56. S. Pitois, A. Tonello, S. Wabnitz, G. Millot, T. Martynkien, W. Urbanczyk, J. Wojcik, A. Locatelli, M. Conforti, D. Modotto, and C. De Angelis, "Observation of frequency tunable polarization and modal modulation instability in birefringent holey fiber with triple defects," 18th Annual Meeting of the IEEE Lasers & Electro-Optics Society (LEOS 2005), oral presentation, Sydney (Australia), October 2005.

C57. A. Parini, M. Lauritano, G. Bellanca, S. Trillo, M. Conforti, A. Locatelli, and C. De Angelis, "Analysis of backward second-harmonic generation in short period gratings," Optical Microsystems (OmS05), oral presentation, Capri (Italy), September 2005.

C58. M. Conforti, A. Locatelli, C. De Angelis, A. Parini, G. Bellanca, and S. Trillo, "Pulse train generation by counterpropagating second order nonlinear interactions," Nonlinear Guided Waves and Their Applications (NLGW 2005), oral presentation, Dresden (Germany), September 2005.

C59. M. Conforti, A. Locatelli, C. De Angelis, A. Parini, G. Bellanca, S. Trillo, "Self-pulsing instability in backward parametric interactions," IEEE/LEOS 4th Workshop on Fibres and Passive Optical Components (WFOPC 2005), poster presentation, Palermo (Italy), June 2005.

A.5 Patents (1)

P1. G. Cerullo, M. Marangoni, F. Baronio, M. Conforti, C. De Angelis, "System for generating Raman vibrational analysis signals," Publication number: WO2010013118 (A1), Publication date: 2010-02-04.

APPENDIX B

Curriculum Vitae

B.1 Personal details

First name :	Matteo
Family name :	CONFORTI
Date of birth :	05/10/1978
Nationality :	Italian
Address :	12 place du récital 59650, Villeneuve d'Ascq
Civil status:	Civil union, no children

B.2 Current positon

Position :	CNRS Researcher (CR1)
Section :	04, Atoms and molecules - Optics and lasers - Hot plasmas
Affiliation :	Laboratoire de Physique des Lasers, Atomes et Molécules (PhLAM) UMR CNRS 8523 Université Lille 1
Team:	Photonics
Subjects :	Nonlinear fiber optics, Nonlinear dynamics, Instabilities, Shock Waves
Address :	IRCICA insitute Parc de la Haute Borne 50 avenue de Halley 59658, Villeneuve d'Ascq
Phone :	+33 (0)3 62 53 16 54
Email :	matteo.conforti@univ-lille1.fr

B.3 Studies

2004-2007 : **Doctorate** in Electronic Instrumentation
University of Brescia
Theoretical and numerical modelling of nanostructured photonics devices

1997-2003 : **Laurea** (bachelor's degree) in Electronic Engineering
University of Brescia
Analisi mediante elementi finiti di tipo "edge" delle frequenze del campo magnetico in cristalli fotonici

1992-1997 : **Diploma di maturità Scientifica** (baccalaureate in science)
Liceo scientifico Annibale Calini

B.4 Past research positions

2013-2015 : Research Officer
Laboratoire de Physique des Lasers, Atomes et Molécules (PhLAM)
Nonlinear optics in topographic fibers

2011-2013 : Research Associate
Department on Information Engineering, University of Brescia
Optical antennas for solar cells

2009-2010 : CNISM Research Associate
Department of Information Engineering, University of Brescia
Plasmonic devices for the control of electromagnetic propagation on the nanometer scale

2006-2009 : Research Associate
Department of Electronics for Automation, University of Brescia
Nanostructured optical devices for high bit-rate communication systems

APPENDIX C

Teaching and Supervision

C.1 Supervision of postdocs

2015-2017 : Gang XU
Dispersive shock waves in optical fibers

C.2 Co-supervision of PhD students

From 2014 : François COPIE
at 50% with Arnaud Mussot
Modulation instabilities in dispersion oscillating passive fiber-ring fibers

From 2015 : Carlos MAS ARABI
at 50% with Alexandre Kudlinski
Théorie des interactions entre solitons et ondes dispersives dans les fibres optiques

From 2015 : Tomy MAREST
at 50% with Alexandre Kudlinski
Dynamique non-linéaire d'ondes extrêmes

From 2016 : Florent BESSIN
at 50% with Arnaud Mussot
Etude des effets non linéaires dans les cavités passives à fibre topographique

From 2016 : Corentin NAVEAU
at 30% with Arnaud Mussot and Pascal Szriftgiser
Etude expérimentale approfondie du processus d'instabilité de modulation dans les fibres optiques topographiques via une caractérisation en phase et en intensité des ondes mises en jeu

C.3 Informal co-supervision of defended PhD thesis

2013-2016 : Flavie BRAUD, Université Lille 1
Solitons et ondes dispersives dans les fibres à dispersion oscillante

2009-2011 : Massimiliano GUASONI, Università di Brescia
Surface plasmons and discrete diffraction in coupled waveguide arrays

2009-2011 : Marco ANDREANA, Università di Brescia - XLIM
Soliton propagzation in crystal and optical fibers

C.4 Supervision of Master students

2010 : Stefano CIRELLI, Università di Brescia
Generazione di impulsi ottici per spettroscopia Raman

2009 : Stefano BARUFFOLO, Università di Brescia
Studio, simulazione e realizzazione di una cavità risonante per applicazioni sensoristiche

2008 : Dario TOMASONI, Università di Brescia
Generazione di forme d'onda tramite conversione di frequenza

2005 : Enrico COLOMBO, Università di Brescia
Studio della propagazione elettromagnetica in guide d'onda accoppiate a cristallo fotonico

C.5 Teaching

2014 : Interference and diffraction, TelecomLille
Engineering school, second year, 20 hours (TD)

2011-2012 : Optical communications, Università di Brescia
L3, 20 hours (TD)

2004-2008 : Numerical analysis , Università di Brescia
L3, 75 hours (TD)

2004-2008 : Advanced numerical analysis , Università di Brescia
Master, 75 hours (TD)

APPENDIX D

Scientific responsibilities, collaborations and impact

D.1 Scientific responsibilities of research projects

2014-2018 : *Nonlinear dynamics of abnormal wave events*
Principal investigator
ANR project, funding 460k€
I achieved this project in the framework of the call *@RAction, Accuel de Chercheurs de haut niveau*. The programme aims to promote the hosting of prominent researchers from abroad, by offering them substantial funding to carry out ambitious research in various new domains that are rare or nonexistent in France. The programme is intended to enable host entities to strengthen their international visibility.
The research project is devoted to the study of waves with extreme features, with particular emphasis on Dispersive Shock Waves. The purpose of the project is twofold: a theoretical description of extreme events in different physical settings, and an experimental analysis of the process in the domain of nonlinear optics. The results of this project will be useful for a better understanding of the nature of extreme events in several physical scenarios.

2011-2013 : *Optical shock waves: theory and experiments*
Responsible of a work package
PRIN project, funding 152k€

2011-2012 : *Engineering optical nonlinearities using plasmon resonances in metal-insulator metamaterials*
Responsible of a work package
CARIPLO project, funding 300k€

2008-2009 : *Temporal and spectral shaping of optical pulses for high resolution optical microscopy*
Responsible of a work package
PRIN project, funding 250k€

2006-2007 : *Numerical and analytical modelling of parametric and photonic-bangap devices in waveguides in surface periodically poled lithium niobate and lithium tantalate*
Responsible of a work package
PRIN project, funding 460k€

D.2 Scientific collaborations

- Polythecnic of Milan, Department of Physics
  G. Cerullo, G. Della Valle, S. Longhi
  Ultrafast nonlinear optical phenomena
  Plasmonics

- University of Rome "Sapienza", Department of Physics
  A. Degasperis
  Solitons and integreble systems
  Rogue waves

- University of Limoges, XLIM
  A. Barthélémy, V. Couderc
  Quadratic solitons

- University of Ferrara, Department of Engineering
  S.Trillo
  Nonlinear optics
  Shock waves

- Massachusetts Institute of Technology, Department of Mechanical Engineering
  T. R. Akylas
  Solitons in discrete systems

- University of Torino, Department of Physics
  M. Onorato
  Rogue waves

- University of Burgundy, ICB
  G. Millot, A. Picozzi
  Rogue waves in cavities
  Shock waves

- KTH Stockholm, Department of Applied Physics
  K. Gallo, V. Pasiskevicius
  Broadband optical parametric generation

- University of Brescia, Department of Information Engineering
  F. Baronio, C. De Angelis, S. Wabnitz
  Nonlinear optics
  Rogue waves

- Heriot-Watt University, Institute of Photonics and Quantum Sciences
  D. Faccio, F. Biancalana
  Nonlinear optics

D.3 Evaluation activity

- Reviewer for several journals, including
  - Physical Review A, E, Letters
  - Optics Letters, Optics Express, JOSA B
  - Physics Letters A, Physica D, Optics Communications, Optical Fiber Technology
  - European Physics Letters, European Physical Journal
  - IEEE Journal of Quantum Electronics, Scientific Reports
- Member of one PhD thesis committee (*Examinateur*)
  - Gang XU, *Emergence of incoherent solitons and shock-like singularities in optical turbulence*, Université de Bourgogne Franche-Comté (2015)

D.4 Scientific production

- Peer-reviewed papers in international journals: 95
- Invited conferences: 14
- International conferences: 59
- Book chapters: 7
- Patents: 1
- h-index: 21, citations: 1457 (ISI)

Instabilities, shock waves and solitons in optical fiber systems

Abstract

This Manuscript resumes the principal research activities that I have conducted since my arrival at the *Laboratoire de Physique des Lasers, Atomes et Molécules* (PhLAM). The first Chapter describes the development of modulation and parametric instabilities in passive ring cavities with inhomogeneous dispersion. The second Chapter is devoted to the analysis of the nonlinear stage of modulation instability in optical fibers with periodic dispersion. The third Chapter deals with dispersive shock waves in fibers and resonators. The fourth Chapter reports on the interactions between solitons and linear waves in optical fibers with varying dispersion. The last part of the Thesis, composed of four Appendices, reports a complete list of my publications, my Curriculum Vitae, a summary of teaching and supervision activities, of responsibilities and of scientific collaborations.

Keywords: shock waves, instabilities, solitons, nonlinear optics, fibers

Instabilités, ondes de choc et solitons dans les systèmes à fibre optique

Résumé

Ce Manuscrit résume les principales activités des recherche que j'ai menées depuis mon arrivée au *Laboratoire de Physique des Lasers, Atomes et Molécules* (PhLAM). Le premier Chapitre décrit les études de l'instabilité de modulation et paramétrique dans les cavités fibrées avec une modulation longitudinale de la dispersion. Le deuxième Chapitre est dédié à l'analyse du régime non-linéaire de l'instabilité de modulation dans des fibres optiques avec dispersion périodique. Le troisième Chapitre traite des ondes de choc dispersives dans les fibres optiques et les résonateurs. Le quatrième Chapitre porte sur les interactions entre solitons et ondes linéaires dans les fibres optiques avec dispersion variable. La dernière partie de la Thèse, composée de quatre Appendices, contient une liste complète de mes publications, mon Curriculum Vitæ, un résumé de mes activités d'enseignement et encadrement, de mes responsabilités scientifiques et de mes collaborations.

Mots clés : ondes de choc, instabilités, solitons, optique non-linéaire , fibres

Laboratoire de Physique de Lasers, Atomes et Molécules
Bât. P5 - USTL – F-59655 Villeneuve d'ascq cedex

